Geophysical Investigation of Urban Subsurface in the historical center of Messina, Southern Italy

Malik Adam Alddoum Adam[1], Sebastiano D'Amico[2], Domenica De Domenico[1], Francesco Panzera[3], Debora Presti[1], Silvia Scolaro[1], Cristina Totaro[1]

[1] *Department of Mathematics, Computer Sciences, Physics, and Earth Sciences, University of Messina, University of Messina, Italy.*
[2] *Department of Geosciences, University of Malta, University of Malta, Malta.*
[3] *Department of Biological, Geological and Environmental Sciences University of Catania, Italy*

This study was conducted in Messina, southern Italy, located within a seismically active area characterized by significant near-surface heterogeneity arising from repeated damaging earthquakes, such as the destructive events of 1783 and 1908. Post-seismic reconstruction led to the accumulation of thick, laterally discontinuous anthropogenic deposits composed of rubble and debris, which, together with a vertically complex natural stratigraphy, complicate the subsurface characterization and the seismic site response assessment. An integrated geophysical investigation was conducted in the historical center of Messina, focusing on the area surrounding the Cathedral, where both geological and human-induced processes strongly influenced the subsurface. Ambient vibration data were analyzed using the Horizontal-to-Vertical Spectral Ratio (HVSR) technique, and active and passive surface-wave methods, including Multichannel Analysis of Surface Waves (MASW) and array-based approaches, were applied to derive shear-wave velocity (Vs) profiles at different depths. The results of the investigation indicate a dominant resonance at approximately 1.0 Hz, associated with alluvial deposits overlying the metamorphic basement, together with localized high-frequency peaks (>30 Hz) interpreted as shallow anthropogenic layers. Surface-wave inversions identify: (i) a very low-velocity surficial layer ($Vs \approx 150–200$ m/s, 2–3 m thick); (ii) intermediate deposits with Vs of ~300–500 m/s, and (iii) deeper velocity increases marking major stratigraphic discontinuities. Joint inversion of HVSR and dispersion data constrains the main impedance contrast, placing the bedrock interface at depths of approximately 90–100 m. The integrated results delineate key stratigraphic boundaries and the spatial variability of anthropogenic fills, especially due to post-earthquake reconstruction, demonstrating the effectiveness of a multi-method geophysical approach in complex urban environments. The derived subsurface models provide essential input for seismic microzonation, site response analysis, and hazard mitigation strategies in one of the most seismically vulnerable areas of the central Mediterranean.

Corresponding author: malik.adamalddoumadam@studenti.unime.it

Multimethod Geophysical Characterization of Subsurface Conditions in Monumental and Archaeologically Sensitive Urban Sites

Giuseppe Calamita[1], Luigi Capozzoli[1], Gregory De Martino[1], Jessica Bellanova[1], Sabatino Piscitelli[1], Angela Perrone[1], Luigi Martino[1,2], and Maria Rosaria Gallipoli[1]

[1] *Institute of Methodologies for Environmental Analysis (CNR - IMAA, Italy)*
[2] *University of Basilicata (Italy)*

Cultural heritage represents a fundamental component of the historical, social, and cultural identity of urban environments and requires effective strategies for long-term preservation. Many monumental buildings and historic urban centres are founded on complex subsurface settings, often consisting of multiple archaeological layers accumulated over centuries and superimposed on heterogeneous geological deposits. In such contexts, incomplete or fragmented knowledge of subsurface conditions may limit archaeological interpretation and compromise the reliability of structural and seismic analyses. A comprehensive understanding of the interactions between underground conditions and above-ground heritage structures is therefore essential for reconstructing urban evolution and defining informed strategies for safeguarding and valorisation.

Within this framework, the Italian PRIN 2022 project NEW AGE ("New Integrated Approach for Seismic Protection and Enhancement of Heritage Buildings on Historic Earthen Deposits") promotes a multidisciplinary and integrated approach in which the urban environment is addressed as a coupled soil–foundation–structure system. The project aims to improve the characterization of under- and above-ground cultural heritage assets through innovative investigation methods and shared data protocols, enabling interoperable modelling, visualization, and analysis of complex urban systems. This integrated knowledge base represents a significant step forward in cultural heritage protection, supporting decision-making processes for risk mitigation, management, and sustainable valorisation, in line with the objectives of the Next Generation EU framework.

In this contribution, we focus on the role of non-invasive geophysical investigations as a key component of this integrated strategy, addressing the characterization of subsurface geological conditions, archaeological layers, and foundation environments in monumental urban settings. We present the application of a combined geophysical approach integrating seismic methods, Ground Penetrating Radar (GPR), and Electrical Resistivity Tomography (ERT), illustrated through two representative case studies: the Roman Amphitheatre (Arena) of Verona and the monumental complex of Santa Sofia in Benevento, including the bell tower and adjacent public spaces.

Ground Penetrating Radar investigations were carried out using two complementary acquisition systems in order to balance depth of investigation, spatial resolution, and survey efficiency in complex urban and archaeological environments. A single-channel GPR system (GSSI TerraSIRch SIR-3000), equipped with ground-coupled monostatic antennas operating at 200 and 400 MHz, was employed for targeted, high-resolution surveys in confined areas, such as internal corridors and subsurface drainage levels (e.g., the cloaca) within the amphitheatre. The combined use of these frequencies allowed the investigation of relatively deeper shallow layers (200 MHz) together with finer structural details (400 MHz), facilitating the identification of foundation elements and near-surface anthropogenic features. Overall, approximately 730 m of GPR profiles were acquired inside the amphitheatre and along the cloaca using the single-channel system at both frequencies.

In addition, a multi-channel stepped-frequency GPR system (Geoscope Kontur), operating over a broad frequency range between 80 and 3000 MHz and integrated with an external GNSS receiver (Kolida UFO 5), was adopted for large-area surveys covering the Arena floor and adjacent urban spaces, including Piazza Bra (Verona), as well as Piazza Santa Sofia (Benevento). This system provided dense spatial sampling and enhanced spatial resolution, enabling detailed imaging of shallow subsurface heterogeneities and the detection of archaeological anomalies associated with different construction and occupation phases. The integration of GNSS positioning ensured accurate georeferencing of the radar data, supporting spatial correlation with other geophysical datasets and archaeological information.

Radar data processing was performed using the commercial software Examiner, which allows the extraction of constant-depth time slices of the subsurface. This approach facilitates the identification of coherent reflection patterns related to contrasts in the physical properties of the investigated materials, potentially associated with buried structures and underground utilities. Data acquisition was conducted along two orthogonal directions to ensure complete spatial coverage and maximize lateral resolution. Using the multi-channel GPR system, approximately 6,800 m² were surveyed in Piazza Bra and 1,500 m² inside the Arena (Verona), while an additional area of about 3,000 m² was investigated in Piazza Santa Sofia (Benevento). Overall, the combined use of single-channel and multi-channel GPR systems allowed flexible adaptation to site-specific constraints and provided high-resolution characterization of shallow subsurface features relevant to archaeological interpretation and foundation assessment.

Electrical Resistivity Tomography surveys were conducted in both Verona and Benevento to investigate subsurface geological conditions, archaeological layers, and foundation systems at different spatial scales. All ERT acquisitions were performed using instruments manufactured by IRIS Instruments: the Syscal Pro system was employed in Verona, while the Syscal Terra system was used in Benevento.

In Verona, ERT surveys were carried out inside the Arena and in Piazza Bra. In Piazza Bra, two long ERT profiles were acquired with an electrode spacing of 5 m, covering a total length of approximately 235 m. These profiles were designed to investigate the deeper subsurface, reaching depths of several tens of meters, and were primarily aimed at reconstructing the geological setting underlying the monumental area. Inside the Arena, ERT investigations focused on the Cavea, where two profiles were acquired along different arcades and complemented by a roll-along ERT survey conducted along the longitudinal tunnel beneath the Cavea. This configuration increased lateral coverage and resolution in areas of archaeological interest, supporting the interpretation of shallow subsurface features and foundation-related structures.

In Benevento, ERT investigations were conducted at Piazza Santa Sofia and around the Santa Sofia bell tower, adopting a multiscale strategy to address both geological and structural objectives. A longer ERT profile, consisting of 48 electrodes with a spacing of 2 m, was acquired to obtain a broader-scale view of the subsurface, reaching depths close to 20 m and providing information on the local geological framework. In addition, shorter and higher-resolution ERT profiles were deployed directly at the base of the bell tower, using electrode spacings of 1 m and 2 m, with the specific aim of improving the imaging of shallow layers and better constraining the geometry and extent of the foundation system.

Thanks to the flexibility of the acquisition system and array configurations, ERT data in Benevento were collected using three different setups: (i) common-cable configuration, where both transmitter (Tx) and receiver (Rx) dipoles are located on the same cable; (ii) cross-cable configuration, where Tx and Rx dipoles are positioned on two parallel cables; and (iii) x-cable configuration, in which individual electrodes of the Tx and Rx dipoles are distributed across separate cables. While the cross-cable setup enhances lateral coverage relative to the common-cable configuration, it still represents a pseudo-3D approach, as the sensitivity of each measurement remains largely confined to the plane defined by the dipoles. In contrast, the x-cable configuration provides true three-dimensional sensitivity, allowing a more robust characterization of complex subsurface structures beneath and around the monument.

The combined interpretation of seismic, GPR, and ERT data, supported by archaeological evidence and geotechnical borehole information, enables a more reliable reconstruction of subsurface stratigraphy and foundation contexts. These results provide a physically consistent framework for refining numerical soil–structure interaction models. The analysis of the dynamic behaviour of the monumental structures themselves is addressed in separate contributions by Gallipoli et al., presented within the same conference.

Aknoledgments

Geophysical surveys were also conducted using instrumentation and facilities provided by the IRPAC and ITINERIS research infrastructures, funded through regional and national programmes (PO FESR Basilicata 2014–2020 – DGR n. 402 del 28.06.2019 / CUP: G29J19001190003) and European initiatives (Next Generation EU, PNRR, M4C2 inv.3.1, CUP B53C2200215000).

Corresponding author: giuseppe.calamita@cnr.it

Small-scale passive surface-wave tomography and rapid Vs estimation in a mud volcano system

Carfagna Nicolò[1], Albarello Dario[1,2]

[1] *Department of Physical, Earth and Environmental Sciences, University of Siena, Italy*
[2]*Consiglio Nazionale delle Ricerche, Istituto di Geologia Ambientale e Geoingegneria, Rome, Italy*

Small-scale subsurface seismic imaging is traditionally approached using active techniques (i.e Barone et al.,2021; Boiero & Socco, 2010), such as MASW or refraction profiles, while passive methods remain relatively underexplored in strongly laterally heterogeneous and fluid-driven contexts. In this work, a local passive seismic imaging of the sedimentary volcanism system of the Salse di Nirano (Northern Apennines) is presented. The approach is based on time (Levshin et al., 1972) and frequency (Aki, 1957; 1965) correlation of ambient seismic noise to extract multiple phase dispersion curves using a two-station method. Ambiguity in phase curve selection is reduced through automatic comparison with the corresponding group curves. The obtained phase velocities are used to construct local-scale phase velocity maps, linearly inverted in a single step for all frequencies by introducing spatial and frequency correlation constraints to ensure solution stability. Local dispersion curves derived from the phase velocity maps are then rapidly inverted to obtain effective Vs profiles. The inversion assumes a relationship between frequency and sensitivity depth of surface waves, whereby phase velocity mainly reflects elastic properties of specific depth ranges. This approach allows estimating realistic Vs profiles representative of the local structure without global sampling of the solution space, making it suitable for the inversion of numerous curves. The results highlight marked lateral heterogeneity beneath the site and demonstrate the effectiveness of passive approach for small-scale imaging of complex systems.

References

Aki, K. (1957) Space and time spectra of stationary stochastic waves, with special reference to microtremors. Bull Earthq Res Inst 35:415–457

Aki, K., 1965. A note on the use of microtremors in determining the shallow structures of the Earth's crust. Geophysics 30, 665–666.

Barone, I., Boaga, J., Carrera, A., Flores-Orozco, A., & Cassiani, G. (2021). Tackling Lateral Variability Using Surface Waves: A Tomography-Like Approach. Surveys in Geophysics, 42(2), 317–338. https://doi.org/10.1007/s10712-021-09631-x

Boiero, D., & Socco, L. V. (2010). Retrieving lateral variations from surface wave dispersion curves. Geophysical Prospecting, 58(6), 977–996. Portico. https://doi.org/10.1111/j.1365-2478.2010.00877.x

Levshin, A.L., Pisarenko, V., Pogrebinsky, G., 1972. On a frequency–time analysis of oscillations. Ann. Geophys. 28, 211–218.

Corresponding author: nicolo.carfagna@student.unisi.it

Magnetic UAV Sensing of non-volcanic CO2 degassing area: the case study of Mefite D'Ansanto

Raffaele Castaldo[1,2], Filippo Accomando[1,2], Andrea Barone[1,2], Maurizio Buonanno[2,3], Salvatore Grimaldi[4], Francesco Mercogliano[5], Antonio Napoliello[6], Susi Pepe[1,2], Tony Alfredo Stabile[7], Pietro Tizzani[1,2]

[1] *Institute for Electromagnetic Sensing of the Environment, National Research Council of Italy (CNR IREA), Via Diocleziano, 328, 80124 Naples, Italy*
[2] *GAIA iLAB, Piazzale E. Fermi, 1, 80055 Portici, Italy*
[3] *Institute for Agricultural and Forest Systems in the Mediterranean, National Research Council of Italy (CNR ISAFoM), Piazzale E. Fermi, 1, 80055 Portici, Italy*
[4] *University of Naples Parthenope, Centro Direzionale Isola C4, 80143 Naples, Italy*
[5] *Department of Basic and Applied Sciences (DiSBA) – University of Basilicata, 85100 – Potenza*
[6] *GeoSMART Italia s.r.l s – Service Companies and Models Applied to Geology – Spin Off Unibas, Via dell'Ateneo Lucano, 10 – Sede legale: via Domenico di Giura, 54 – 85100 - Potenza*
[7] *Institute of Methodologies for Environmental Analysis, National Research Council of Italy (CNR IMAA), 85050 TITO (PZ)*

The Mefite in the Ansanto Valley (Southern Apennines, Italy) represents a unique geological phenomenon characterized by a small sulfurous puddle with continuous emissions of gases, mainly carbon dioxide (CO_2) and hydrogen sulfide (H_2S), from the subsurface. These emissions occur in a non-volcanic environment and are associated with pseudo-volcanic processes linked to the Messinian salinity crisis deposits. Mefite d'Ansanto is recognized as the largest natural source of low-temperature CO_2-rich gases from a non-volcanic setting ever measured on Earth, with an estimated flux of approximately 2000 tons per day. The gas discharge is fed by a buried reservoir composed of permeable limestones overlain by clayey sediments (Chiodini et al., 2010).

In May 2025, we conducted a UAV-based LiDAR survey followed by a magnetic survey over the Mefite area. The LiDAR acquisition provided a high-resolution both Digital Terrain Model (DTM) and Digital Surface Model (DSM) covering 1.2 km² (Fig.1), which was essential for planning the magnetic survey in terrain-following mode, ensuring a fight with constant altitude relative to the topography. The UAV platform employed was a DJI Matrice 300 RTK. Magnetic data were acquired using a Geometrics MagArrow magnetometer, featuring a sensitivity of 1 pT/√Hz and a sampling frequency of 1000 Hz. This instrument is equipped with the Micro Fabricated Atomic Magnetometer (MFAM) sensors, which exhibit only a polar dead zone, producing weak or no signal when aligned within ±35° of the Earth's magnetic field vector (Accomando et al., 2025).

The two drone-based magnetic surveys are characterized by the following features: Area 1, centered on the Mefite gas emission puddle, flown over in May 2025 and highlighted with a blue rectangle in Fig. 1, extends for 350 m × 450 m with a line spacing of 10 m; in this case the MagArrow sensor was suspended 3 m below the UAV. The Area 2, acquired in November 2025 and marked with a red rectangle in Fig. 1, covers 0.45 km^2 with a line spacing of 20 m and the sensor rigidly mounted on the UAV. Both surveys were conducted at 35 m A.G.L., with a flight speed of 4 m/s.

Magnetic data were processed to remove heading errors and high-frequency noise induced by UAV rotors. Filtering steps ensured the isolation of geophysical signals from platform-related artifacts. The local geomagnetic field has a declination of 4° and an inclination of 57° and these parameters are used for the reduction to the pole transformation. The processed magnetic map revealed an ellipsoidal anomaly centered on the Mefite pond, with an amplitude of approximately 60–70 nT. A second, more intense anomaly was detected northeast of the main CO_2 emission zone. These anomalies are interpreted as related to the presence of magnetic minerals transported by deep fluids and precipitated near the emission vents.

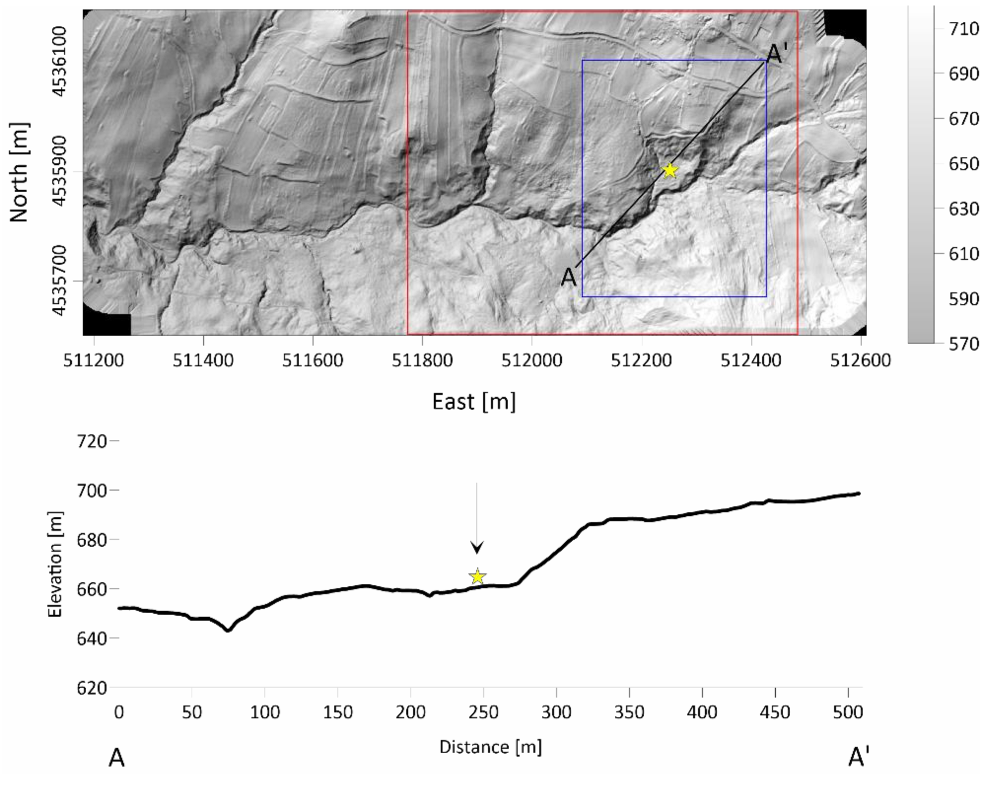

Fig. 1 – Digital Terrain Model of the study area. The blue and red rectangles show where the magnetometric survey was carried out in May (Area 1) and November 2025 (Area 2), respectively. The yellow star marks the Mefite puddle of CO_2 emission. The black line indicates the trace of the A-A' altitude profile shown below.

Acknowledgments

The activities are partially supported by the projects “Relation between 3D Thermo-Rheological Model and Seismic Hazard for Risk Mitigation in the Urban Areas of Southern Italy”, funded under the PRIN2022 PNRR initiative (code: P202299L2C) and FRACTURES PRIN-MUR 2022 (grant no. 2022BEKFN2), both supported by the European Union-Next Generation EU.

References

Chiodini, G., Granieri, D., Avino, R., Caliro, S., Costa, A., Minopoli, C., & Vilardo, G. (2010). Non-volcanic CO_2 Earth degassing: Case of Mefite d’Ansanto (southern Apennines), Italy. Geophysical Research Letters, 37, L11303. https://doi.org/10.1029/2010GL042858

Accomando, F., Barone, A., Mercogliano, F., Milano, M., Vitale, A., Castaldo, R., & Tizzani, P. (2025). Advances in Magnetic UAV Sensing: A Comparative Study of the MagNimbus and MagArrow Magnetometers. Sensors, 25(19), 6076. https://doi.org/10.3390/s25196076

Corresponding author: castaldo.r@irea.cnr.it

AI-based quality check and interpretation of microtremor H/V curves

Silvia Castellaro[1], **Laura Dal Compare**[2]

[1] Dipartimento di Fisica e Astronomia, Alma Mater Studiorum Università di Bologna, v.le C. B. Pichat 8, 40127 Bologna (Italy)

[2] MoHo slr, via delle Industrie 17/a, 30175 Venezia (Italy)

Introduction

Microtremor H/V measurements are extensively used today in many areas of earthquake engineering and exploration geophysics. They are the fastest and cheapest way to assess the resonance frequencies of the ground and to map the geometry of the main seismic reflectors down to 1-1.5 km depth (Figure 1). A single measurement takes just a few minutes with portable seismometers, but many measurements are required to image the ground in detail.

As for all geophysical techniques, being able to assess the quality, recognizing the issues and the information in a microtremor recording requires training and experience. Also, when the recordings to process are some hundreds or thousands, it requires time. 20 years ago, the SESAME (2004) guidelines attempted to provide criteria to assess the reliability of H/V curves and the clarity of H/V peaks. However, these criteria are now partly obsolete (Molnar et al. 2022). As for many other classification tasks, a neural network approach could be more effective than a threshold-based classification, as in SESAME. Thus, to help both field operators and data analysts, we trained a supervised neural network (NN) to classify different features of H/V curves and to provide hints about their interpretation. The training dataset was built starting from 3000 recordings collected over the past 15 years at different sites in the world. The NN analyses the H/V curves as a function of frequency and classifies each selected frequency interval into 7 different categories. When several H/V recordings are provided to the NN, this analyses them in a single batch and also provides a summary sheet, marking problematic recordings or recordings needing to take some actions.

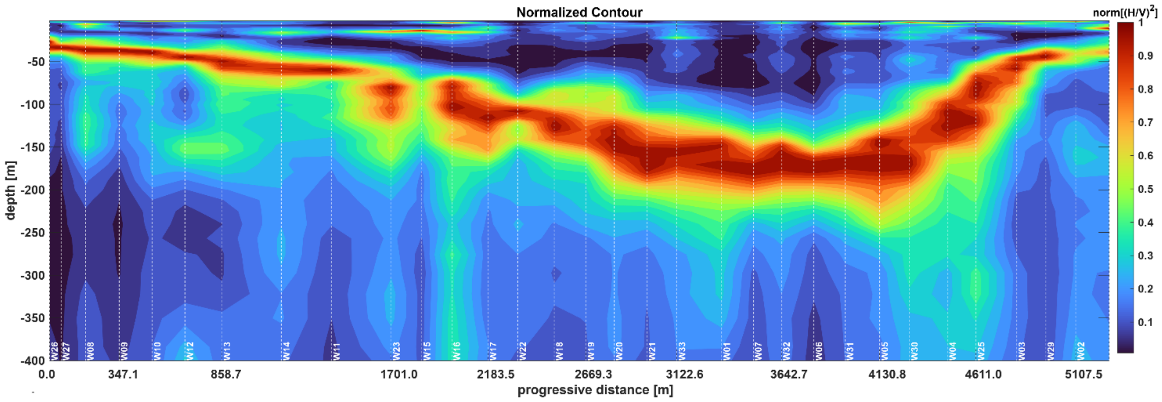

Fig. 1 – Example of bedrock imaging over a 5 km section as obtained from 29 single-station non-synchronized microtremor measurements.

Method

The goal was to create a NN capable to discriminate the following features:

- Normal H/V curves
- 1D H/V peaks
- 2D H/V peaks
- Artefacts
- Velocity inversions
- Recordings to be cleaned
- Malfunctioning sensors.

The training dataset consisted of more than 3000 examples. As input, we used 200 values extracted from the NS, EW and Z spectral components. After several attempts, we found that the best performing NN configuration was achieved by using a network with 3 hidden layers with 60 nodes each.

We implemented a software that for each new input example presented to the NN, consisting of an H/V curve and the corresponding NS, EW, Z spectra, analyses consecutive or on-demand overlapping frequency windows and provides a classification output as in Figure 2. When several curves are analysed, a summary assessment on the H/V measurement quality is also provided, marking good, fairly acceptable, non-acceptable measurements.

Results and Conclusions

The NN was found to perform well in 80-82% of single windows presented as input. However, a single H/V normally includes 20 to 40 of these windows. An expert system applied after the NN classification is capable of summarising the categorization of each window and providing a more general result, whose accuracy is about 90%. The most challenging classification task for the NN was distinguishing 2D resonances, associated with soils and structures, from artifacts, as these two categories share many characteristics

This neural network serves three main purposes. First, it enables automatic quality control by distinguishing high-quality records from potentially problematic ones, which can often be recovered by removing transients, and from compromised records. This is particularly useful when processing large datasets or when field acquisitions are performed by non-geophysicists who require a data quality check.

Second, it allows the rapid extraction of microtremor H/V curves showing a common pattern from huge databases.

Third, the NN offers an alternative to the SESAME criteria, which provide guidelines for selecting analysis parameters and evaluating the reliability of H/V peaks. However, some of these guidelines are now outdated and require revision. Given the complexity and variability of H/V curves, a classifier based on an NN can be more effective than fixed-threshold criteria like those in SESAME.

Last, NNs can detect patterns that may not be immediately visible to the human eye. While these patterns are not necessarily correct, analyzing the NN errors can still provide valuable insights into the data.

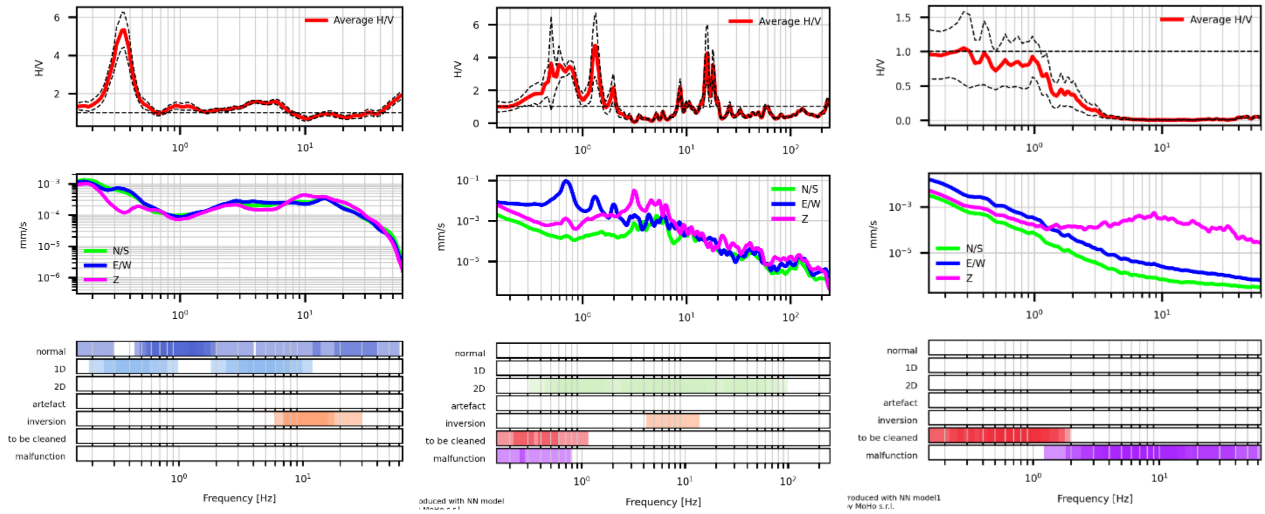

Fig. 2 - Examples of NN classifications. Top panels: average H/V ratio. Central panels: 3D-spectra. Bottom panels: NN classification. Left column: correctly detected 1D soil resonance at 0.3 Hz and an overall good quality. Central column: correctly detected 2D resonances and artefacts (this was collected at the base of a large bridge and the peaks are the resonances of the bridge transmitted to the ground). Right column: measurement with a malfunctioning EW component.

References

Castellaro, S., and F. Mulargia, 2009, The effect of velocity inversions on H/V: Pure and Applied Geophysics*,* **166**, 567-592.

Castellaro, S., 2016. The complementarity of H/V and dispersion curves: *Geophysics*, 81, T323-T338.

Castellaro, S., and G. Musinu, 2023. Resonance vs. shape of sedimentary basins: Bulletin of the Seismological Society of America, 113, 745-761.

Castellaro, S., and L. Dal Compare, 2025. A Neural Network Approach for Quality Control and Interpretation of Single Station Microtremor Measurements, Geophysics, minor revisions

Di Donato M., and S. Castellaro, 2024, Performance of different ANNs in microtremor H/V peak classification: Seismological Research Letters, **95**, no. 6, 3722-3736.

Ibs-von Seht, M., and J. Wohlenberg, 1999. Microtremor measurements used to map thickness of soft sediments: Bulletin of the Seismological Society of America, **89**, 250–259.

Molnar, S., A. Shirohey, J. Assaf, P.-Y. Bard, S. Castellaro, C. Cornou, B. Cox, B. Guiller, B. Hassani, H. Kawase, S. Matsushima, and F.J. Sánchez-Sesma, 2022, A review of the microtremor horizontal-to-vertical spectral ratio (MHVSR) method: Journal of Seismology, **26**, 653-685.

SESAME Project, 2004, Guidelines for the implementation of the H/V spectral ratio technique on ambient vibrations: measurements, processing and interpretation: SESAME European Research Project WP12, deliverable.

Effect of embankment structure on seismic wave propagation

Dario Chieppa[1]**, Andrea Vergnano**[2]**, Cesare Comina**[2]**, Laura Valentina Socco**[1,3]

[1] *Department of Environment, Land and Infrastructure Engineering, Politecnico di Torino, Italy*
[2] *Department of Earth Sciences, University of Turin, Italy*
[3] CEG*, Delft University of Technology, Netherlands*

Introduction

River embankments are morphological structures built to protect urbanized areas from flooding events. In recent years, due to the extreme rainfalls, portions of embankments have collapsed pointing out the need for an accurate characterization of these structures. Geophysical methods provide an efficient and non-invasive way to investigate their physical properties and their lateral variability with the possibility to recognize weak zones that need to be reinforced.

The analysis of seismic surface waves (SW) have been widely adopted for embankment characterization (e.g. Karl et al., 2011; Joubert et al., 2018; Le Feuvre et al., 2015; Planès et al., 2017; Planès et al. 2016; Arato et al., 2022; Comina et al. 2020, Busato et al., 2016). However, only in few cases seismic numerical simulations were performed to understand the dynamic response of an embankment to SW propagation and its influence on the tests results (e.g. Pageot et al., 2020, Karl et al., 2011). This work aims at exploring, through numerical simulations, the effects of the geometry of an embankment on the SW propagation.

Modelling

To simulate the seismic wave-field propagation, we used the 3D finite-difference Seismic Wave simulation (SOFI3D) algorithm, developed by Bohlen et al. (2002). To build the embankment model, a volume with a squared base of about 100x100 meters and height of 33m is generated. The embankment is located on top of this volume, at its centre with respect to the x-axis and extend along the y-axis (Fig. 1a). Four different heights are tested for the embankment (3, 5, 7, and 9 meters) and four different slopes of the flanks (length to height ratios of 0.5, 1, 2 and 3). The top embankment width is set constant to 6 m in all simulations. On top of the embankment 50 three-components geophones 1m spaced are deployed (blue triangles). The source employed for the simulation is a Ricker wavelet with a central frequency of 60 Hz. The shot location is at 10 meters from the first geophone (yellow stars). The model is made of cubic cells of 0.1x0.1x0.1 m each.

All the geometrical combinations of the embankment are tested for a stratified model consisting in one layer (embankment) over the halfspace (Fig. 1c) where the velocity of the embankment is lower than the one of underlying ground. An initial geometric configuration (height 3m and slope ratio of 2) is tested for a homogeneous media also (Fig. 1a) to compare the results. P- and S-wave velocities, thicknesses and densities values are reported below each sketch in Fig. 1a and 1c. Around and above the embankment an air layer of 2 meters is modelled using standard parameters: V_p = 0 m/s (default value of air requested by SOFI3D software), V_s = 0.00001 m/s and ρ = 1.25 kg/m^3.

Results and discussion

Fig. 1b shows the velocity spectrum obtained for the homogenous medium (Fig. 1a); the resulting dispersion curve is flat over the entire frequency band without dispersive effect. In this condition, also the geometry of the embankment has no effect on the results. Fig. 1d shows the velocity spectra for a stratified model (Fig. 1c) with the same geometric configuration of Fig. 1a; here a dispersive behaviour is clear and several propagation modes are excited and picked on the velocity spectrum (Fig. 1d). The picked dispersion curve branches (dots in Fig.1d) are compared with the theoretical fundamental and higher modes (solid lines in Fig.1d) of a 1D model corresponding to the velocity profile on top of the embankment.

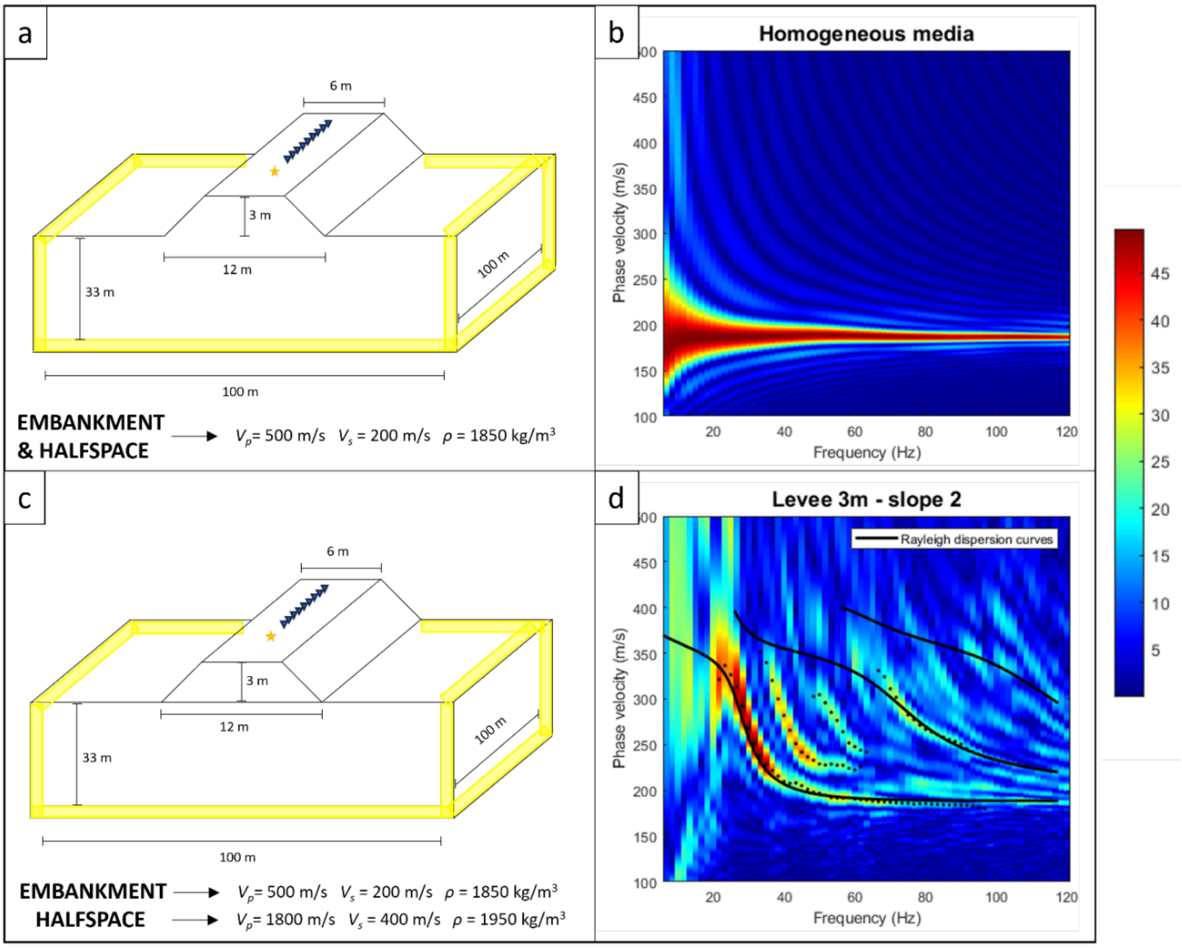

Fig. 1 - Left c: embankment models generated using SOFI3D algorithm. The geometry of the embankment is drawn maintaining the ratio between height and base, while the geometry of the half-space is not in scale. Yellow bands identify the absorption cells for each model. The size of these bands changes according to the frequency of the source. For both simulations, the source (yellow star) is a 60 Hz Ricker wavelet located 10 meters from the first geophone. Dark triangles in the left column represent the 50 geophones evenly distributed with 1m spacing. Right column: Velocity spectra for the models shown in the left column. Black dotted lines are the picked curves; continuous black lines correspond to the synthetic Rayleigh-wave dispersion curves for the 1D model. Top row: results for a homogeneous media. Bottom row: results for a stratified media consisting in an embankment overlying the half-space.

The first picked curve is in good agreement with the synthetic fundamental mode over the entire frequency range. Agreement can be found also between the first theoretical higher mode and the fourth picked curve over the 70 to 100 Hz frequency band. The second and third picked curves are instead located between the two theoretical modal curves. These dispersive events, which might be interpreted as seismic reflections from the flanks of the embankment, cannot be easily explained taking into account the features of the embankment structure (height, width, etc.).

Results from all simulations are reported in Figure 2. Each subplot contains the results for a different embankment height (3m – panel a; 5m – panel b; 7m – panel c; 9m – panel d); within each figure, all results linked to different slope ratios are also reported with different colours. Orange curves are the synthetic Rayleigh-wave dispersion curves for each 1D model.

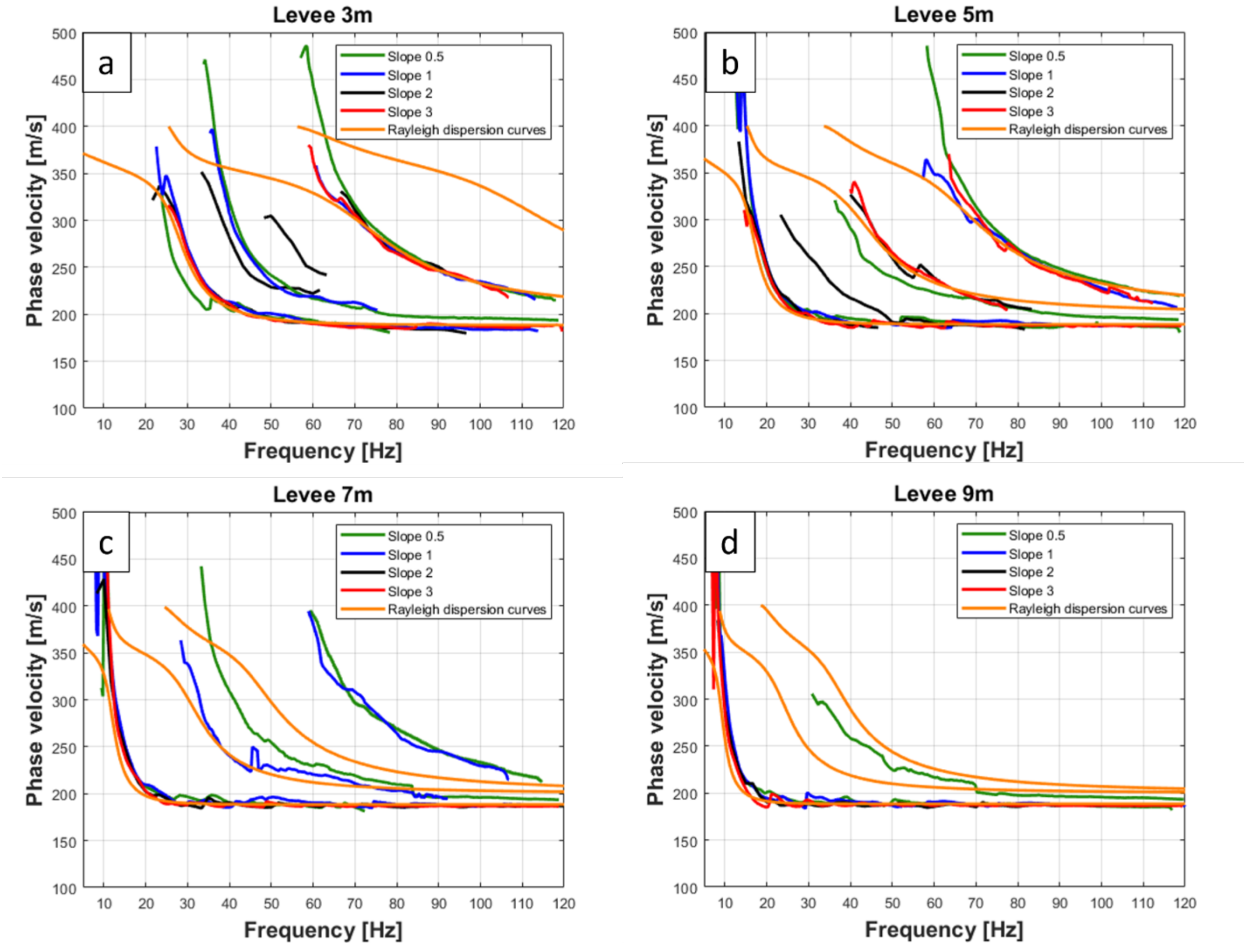

Fig. 2 - Comparison of the picked dispersion curves for each model (height of 3, 5, 7 and 9 meters) and for all tested slope ratios (0.5, 1, 2, 3). Orange continuous curves are the synthetic dispersion curves for Rayleigh wave computed assuming a 1D velocity profile crossing the embankment and the halfspace.

For all four tested embankments, the fundamental mode curve of synthetic Rayleigh waves fits the picked curve at low frequencies and low seismic velocities. The overlap is continuous from low frequencies (from 10 Hz to 30 Hz depending on the model) to 120 Hz. The fit of higher modes is conversely more difficult to interpret. Some of the picked dispersive events fit theoretical modal curves, see for instance the first theoretical higher mode (panel a - b) and the second higher mode (panel b). Nevertheless, several other curves are picked that do not always fit the theoretical modal curves. Considering the different aspect ratio of the embankment, the dispersion curves picked for an aspect ratio equal to 3 (red curves) corresponds to theoretical modal curves, while for steeper embankments, the picked curves are affected by the embankment shape and only the fundamental mode is reliable and can be inverted with a classical 1D reference model, neglecting the embankment shape.

Conclusions

The analysis performed in this work pointed out 1) the importance to understand how the seismic wave-field propagates in a complex structure as an embankment and 2) the need to discern which are the dispersive curves linked to the propagation of seismic waves from other phenomena that generate within the embankment and are not directly linked to its shape. According to our results, we can establish that no matter the height and shape of the embankment, the fundamental mode of Rayleigh-wave dispersion curve is the most energetic and fits the theoretical fundamental mode for the corresponding 1D model. This means that the fundamental mode is the only curve which can be inverted without any doubt. The other dispersive events should be assessed with numerical modelling to ensure they correspond to Rayleigh wave higher modes.
Further analyses will be carried out to explain the origin of the dispersive events within embankment structures and the effect of sources located outside the embankment, at different distances.

Acknowledgements

This study was carried out within the GEOCHARME project – funded by the European Union – Next Generation EU within the PRIN 2022 program (D.D. 104 - 02/02/2022 Ministero dell’Università e della Ricerca). This manuscript reflects only the authors’ views and opinions and the Ministry cannot be considered responsible for them.

Finanziato dall'Unione europea NextGenerationEU | Ministero dell’Università e della Ricerca | Italiadomani PIANO NAZIONALE DI RIPRESA E RESILIENZA

References

Arato, A., Vagnon, F. & Comina, C. (2022). First application of a new seismo-electric streamer for combined resistivity and seismic measurements along linearly extended earth structures. *Near Surf. Geophys. 20*, 117–134.

Bohlen, T. (2002). Parallel 3-D viscoelastic finite difference seismic modelling. Computers & Geosciences, 28(8), 887-899.

Busato, L., Boaga, J., Peruzzo, L., Himi, M., Cola, S., Bersan, S. & Cassiani, G. (2016) Combined geophysical surveys for the characterization of a reconstructed river embankment Eng. Geol., 211 , pp. 74-84, 10.1016/j.enggeo.2016.06.023

Comina, C., Vagnon, F., Arato, A. & Antonietti, A. (2020) Effective Vs and Vp characterization from Surface Waves streamer data along river embankments J. Appl. Geophys., 183 , 10.1016/j.jappgeo.2020.104221

Joubert, A., Le Feuvre, M. & Côte, P. (2018) Passive monitoring of a sea dike during a tidal cycle using sea waves as a seismic noise source, *Geophysical Journal International*, Volume 214, Issue 2, Pages 1364–1378, https://doi.org/10.1093/gji/ggy180

Le Feuvre, M., Joubert, A., Leparoux, D. & Côte, P. Passive multi-channel analysis of surface waves with cross-correlations and beamforming. *Application to a sea dike. Journal of Applied Geophysics* **114**, 36–51, https://doi.org/10.1016/j.jappgeo.2014.12.014 (2015).

Karl, L., Fechner, T., Schevenels, M., François, S. & Degrande G. (2011) Geotechnical characterization of a river dyke by surface waves Near Surf. Geophys., 9 (6), pp. 515-527

Pageot, D., Le Feuvre, M., Leparoux, D., Cote, P. & Capdeville Y. (2020) Assessment of physical properties of a sea dike using multichannel analysis of surface waves and 3D forward modeling J Appl Geophys, 172 (2020), Article 103841, 10.1016/j.jappgeo.2019.103841

Park, C.B., Miller, R.D., & Xia, J., (1999) Multichannel analysis of surface waves (MASW): Geophysics, 64, 800-808

Planès, T., Mooney, M.A., Rittgers, J.B.R., Parekh, M.L., Behm, M. & Snieder R. (2016) Time-lapse monitoring of internal erosion in earthen dams and levees using ambient seismic noise Géotechnique, 66, pp. 301-312, 10.1680/jgeot.14.P.268

Planès, T., Rittgers, J.B., Mooney, M.A., Kanning, W. & Draganov, D. (2017) Monitoring the tidal response of a sea levee with ambient seismic noise Journal of Applied Geophysics, 138 , pp. 255-263, 10.1016/j.jappgeo.2017.01.025

Corresponding author: dario.chieppa@polito.it

Quality assessment criteria for HVSR measurements: proposal and application to the Abruzzo region

Sarah Ciaglia[1], Alessandro Pagliaroli[1,3], Dario Albarello[2], Massimiliano Moscatelli[3]

[1] Department of Engineering and Geology, University of Chieti-Pescara, Pescara, Italy
[2]Department of Physical Science, Earth and Environment, University of Siena, Siena, Italy
[3]Environmental Geology and Geoengineering Institute, CNR IGAG, Montelibretti, Italy

The extensive application of the passive HVSR technique across a wide range of contexts has made the adoption of reliable quality assessment criteria essential for constraining measurement value and ensuring the robustness of the results.

This technique is a non-invasive passive geophysical investigation that does not require any active energy source and is widely applied, particularly in the framework of Seismic Microzonation and local seismic response analysis, due to its low cost and ease of acquisition. It enables the identification of zones susceptible to ground motion amplification and the fundamental resonance frequencies of soil deposits, which are of significant interest in engineering applications for the assessment of local seismic amplification effects. In particular, the HVSR technique is frequently employed for the calibration of one- and two-dimensional subsoil models, supporting the constraint of geological structure depths and geotechnical –properties. The application of the method, together with the wide range of usage contexts, requires careful control of acquisition conditions and data quality. The instrumentation typically operates within a frequency range between 0.2 and 20 Hz; for this reason, it is essential to ensure proper coupling of the sensors with the ground under free-field conditions, away from external disturbance sources and in environments free from wind, traffic, or other anthropogenic noise.

Starting from the theory based on the work of Albarello and Castellaro (2011), which presents a classification of H/V measurements, a **quality assessment model** was here developed to analyse in detail three key issues of H/V technique: documentations, measurements and processing quality, resonant peak validity.

For each category, three quality classes are proposed: A, B or C, which are subsequently combined to derive an overall quality class for the HVSR measurement.

1) Completeness of documentation: the documentation must contain all information relating to data acquisition and results of the measurement (Tab. 1).

1.1 **Processing:** information regarding acquisition and processing methods.

1.2 **Location:** information regarding the location of the acquisition, latitude, longitude, photographic documentation.

1.3 **H/V curve:** presence of the H/V curve plot within the report**.**

1.4 **Spectral components:** presence of the spectral components plot within the report.

1.5 **Directionality:** presence of a plot showing the directionality of the measured horizontal component of the signal (anisotropy).

1.6 **Stationarity:** presence of a plot showing the stationarity of the measured signal over time.

Table 1 - Evaluation grid for the first issue: documentation.

Documentation						
1° Processing	**2° Location**	**3° H/V Curve**	**4° Spectral Component**	**5° Directionality**	**6° Stationarity**	**CLASS**
X = element present Empty cell = element absent						

Class A: score 6/6 or when elements 1°- 3°- 4° - 5° are present.

Class B: score from 3/6 to 5/6 (including 3° - 4°)

Class C: score from 1/6 to 2/6 (usually including 3° - 4°) or 0

2) **Measurement quality:** the duration of the acquisition and the trace used for analysis must be no less than 15 minutes and free from interference in the frequency range of interest (Tab.2).

2.1 **Record duration:** the total length of the recording, usually between 15 and 30 minutes.

2.2 **Windows used:** indicates the number of processing windows, expressed as a percentage.

2.3 **External disturbances.**

Table 2 - Evaluation grid for the second issue: measurement.

Measurement			
Record duration	**Windows (%)**	**Disturbance**	**CLASS**

Class A: acquisition duration, combined with window utilisation percentage, ≥ 20 min; absence of disturbance at the frequency of interest.

Class B: acquisition duration, combined with window utilisation percentage, ≥ 15 min; absence of disturbance at the frequency of interest.

Class C: acquisition duration, combined with window utilisation percentage, <15 min; absence of disturbance at the frequency of interest.

The presence of disturbances at the frequency of interest results, in all cases, in a class C rating.

3) Quality of the H/V peak (Tab. 3)

3.1 Consistency with Sesame criteria: the results of the individual tests must be reported in relation to the "Sesame Criteria" (2004). In particular, the "criteria for a clear H/V peak" are compared, where the resulting peak is evaluated based on six criteria:

1) $\exists\ f^{-}$ in $[f_0/4, f_0]$ | $A_{H/V}(f^{-}) < A_0 / 2$.
2) $\exists\ f^{+}$ in $[f_0, 4f_0]$ | $A_{H/V}(f^{+}) < A_0 / 2$
3) $A_0 > 2$
4) $f_{peak}[A_{H/V}(f) \pm \sigma_A(f)] = f_0 \pm 5\%$
5) $\sigma_f < \varepsilon(f_0)$
6) $\sigma_A(f_0) < \theta(f_0)$

3.2 Presence of directionality in the signal.

Table 3 – Evaluation grid for the third issue: Peak

Peak		
SESAME Criteria	**Directionality**	**CLASS**

Class A: 5/6 Sesame criteria satisfied; no directionality.

Class B: 1-5/6 Sesame criteria satisfied; directionality.

Class C: 1/6 Sesame criteria satisfied (even in the absence of directionality)

After assigning a final class to each issue, the overall measurement quality is conclusively determined through an integrated comparison of all evaluated categories.

CLASS A: a measurement that has excellent ratings in all categories (AAA) or where only one category falls into class B (e.g., AAB, ABA, BAA). This category includes all measurements that provide all the necessary documentation, with an acquisition and processing time of between 15 and 20 minutes, and a resulting peak that is in line with Sesame criteria.

CLASS B: a measurement that scores "good" in all categories (BBB), which may also include a class A (e.g. ABB, BAB, BBA). This class includes all measurements that provide the necessary information (the report may omit some information, but overall, it is clear), whose acquisition and processing time is between 15 and 20 minutes, and whose resulting peak is in line with Sesame criteria, although they present some minor uncertainties (such as, for example, significant directionality).

CLASS C: this class includes all measurements that are negatively evaluated in at least one category; cases where all categories fall into class C (CCC) exist but are uncommon. Examples of class C measurements are:

C**: a class C for the documentation category indicates that the available documentation is incomplete and lacks essential information, which could compromise the entire measurement, since without information such as the H/V curve, the data cannot be used.

C: this score reflects acquisition conditions that negatively affect the reliability of the identified resonance peak. Consequently, a critical comparison with neighbouring measurements, together with a detailed analysis of the local stratigraphic framework, is required.

**C: this case is usually linked to a strong directionality of the peak, whose characteristics did not even meet the Sesame criteria. These data are linked to a strong anthropogenic disturbance, which requires the exclusion of the result.

To validate the proposed model and assess its applicability, all HVSR measurements acquired in the Abruzzo region within the framework of Level 1 Seismic Microzonation were analysed (fig. 1). The evaluations were performed by verifying the resonance frequency f_0, defined as the first identified resonance peak, corresponding to the lowest-frequency peak. A total of 4891 measurements were examined, of which approximately 42% were classified as low quality (class C). In these cases, class C is usually influenced by the second category ("Measurement"), which is often rated negatively because of the recording duration, further reduced during processing, and by frequently incomplete documentation (fig. 2).

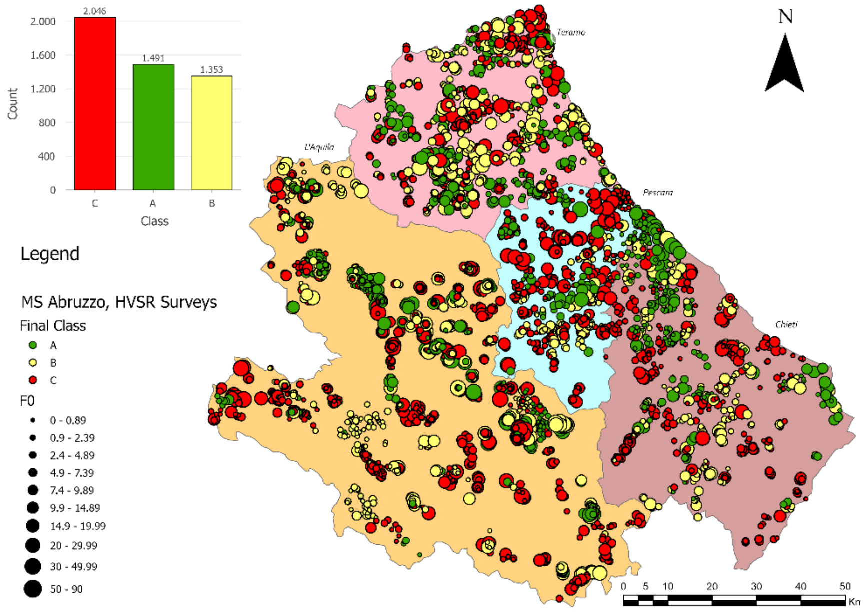

Figure 1 Quality assessment of HVSR surveys in the Abruzzo Region according to the proposed methodology

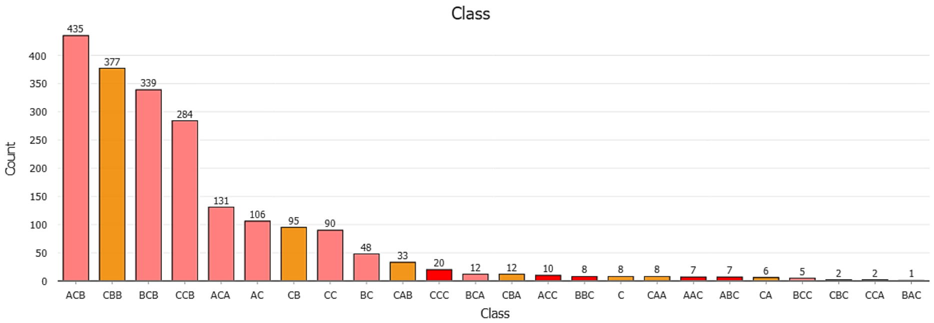

Figure 2 Categorization of class C by quality category

Additionally, a total of 261 new experimental measurements were carried out to allow comparison with data previously classified as low quality (class C) and to improve their reliability according to the defined criteria. The 6% of the new measurements were classified as class C essentially because the recording duration was reduced during the processing stage due to the presence of external disturbances, particularly wind and anthropogenic noise (fig. 3).

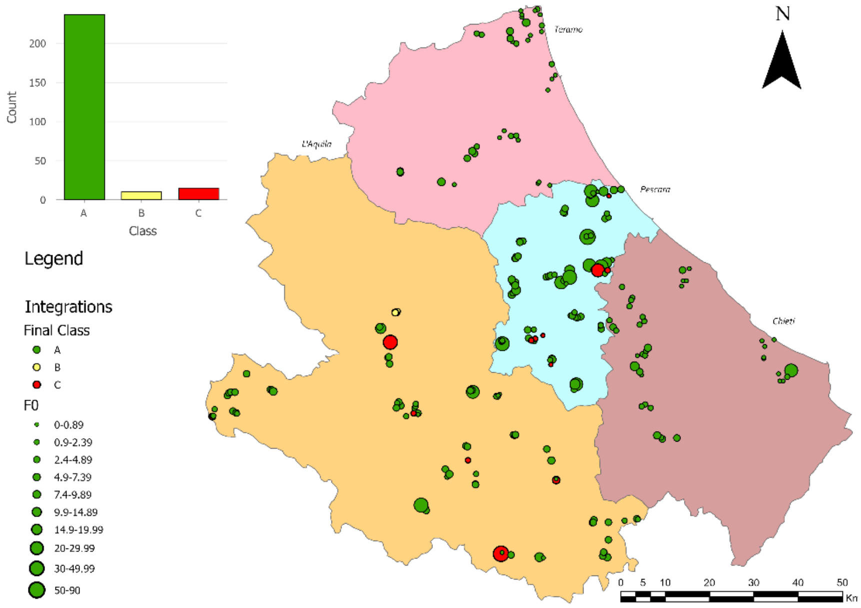

Figure 3 Spatial distribution of newly acquired experimental measurements

As evidenced by the comparison between the measurements presented in Figures 1 and 3, the implementation of an approach based on systematic data compilation and quality evaluation has resulted in a significant improvement of the available dataset. Specifically, the newly acquired data exhibit enhanced quality in both the measurement procedures and the associated documentation and can therefore be regarded as more reliable.

The proposed model is conceived as an effective practical tool for the standardization of ambient noise HVSR acquisition procedures, as well as for the evaluation and comparison of both existing and newly acquired datasets. This approach enables dataset homogenization and supports the extension of their use across a broad range of application contexts, ensuring greater reliability of the results with respect to the reference stratigraphic and geological conditions.

References

Albarello, D., & Castellaro, S. (2011). Tecniche sismiche passive: indagini a stazione singola. Ingegneria sismica, 2, 32-61.

SESAME (2004). Guidelines for the implementation of the H/V spectral ratio technique on ambient vibrations measurements, processing and interpretations. In: SESAME European research project EVG1-CT-2000-00026, deliverable D23.12.

Corresponding author: sarah.ciaglia@unich.it

Comprehensive geophysical investigation of a prehistoric site: Favella della Corte (Cosenza, Italy)

Alberto Cogliati[1], Alessandro Ghirotto[2,*], Andrea Zunino[2], Luca Peruzzo[1], Jacopo Boaga[1], Mauro Pavan[3], Egidio Armadillo[3]

[1] *Dipartimento di Geoscienze, University of Padova, Padova, Italy*
[2] *Institute of Geophysics, ETH Zurich, Zurich, Switzerland*
[3] *Applied Geophysics Laboratory, DISTAV, University of Genova, Genova, Italy*
[*] *Formerly at Applied Geophysics Laboratory, DISTAV, University of Genova, Genova, Italy*

The Neolithic settlement of Favella della Corte (Cosenza, Italy) offers a unique opportunity to study early communities in Southern Italy. This work presents the results of a non-invasive geophysical investigation of the site, providing insights into its stratigraphy and paleo-environmental context. Specifically, an integrated survey has been conducted, including magnetic field measurements, magnetic susceptibility sampling and electrical resistivity profiling, with the aim of characterising subsurface features and supporting the reconstruction of past environmental conditions.

The magnetic survey comprises 3,000 readings collected with a Proton Precession Magnetometer GEM GSM-19T over an area of 11,600 m^2. Magnetic susceptibility data were recorded by a Geofyzika KT-5 handheld kappameter on the stratigraphic units outcropping from exploratory trenches along vertical sections spaced at 20–50 cm. Electrical resistivity measurements were carried out adopting Wenner-Alpha and Beta arrays along nine profiles spaced 20 m apart and extending up to 90 m.

We have modelled the magnetic data using an “ad hoc” three-dimensional inversion strategy. The modelling domain has been discretized into a single horizontal layer of prismatic bodies and, because of the non-linearity of the inverse problem, the L-BFGS algorithm has been employed to solve the optimization problem. The model parameters used in this study are the position of the bottom of each prism and a single value of magnetic susceptibility contrast associated with all the prisms. These parameters were updated at every iteration until the L-BFGS algorithm converged. The electrical resistivity data have been modelled along two-dimensional sections using Res2dinv based on the smoothness-constrained least-squares method.

Combined modelling of magnetic and electrical resistivity datasets have revealed a NE–SW trending linear feature 70 m long crossing the whole survey area, 20 m wide, and reaching depths of about 4 m. The stratigraphic evidence resulting from exploratory trenches allowed us to interpret this anomaly in terms of geophysical parameters as a paleo-channel carved into the sandy substrate and filled with silty-clayey material. Considering the pronounced straightness of this feature, we interpreted it as an anthropogenic paleo-channel with a drainage function.

The integrated application of magnetic and resistivity techniques has proved to be highly effective for assessing the archaeological and paleo-environmental context of the Favella della Corte area, revealing subsurface stratigraphy and past environmental conditions. These findings have highlighted the value of integrated geophysical approaches for reconstructing ancient landscapes and informing future research.

Corresponding author: alberto.cogliati@phd.unipd.it

Distributed Acoustic Sensing (DAS) for river embankments monitoring: an open laboratory at the Chivasso test site.

Cesare Comina[1], Andrea Vergnano[1], Nicola Piana Agostinetti[2,3], Dario Chieppa[4], Alberto Villa[2], Marta Arcangeli[2], Lorenzo Suranna[2], Laura Valentina Socco[4,5]

[1]*Department of Earth Sciences, University of Turin, Italy.*
[2]*Department of Earth and Environmental Sciences, University of Milan Bicocca, Italy.*
[3]*Istituto Nazionale di Geofisica e Vulcanologia, Osservatorio Nazionale Terremoti, Rome, Italy.*
[4]*Department of Environment, Land and Infrastructure Engineering, Polytechnic of Turin, Italy.*
[5]*Department of Civil Engineering and Geosciences, TU Delft, Netherlands.*

Introduction

The management of river basins has often involved the building of embankments to protect surroundings from floods. As with any other structure, embankments need proper monitoring of their geotechnical properties to assess their state. This need has become more critical in recent decades due to the more frequent extreme rain events induced by climate change. However, embankment monitoring faces numerous challenges, often for the lack of comprehensive instrumentation installed along their relevant lengths. Distributed Acoustic Sensing (DAS) permanently installed over embankments could provide a feasible solution to this aim. Some example applications of DAS to the monitoring of river embankments are indeed available in recent literature (e.g. Cheng et al., 2026; Roshdy et al., 2025). However, DAS data analysis and interpretation could be critical as a function of coupling, interrogator design, adopted gauge length and noise levels in the fiber. Therefore, preliminary tests comparing DAS and standard seismic instrumentation are necessary to allow for a precise understanding of the potentially usable data.

Within this framework, preliminary tests combining DAS instrumentation and standard seismic instrumentation were performed over the Chivasso (near Torino, northwest Italy) embankment test site. Here, a DAS cable was buried within the newly constructed embankment structure and several tests were performed comparing the obtainable DAS seismic response with standard seismic instrumentation. Specifically, variations of the frequency content of the data as a function of adopted gauge length and in comparison with standard seismic surveys were investigated. Also, stacking strategies for the DAS signal were attempted to take advantage of multiple fiber cables.

The final aim of this work is the implementation of an open field laboratory for the study of DAS response over embankment structures in order to improve the applicability of this technology at a wide scale available for different researchers to test their acquisition and interpretation approaches. Also, the preliminary calibration data of this work and the ones that are planned in the near future will be made available for comparison.

Test site and preliminary acquisitions

The Chivasso embankment test site is a newly constructed embankment located along the hydrographic left of the Orco river, near the city of Chivasso, near Torino, northwest Italy (Figure 1). The embankment is specifically placed in a critical location due to the presence in the nearby of several infrastructures that could be severely affected by floods (i.e. the A4 Torino-Milano highway, the high speed Torino-Milano railway and the old RFI Torino-Milano railway). Moreover, the embankment is near the confluence of the Orco river with the Po River in a critical hydrogeological zone. The embankment is of very recent construction (works were ultimate in July 2025) and was specifically built to protect the surrounding infrastructures. It has an average height of about 2 – 3 m and is constituted of compacted silty sands. The natural subsoil below the embankment is conversely mainly made of coarse gravels. The attended water table depth is of about 4 m b.g.l. Several geotechnical field and laboratory tests are available on both embankment material and natural subsoil making it an ideal test site for comparing seismic data analyses with standard geotechnical parameters which are often the aim of the characterization.

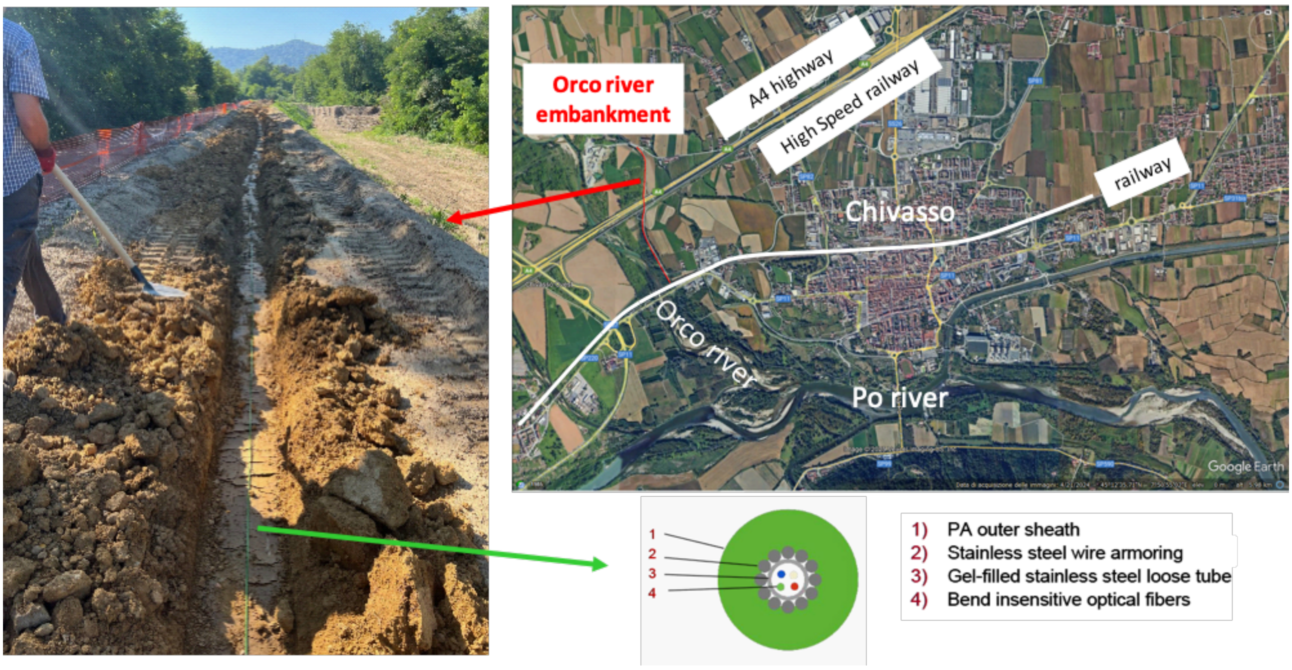

Figure 1 – Location of the test site and of the DAS cable installed over the embankment.

A Solifos BRUsens – DAS AC3 Steel-Armored Acoustic Sensing Cable was buried at about 0.5 m depth in a trench executed on top of the embankment (Figure 1). This cable is composed of 4 different optical fibers that were looped at the extremities in order to be acquired with a single interrogator unit (IU) placed at one of its ends. The length of the buried cable is of about 270 m and the cable is located in the central portion of the embankment in between the main transversal highway and railways.

The DAS IU adopted in the preliminary tests of this work is a Febus A1R, with a single interrogated fiber cable. To enable the best approach for data analysis, only raw optical phase data have been acquired, i.e. without direct strain-rate conversion, which was performed post acquisition in order to evaluate different conversion parameters. The DAS IU has been set with the following aacquisition parameters: spatial sampling was set to 40 cm, i.e. the minimum available DAS channel spacing; pulse width was equal to 1 meter, enabling to reach down to a 1 meter Gauge Length (GL) in post-processing; pulse rate frequency of the laser (i.e. the number of laser pulses per second) was set to 20.000, which can be processed to obtain 4000 sps in strain-rate time series. Looping all optic fibers in the cables gave us about 1200 of interrogated fiber length. As reference, we recorded with the above parameters about 24 Tb per minute of raw data.

In the preliminary surveys of this paper 10 three-component (4.5 Hz) connected to NuSeis^{TM} nodes have been adopted with an approximate spacing of 30 m. The seismic source used for active shots was a Geodevice Accelerated Weight Drop (AWD) with a 40 Kg hammer driven with powerful springs, attached to an electric winch and mounted on a compact lightweight frame equipped with wheels and handles for ease of transportation around survey area. The preliminary seismic shots executed with this source will be adopted for direct comparison of the seismic responses of the buried DAS in comparison with standard geophone as commented hereafter.

Results and discussion

The main intended use of DAS data is related to the analyses of surface waves both from ambient noise and from active seismic shots. Frequency content of the data as a function of GL, noise levels in the DAS, related to its coupling, and comparison of DAS data with standard seismic surveys play therefore a fundamental role. In the preliminary tests all these aspects were investigated.

First, comparison of DAS data quality as a function of GL was addressed. Raw DAS data of the test seismic shots were processed at a 1000, 2000 and 4000 S/s sampling rates and later the effect of different GL (i.e. 1, 2, 4, 8) was investigated either through the analysis of the quality of the acquired shot gathers and of their f-k transforms (Figure 2a).

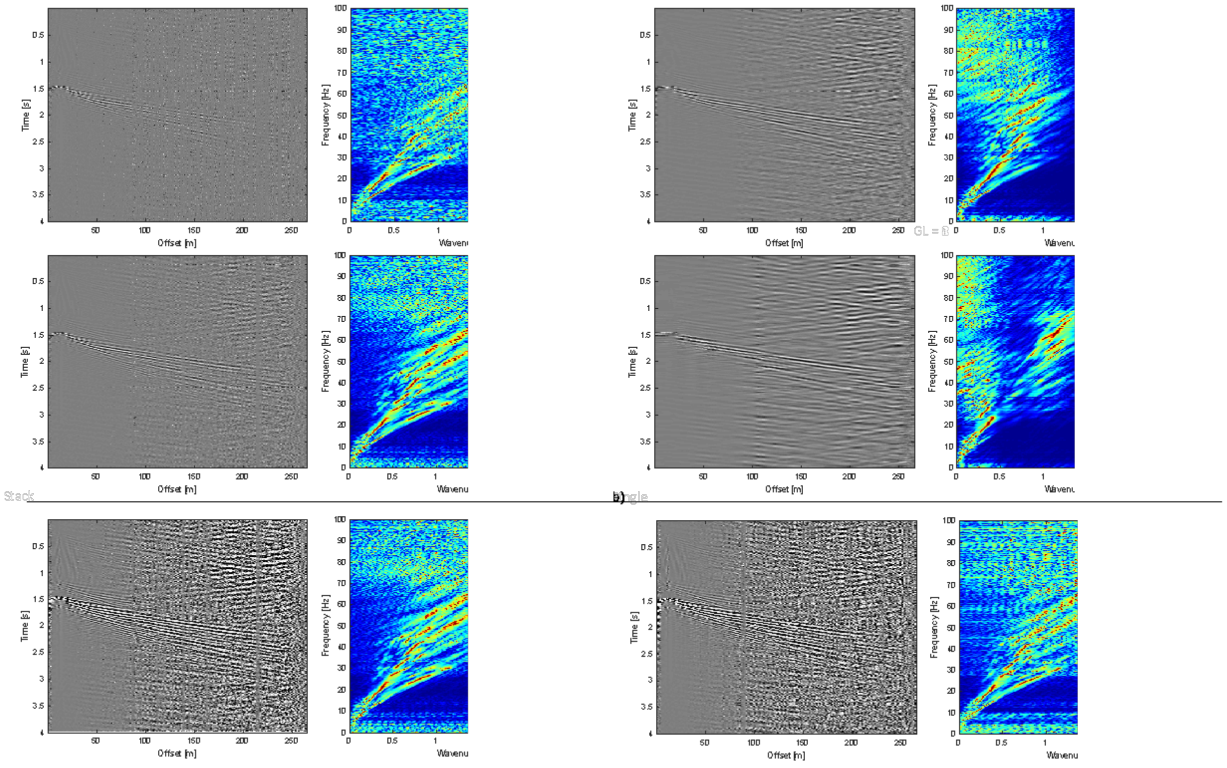

Figure 2 – Preliminary tests on the quality of DAS acquired data: a) as a function of the adopted Gauge Length; b) Stacking of multiple fibers along the cable in comparison with the acquisition of a single fiberv only.

In general, the improvement in the S/N ratio is not significant from 4000 to 2000 to 1000 S/s sampling rate and, thus, we opted to present the results for the 4000 S/s sampling rate only. The best option for data acquisition at the test site resulted to be the one with 4000 S/s and GL=2, because shorter GL resulted in too noisy data while larger GL in a significant loss of information in the high frequency range (Figure 2a), which is important for the present case study given the shallow height of the embankment. Then, the possibility of using all the 4 fibers in the same cable and stack their information was also evaluated. Figure 2b shows the comparison between stacked and non-stacked data. Clearly, the stacking enhances the quality of both the shot gathers and the f-k transform and will be adopted in future analyses.

Later, DAS data were also compared with the response obtainable with standard seismic instrumentation. With this respect in Figure 3a a comparison between a single channel along the fiber and a three-component geophone in a similar position are reported for a test seismic shot; in Figure 3b a comparison between average normalized spectra of all DAS channels and the same from the three-component geophones are shown. In both these results the different frequency content of the data can be clearly observed. Specifically, DAS data appear to show a marked reduction in the frequencies above 50 Hz, as already partially observed in the f-k transforms of Figure 2. This should be considered with attention in further tests, because losing information at high frequencies could hamper the capability of surface waves analysis to investigate the shallowest portions of the embankment.

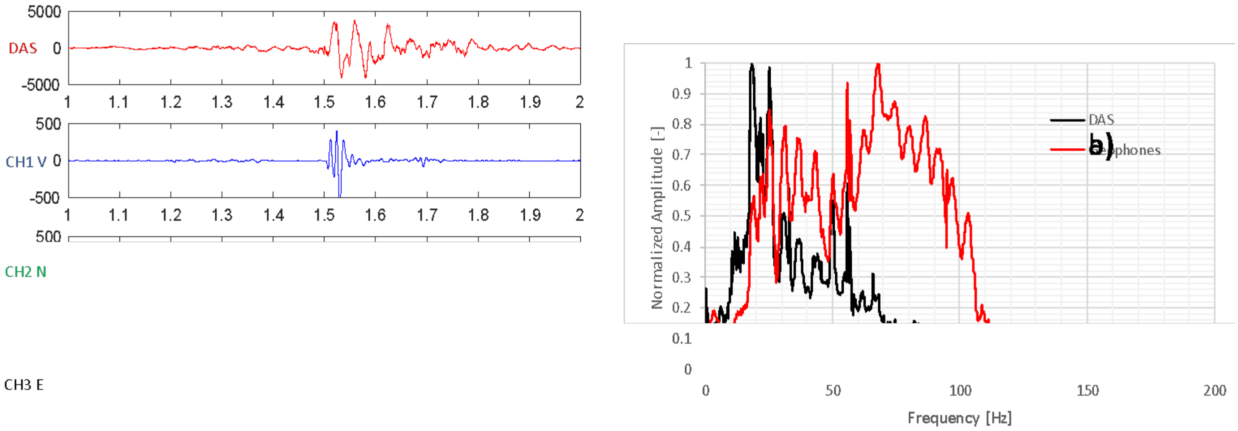

Figure 3 – Preliminary comparisons of DAS acquired data with standard seismic instrumentation: a) comparison between a single channel along the fiber and a three-component geophone in a similar position; b) average normalized spectra of all DAS channels in comparison with the same from standard geophones.

Conclusions

The installation and preliminary tests performed over a DAS cable in the Chivasso embankment test site are reported in this paper. Further tests are planned in the near future with a more extended active seismic survey over the whole embankment length and with a period of permanent monitoring of seismic noise sources to be used for seismic interferometry applications. The presence of highway and railway infrastructures is a clear advantage with this respect given timing and location of noise sources less aleatory.

Also, the presented test site is to be considered as an open field laboratory and different DAS acquisition approaches by the use of different interrogators are welcome to be tested at the site. In this aim also the raw data of the preliminary tests reported in the paper could be made available in open source for future usage.

Acknowledgements

This study was carried out within the GEOCHARME project – funded by the European Union – Next Generation EU within the PRIN 2022 program (D.D. 104 - 02/02/2022 Ministero dell'Università e della Ricerca). This manuscript reflects only the authors' views and opinions and the Ministry cannot be considered responsible for them.

Authors are indebted with the Po River Regional authority (AIPO) – Moncalieri section for the support in the identification of relevant case histories for the project and for the sharing of independent geotechnical and geophysical data overt the embankment.

Finanziato dall'Unione europea NextGenerationEU | Ministero dell'Università e della Ricerca | Italiadomani PIANO NAZIONALE DI RIPRESA E RESILIENZA

References

Cheng F., Guan J., Xia J., Zhu X., Fu J., Yu X., Tan L., He Z.; 2026: Advancing dam health monitoring with high-resolution Fiber-optic Distributed Acoustic Sensing. Engineering Geology, Vol. 360, 108462.

Roshdy, E., Majdanski, M., Długosz, S., Marciniak, A., Popielski, P.; 2025: Application of Distributed Acoustic Sensing for Active Near-Surface Seismic Monitoring. Sensors, Vol. 25, 1558.

Corresponding author: Cesare.comina@unito.it

Induced Polarization effects in airborne EM systems: fixed-wing and helicopter-borne measurements

Francesco Dauti[1], Tim Munday[2], Shane Mulè[2], Andrea Viezzoli[3], Gianluca Fiandaca[1]

[1] The EEMteam for Hydro & eXploration, Università degli Studi di Milano "A. Desio", Milano, Italy
[2]Commonwealth Scientific and Industrial Research Organization (CSIRO), Kensington, Perth, Australia
[3] EMERGO s.r.l., Cascina, Pisa, Italy

Introduction

Fixed-wing airborne electromagnetic (AEM) systems have been widely used to map subsurface conductivity from tenement to continental scales due to their efficiency in acquiring large, high-quality datasets (Lane et al., 2000). A notable example is the AusAEM program (Ley Cooper et al., 2019), which employs the TEMPEST™ system and has collected more than two million line-kilometres of data across Australia.

Airborne induced polarization (AIP) investigations have traditionally focused on helicopter-borne time-domain EM systems such as SkyTEM, whose concentric-loop geometry and low flight altitude allow accurate system characterization and reliable identification of subtle IP effects (e.g., Oldenburg and Kang, 2015; Macnae, 2016; Viezzoli et al., 2017; Cox et al., 2022). However, Dauti et al. (2025) demonstrated numerically that fixed-wing systems are also sensitive to IP effects over chargeable ground, producing negative responses and sharing a comparable field of sensitivity with helicopter-borne platforms.

In this work, we compare IP responses from helicopter-borne SkyTEM data with those from the fixed-wing TEMPEST™ system to assess how chargeability manifests across different AEM platforms and to evaluate the potential for extracting chargeability information from fixed-wing surveys. The TEMPEST™ system is considered due to its widespread global use and the availability of processed B-field X and Z components suitable for IP analysis (Lane et al., 2000).

The datasets analysed were acquired in the Kimba region, South Australia, using SkyTEM in 2022 and TEMPEST™ in 2008.

Methodology

The inductive datasets have been modelled using the EEMverter inversion scheme (Fiandaca *et al.*, 2023). In terms of inversion architecture, the scheme uses independent meshes to define the model parameters and to compute the forward responses during inversion. The parameters are mapped at the nodes of the model mesh and are linked to the forward mesh, located in correspondence of the acquired data, through a distance-dependent interpolation. This approach allows us to use, potentially, a different mesh for each model parameter while allowing different regularization or lateral and vertical discretization. This is especially useful for AIP inversions, where numerous parameters create strong equivalencies, making regularization and discretization essential to constrain possible solutions. The forward-model mesh uncoupling also allows us to link to the same model mesh(es) multiple forward meshes (one for each dataset that contributes to the inversion), possibly with different dimensionality (e.g. 1D for inductive data and 2D for galvanic data).

The inductive 1D forward response is computed following Effersø et al. (1999), accounting for the influence of the transmitter waveform, transfer function, and geometry, as well as the receiver filters and time gates, as further detailed in Sullivan *et al*. (2023). The forward computation is carried in frequency domain and is then transformed through Hankel transform in time domain (following Johansen & Sørensen, 1979). Variations in magnetic susceptibility are not modelled; the vacuum magnetic susceptibility (μ_0) is used to compute the responses. Although neglecting susceptibility effects is not entirely appropriate for our field example, where magnetic anomalies are present, deriving susceptibility solely from AEM data would lead to strong model-space equivalences during inversion procedures.

The model-space is parametrized using the Maximum Phase Angle (MPA) Cole-Cole re-parametrization (Fiandaca *et al.*, 2018) for both galvanic and inductive data. The ground is thus described with four parameters, $\{\rho,\phi,\tau_\phi,C\}$, where ρ is the ground resistivity (Ω·m), ϕ is the maximum phase between the real and imaginary part of the complex resistivity – representing the ground chargeability (expressed in mrad) – τ_ϕ (s) is the phase relaxation time and C the frequency dependence.

Numerical and survey data modelling results

To investigate how airborne induced polarization manifests in different AEM platforms, we first carried out a forward response analysis comparing the TEMPEST™ fixed-wing system and the helicopter-borne SkyTEM system. The aim was to examine how each system responds to the same polarized subsurface under controlled conditions. Forward responses were computed for an identical two-layer half-space model, ensuring that any differences in the observed behaviour arise from system characteristics (such as geometry, altitude, waveform, and measured observable) rather than from geological variability. For the TEMPEST™ system, the forward response was calculated both in terms of the magnetic field (B) and its time derivative (dB/dt), allowing a direct comparison with the SkyTEM responses. This provides a consistent framework for evaluating differences in amplitude, sign, and temporal evolution of the IP effects across systems. An example of this numerical study is shown in Fig. 1.

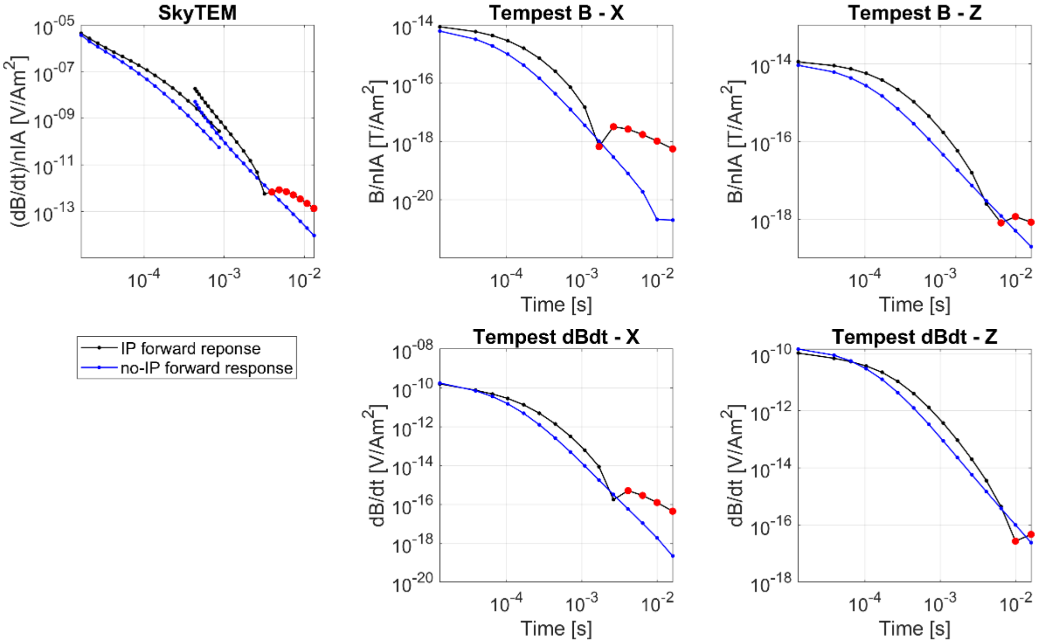

Fig. 1 – Forward response comparison relative to IP-affected (black) and non-IP-affected (blue) models for the TEMPEST™ fixed-wing and SkyTEM helicopter-borne systems. For TEMPEST™, both X and Z components are evaluated. Red markers denote negative measurements.

For the dispersive-resistivity model, the forward responses are computed for a two layers halfspace defined with a 30 m shallow chargeable layer ($\rho = 50\ \Omega\cdot$m; $\phi = 50$ mrad; $\tau_\phi = 0.001$ s; $c = 0.5$), representing the cover, over a purely resistive non-chargeable layer (1000 $\Omega\cdot$m) representing the basement. For the non-dispersive resistivity model, the forward responses are computed for the same model with a non-chargeable shallow layer (but with the same resistivity value). As visible from figure, for both systems IP effects produce negative secondary field responses at late times for both X and Z components. All the differences between the non-IP and IP responses are related to the ground polarizability, i.e., also for the TEMPEST^{TM} system the negatives are related to induced polarization effects. Not reported in this abstract, it is worth to mention that the ground polarization not always produce negative responses in both helicopter-borne and fixed-wing systems. For low ground chargeabilities (< 5 mrad) this does not happen, as also shown by Dauti *et al*. (2025). This can be consequence of the higher ground clearance of the fixed-wing systems and the processing routines.

The real TEMPEST^{TM} and SkyTEM survey data have been modelled including IP effects following the approach presented in the methodological section. The inversion used a consistent starting model for the two systems defined as a homogeneous halfspace with: $\rho = 50\ \Omega\cdot$m, $\phi = 10$ mrad, $\tau_\phi = 0.001$ s and $c = 0.5$, discretised in 21 layers (log-increasing thicknesses) from surface to 450 m at depth. The results for an overlapping TEMPEST^{TM} - SkyTEM line of about 30 km are visible in Fig. 2. As mentioned in the introduction, AIP modelling of HTEM data is presently more advanced, and we therefore use SkyTEM's AIP inversion results as a benchmark to prove the reliability of TEMPEST^{TM} chargeability model. SkyTEM's data contains also here some late time negatives in the HM channel (as visible in red in figure 4) that can be uniquely relatable with IP effects for helicopter systems. In this dataset, the TEMPEST^{TM} data do not contain negatives.

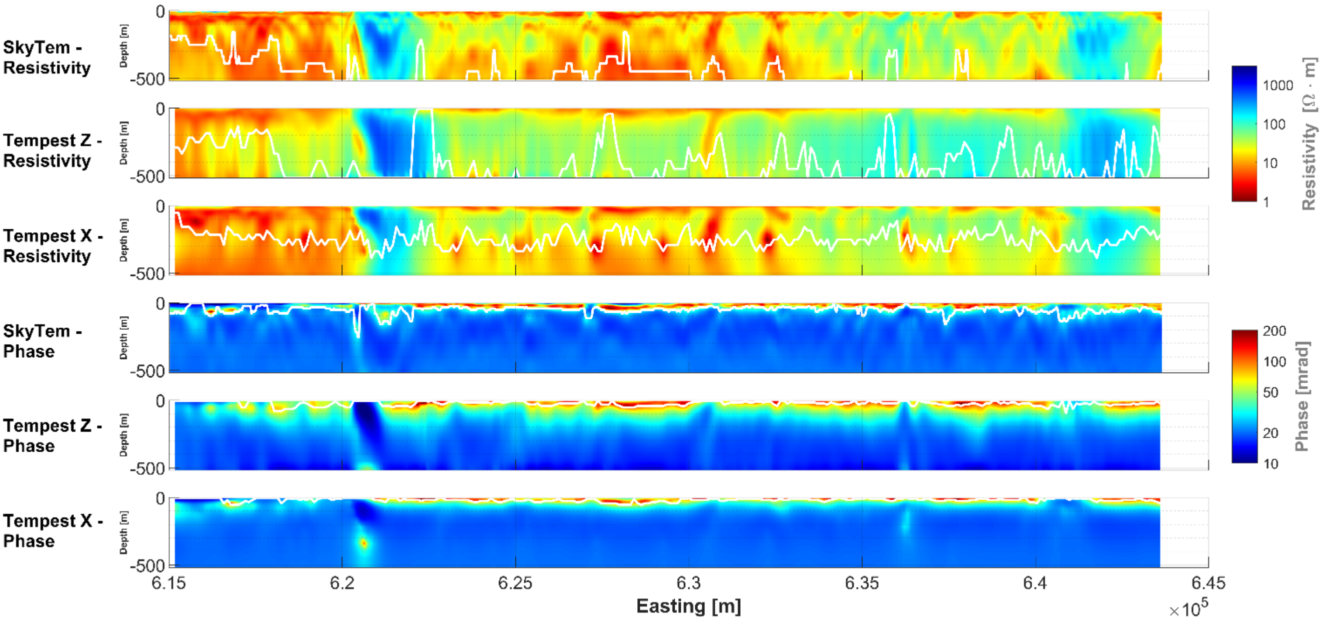

Fig. 2 – Inversion results of an overlapping TEMPESTTM and SkyTEM survey line. Both resistivity (top three panels) and chargeability (bottom three panels) are shown. The white line indicates the depth of investigation computed as in Fiandaca et al. (2015).

As shown in Figure 2, the SkyTEM and TEMPEST™ resistivity and chargeability models are in good agreement for both parameters. Notably, the TEMPEST™ X component recovers a resistivity structure that closely matches that obtained from the helicopter-borne system. The ground-derived chargeability correlates well with the distribution of transported regolith across the area, which typically produces measurable polarization responses. These clay- and oxide-rich sediments are well-known sources of IP effects in Australian AEM datasets and require dispersive resistivity modelling to accurately resolve their thicknesses in ground-based imaging. Consistent chargeability responses are observed between the systems even in areas where negative responses are absent in the data space.

The obtained data-fit retrieved by inversion is very good, with data-misfits below 1 for both systems. The last-iteration forward response versus the measured data is visible in figure 4.

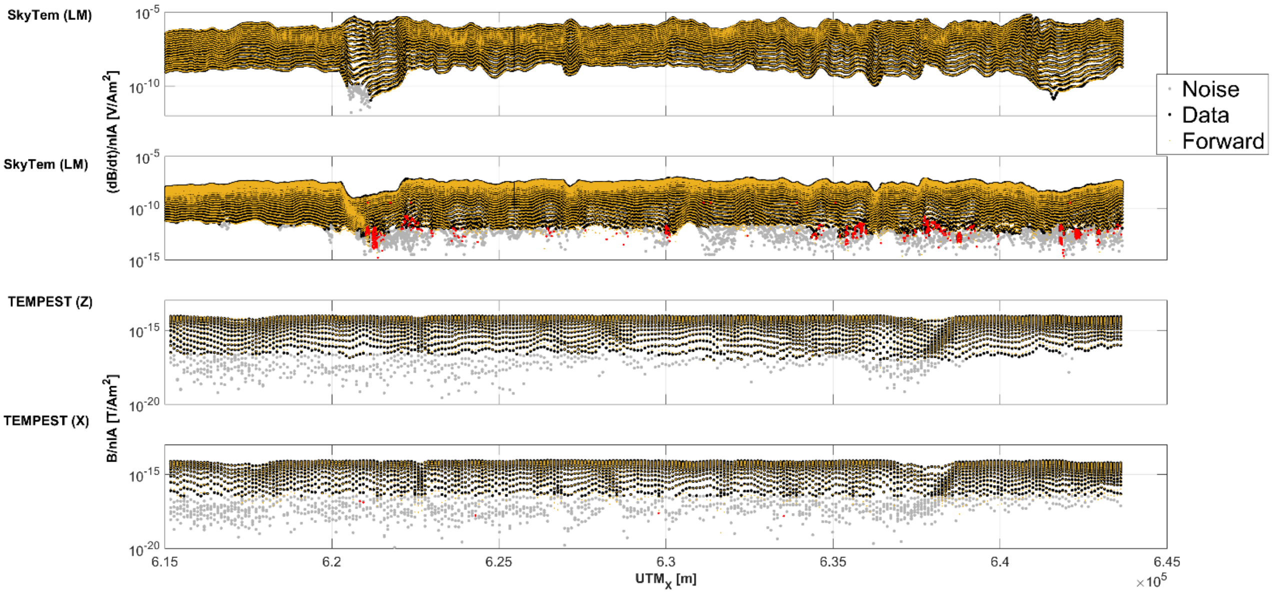

Fig. 3 – Last iteration inversion data fit for the SkyTEM Low Moment (LM), High Moment (HM) and TEMPESTTM X and Z components. The removed data are in grey, the forward response in yellow and the measured data in black. The red dots are the negative recordings.

In figure 3, in gold is shown the forward response while in black the measured data. As visible, a very good fit is retrieved for both datasets and TEMPEST^{TM} components.

Conclusions

The results show strong agreement between SkyTEM and TEMPEST™ in recovering both resistivity and chargeability, despite differences in system configuration and acquisition geometry. The TEMPEST™ X component retrieves resistivity models comparable to those from the helicopter-borne SkyTEM system, while chargeability responses from both datasets consistently map transported regolith units. This agreement, including in areas without negative responses in the data space, confirms the robustness of the recovered models and supports the complementary use of both systems for subsurface characterization.

References

Brodie, R., Ley Cooper, Y. 2019. AusAEM Year 1: Some aspects of quality control and calibration, AEGC 2019.

Christensen, N. K., Minsley B. J., and Christensen S. (2017), Generation of 3-D hydrostratigraphic zones from dense airborne electromagnetic data to assess groundwater model prediction error, Water Resour. Res., 53, 1019–1038, doi:10.1002/2016WR019141.

Cox, L., Zhdanov, M., Pitcher, D., Niemi, J., Three-Dimensional Inversion of IP effects in AEM using the GEMTIP Model. Minerals

Dauti F., Ley Cooper Y., Munday T., Viezzoli A., Fiandaca G., 2025, Induced polarization effects in fixed-wing airborne EM: the TEMPEST^{TM} system – Part A, connecting numerical modelling with field evidence at continental scale, Geophysical Journal International, 2025, ggaf495, https://doi.org/10.1093/gji/ggaf495

Effersø, F., Auken, E. and Ingvard Sørensen, K. (1999), Inversion of band-limited TEM responses. Geophysical Prospecting, 47: 551-564. https://doi.org/10.1046/j.1365-2478.1999.00135.x

Fiandaca, G., Ramm, J., Binley, A., Gazoty, A., Christiansen, A. V., & Auken, E. (2013), Resolving spectral information from time domain induced polarization data through 2-D inversion. Geophysical Journal International, 192(2), 631-646, https://doi.org/10.1093/gji/ggs060

Fiandaca, G., Christiansen, A., V., Auken, E., (2015), Depth of Investigation for Multi-parameters Inversions, European Association of Geoscientists and Engineers, Near Surface Geoscience 2015 - 21st European Meeting of Environmental and Engineering Geophysics, 2015, p.1 – 5, https://doi.org/10.3997/2214-4609.201413797

Fiandaca, G., Madsen, L.M. and Maurya, P.K. (2018), Re-parameterisations of the Cole–Cole model for improved spectral inversion of induced polarization data. Near Surface Geophysics, 16: 385-399. 3(1), 17-34.

Fiandaca, G., Zang, B., Chen, J., Signora, Al., Dauti, F., Galli, S., Sullivan, N., Bollino, A., Viezzoli, 2023, A.Closing the gap between galvanic and inductive methods: EEMverter, a new 1D/2D/3D inversion tool for Electric and Electromagnetic data with focus on Induced Polarization. AEM 2023, Fitzroy Island.

Johansen, H. K., and Sørensen, K., (1979). Fast hankel transforms. Geophysical Prospecting, 27(4), 876–901. https://doi.org/10.1111/J.1365-2478.1979.TB01005.X

Lane, R., Green, A., Golding, C., Owers, M., Pik, P., Plunkett, C., Sattel, D., Thorn, B. (2000). An example of 3D conductivity mapping using the TEMPEST airborne electromagnetic system. Exploration Geophysics, 31(1–2), 162–172. https://doi.org/10.1071/EG00162

Ley-Cooper, A. Y., Brodie, R. C., and Richardson, M. (2019), AusAEM: Australia's airborne electromagnetic continental-scale acquisition program. Exploration Geophysics, 51(1), 193–202. https://doi.org/10.1080/08123985.2019.1694393

Macnae, J. 2016, 'Quantitative estimation of intrinsic polarization and superparamagnetic parameters from airborne electromagnetic data', Geophysics 81(6), E433-E446.

Madsen, L. M., Fiandaca, G., and Auken, E. (2020), 3-D time-domain spectral inversion of resistivity and full-decay induced polarization data—full solution of Poisson's equation and modelling of the current waveform. Geophysical Journal International, 223(3), 2101-2116.

Mulè S., Smiarowski, A., (2013) Evolution of TEMPEST. ASEG Extended Abstracts 2013, 1-5.

Oldenburg, D. W. and Kang, S. 2015, 'Recovering IP information in airborne-time domain electromagnetic data', 24th ASEG-PESA meeting - Perth, Extended Abstract.

Smith, R. S., and West, G. F. (1988), TEM Coincident Loop Negatives and the Loop Effect. Exploration Geophysics, 19(1–2), 354–357. https://doi.org/10.1071/EG988354

Sullivan N. A. L., Gisolo M., Spagnoli L., Rapiti A., Dauti F., Menghini A., Viezzoli A. and Fiandaca G. (2023), Airborne EM in northern Italy for sustainable and resilient management of groundwater resources, Nuovo Cimento, Year 2023 - Issue 3 - May-June SIF Congress 2022, Article 68, p.1–11

Viezzoli, A., V. Kaminski, and G. Fiandaca, 2017, Modeling induced polarization effects in helicopter time domain electromagnetic data: Synthetic case studies: Geophysics, 82, no. 2, E31–E50.

Zhang, B., Engebretsen, K. W., Fiandaca, G., Cai, H., and Auken, E. (2021), 3D inversion of time-domain electromagnetic data using finite elements and a triple mesh formulation. Geophysics, 86(3), E257-E267.

Corresponding author: Francesco Dauti (francesco.dauti@unimi.it)

Passive seismic monitoring of a potentially unstable rock slope in Skagway, Alaska

Lorena Di Toro[1], **Chiara Colombero**[1], **Jeffrey R. Moore**[2]

[1]*Politecnico di Torino – Department of Environment, Land and Infrastructure Engineering, Torino, Italy*
[2]*University of Utah – Department of Geology and Geophysics, Salt Lake City, Utah, USA*

Introduction and site description

Rockfall events are common in a wide range of geological settings characterized by steep, rocky slopes. Post-glacial landscapes feature such hazards during deglaciation: when ice retreats from the valley walls, it removes lateral support to the slopes causing periodic small-scale rockfall events. This process is documented in many areas of southeast Alaska, specifically in the narrow glacial valley of Skagway, characterised by steep rock slopes on both the east and west sides (Figure 1a). In recent years, the town has experienced many rock detachments from the eastern slope above the harbour, impacting the cruise ship dock below. Therefore, this area was chosen for a dense geophysical characterization through passive seismic measurements, as it represents the most active zone, featuring extensive fracturing and progressive toppling failure with a stair-stepped geometry.

Passive seismic monitoring techniques are now widely used to monitor slope instabilities by deploying spatially distributed sensors that continuously record ambient seismic noise (Colombero et al. 2021). Spectral analysis of the recorded signals allows for the identification of spectral peaks potentially linked to resonance phenomena while cross-correlation analysis helps in extracting seismic velocity changes within the investigated body (Lévy et al. 2010; Burjánek et al. 2018; Colombero et al. 2017). These seismic parameters can both exhibit reversible variations in response to external modifications in climate factors, such as air temperature and precipitation, providing insights into the dynamic behaviour of the site. In addition, the continuous ambient seismic noise recordings mainly contain surface waves. The analysis of their propagation is a valuable approach for detecting and imaging local sharp lateral variations and subsurface heterogeneities, such as cavities, fractures and faults (Colombero et al. 2019). In this study we applied two SW-based attributes, namely energy and autospectrum, which can be directly applied to raw data without any preprocessing. Energy concentrations are expected at fracture locations because of back reflections at the fracture interfaces and energy trapping inside the low velocity material, and similar behaviours can be observed in the autospectrum as a function of frequency, and consequently depth, of the fracture.

To monitor the slope instability, a temporary seismic array was deployed at the study site (Fig. 1b-c). The array consists of 30 Fairfield Zland 5-Hz nodal geophones recording three-component ambient vibration data in two different configurations, at a sampling rate of 500 Hz. Configuration 1 recorded for ~24 hours on 18 September 2023 and was used to compute attributes of surface waves, as its geometry spans the slope (Figure 1b). Seismic stations of configuration 2 worked for approximately ~ 35 days between 19 September and 25 October 2023 and were used to apply spectral analysis and cross-correlation analysis of ambient seismic noise (Figure 1c). The resulting observations were then compared to air temperature variations and precipitation data to better understand the dynamic behaviour of the site.

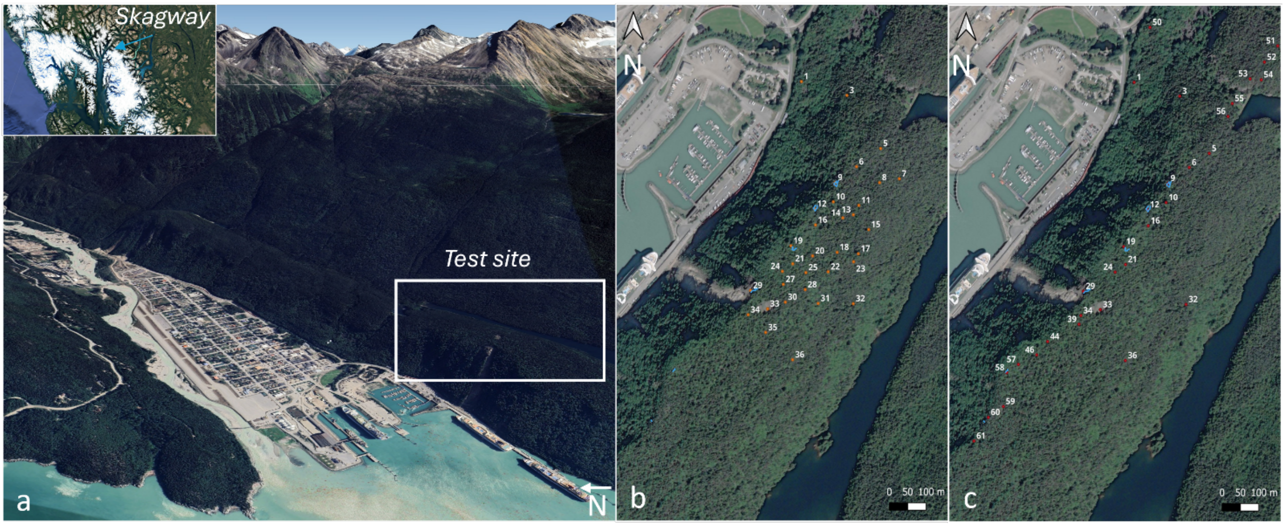

Figure 1 – a) Geographic location of the study site (Skagway, Alaska, USA) with the slope area delineated by the white rectangle. b) Configuration 1 of the temporary seismic array showing nodal geophones (red dots), and mapped fractures (blue lines). c) Configuration 2 of the longer-term array with nodal geophones (orange dots), and mapped fractures (blue lines).

Methods

Spectral analysis and cross-correlation analysis of ambient seismic noise recorded by the longer-term array (Figure 1c) were performed to investigate the dynamic behaviour of the slope and study its response to meteorological factors. Continuous seismic recordings were first divided into consecutive time windows, and Fast Fourier Transforms (FFTs) were computed for each component of the monitoring stations. From the Fourier amplitude spectra, horizontal-to-vertical spectral (H/V) spectral ratios were calculated combining the two horizontal components and normalizing them by the vertical component. Probability density functions (PDFs) of the H/V spectral ratios were then computed to identify spectral peaks, which may be interpreted as resonance frequencies of the slope. In addition, time-dependent H/V ratios were analyzed to investigate temporal variations in resonance frequencies and their potential correlation with meteorological parameters.

Cross-correlation analysis was performed in 2-Hz frequency bands of the [0.5, 20.5] Hz frequency range of the north (N) components of station pairs. For each group of three aligned stations, the central one was selected as the reference. Hourly cross-correlograms were therefore computed for the two adjacent station pairs, between the southern and central stations and between the central and northern stations and then filtered in 2-Hz bands. Seismic velocity changes (dV/V) were estimated using the stretching technique between time intervals [-1.0, – 0.5] s and [+0.5, +1.0] s to work on coda waves.

Finally, to detect heterogeneities such as cavities and fractures, attributes of surface waves were computed using data acquired along configuration 2 profile.

The energy E_i is computed for each passive receiver 1-hour vertical trace i as the sum of the squared amplitude $A_{t,i}$ as:

$$E_i = \sum_f \left|A_{t,i}\right|^2 \qquad (1)$$

For each hour, the energy is normalized to the maximum E_i to balance the contribution of each hour of recording in the results. After normalization, E_i of all the available hours of recordings are stacked to improve data readability.

An alternative way to display energy content as a function of the frequency is the autospectral density G_i, that is then computed as the sum of the squared real and imaginary parts of the discrete Fourier transform Y of the signal (Zerwer et al., 2005):

$$G_i(f) = \{Re[Y_i(f)]\}^2 + \{Im[Y_i(f)]\}^2 \qquad (2)$$

As for energy computation, the autospectral density was computed for each receiver on the 1-hour vertical recordings and then stacked to improve data interpretation.

Results

The results of spectral analysis and cross-correlation analysis of ambient seismic noise are summarised in Figure 2. The horizontal-to-vertical spectral ratio (H/V) is shown for the nodal geophone 16 (Fig. 2b), while seismic velocity changes (dV/V) are the results of cross-correlation between seismic stations 16 and 19 (Fig. 2c). Both these seismic parameters are compared with hourly averaged air temperature and precipitation data shown in the first panel.

The hourly H/V results reveal a strong spectral amplification at 3 Hz and a less amplified peak around 5 Hz. The temporal evolution of both peaks seems to be related to air temperature variations, as they almost disappear during the final days of the period of observation, when temperature drops.

Cross-correlation results are shown in two successive 2-Hz frequency bands ([4 6] Hz and [6 8] Hz). Correlation coefficients are higher for the velocity changes estimated in the lower frequency band (Fig. 2d). The values of dV/V follow a daily pattern for the whole period, oscillating between approximately -1% and +5%, but slightly decreasing during the final days for both the frequency bands.

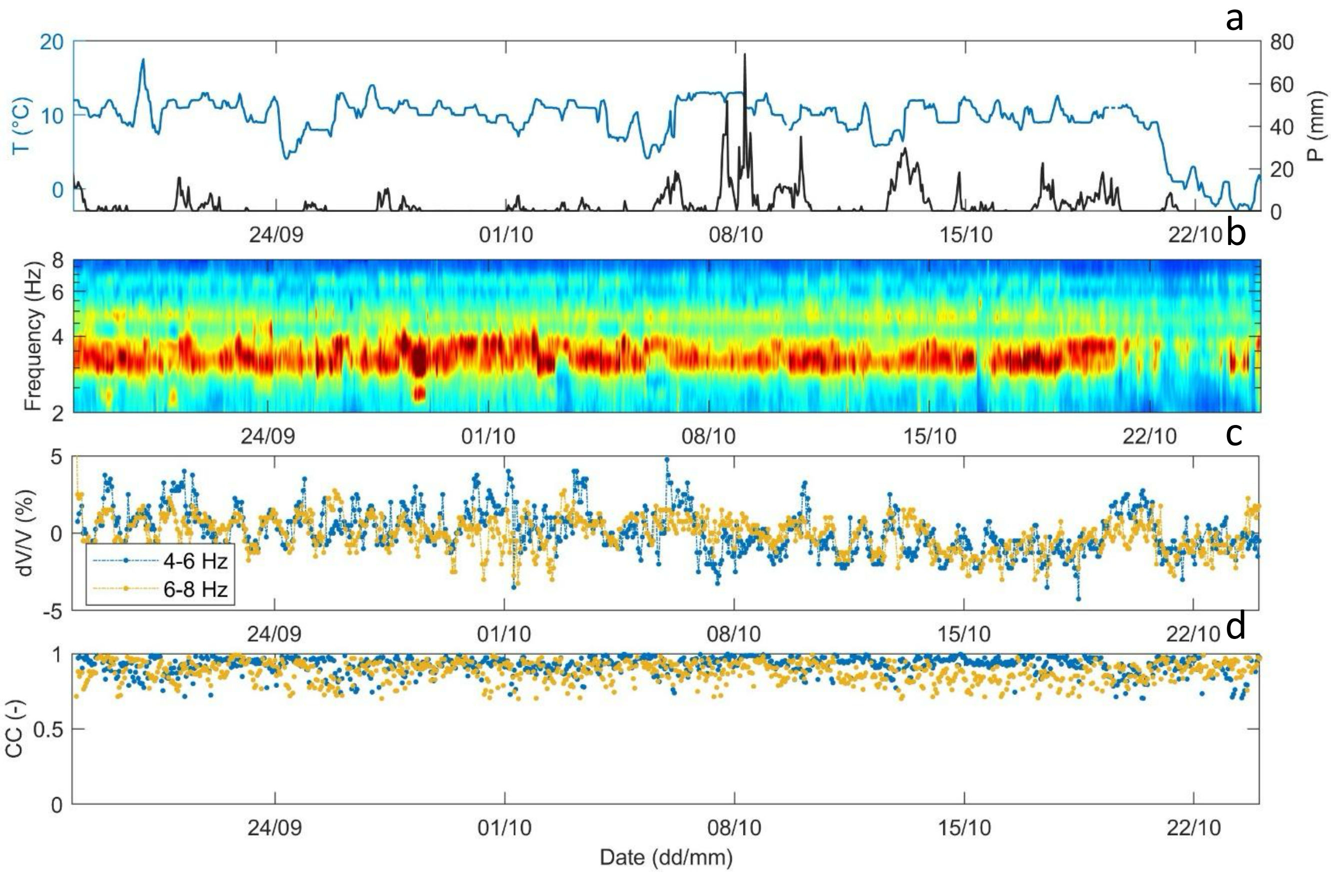

Figure 2 – Comparison of ambient seismic noise results with meteorological variations. (a) hourly air temperature variations (blue) and precipitation (black) at the nearest meteorological station (Haines Airport). (b) Zoom of H/V spectral ratio of geophone 16. (c) Seismic velocity changes retrieved from cross-correlation of ambient seismic noise between station 16 and 19 in two frequency bands. (d) related cross-correlation coefficients in the two frequency bands.

Results of surface waves attributes computed on the temporary array are shown in Figure 3. The spatial distribution of energy is not uniform and shows high values occurring in the central portion of the array (Fig. 3a). The interpolated autospectral map at 10 Hz (Fig. 3b) is showing anomalies in correspondence with the main energy concentrations. These anomalies may indicate changes in the frequency content which can be associated with different mechanical properties or the presence of heterogeneities, which can cause scattering or partial energy trapping.

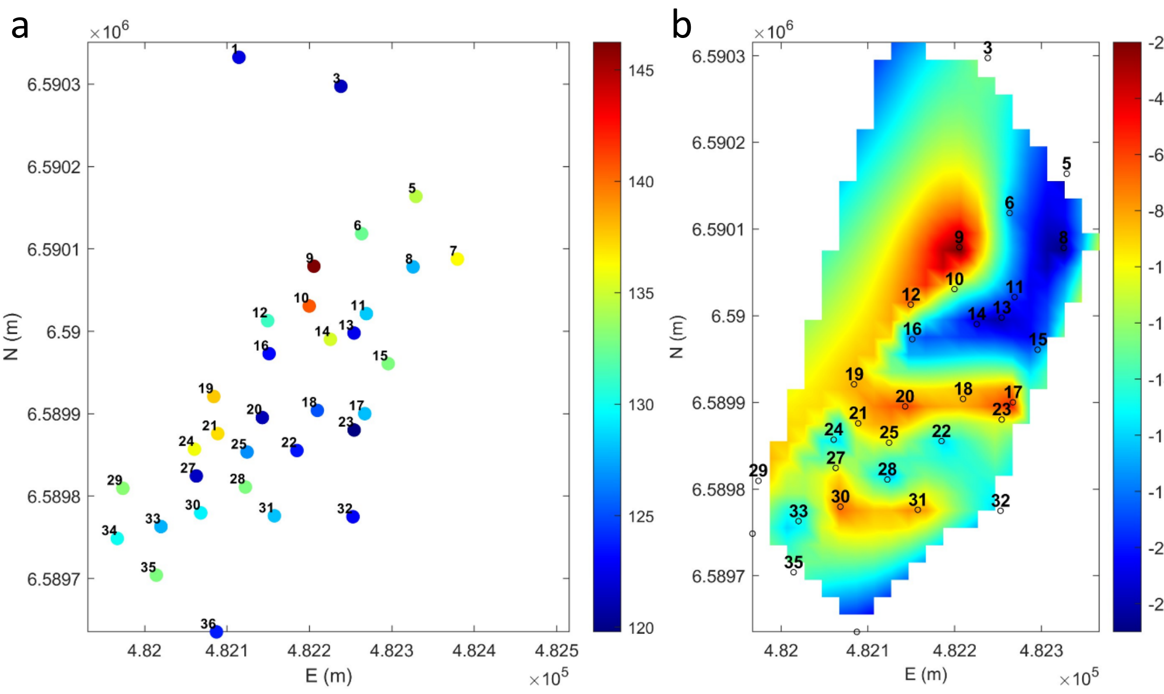

Figure 3 – Results of surface wave analysis. (a) spatial distribution of energy computed at each receiver as a function of geographic coordinates. (b) interpolated autospectrum map at 10 Hz over the study area. Receiver labels are indicated by numbers in both panels.

Conclusion

In this study, passive seismic monitoring was used to investigate the dynamic behaviour and structural heterogeneity of an unstable rock slope in a post-glacial environment.

Spectral analysis and cross-correlation analysis of ambient seismic noise revealed temporal variations in resonance frequencies and seismic velocity changes, which appear to be affected by air temperature variations.

Surface-wave attributes highlighted spatial variations within the investigated area. The non-uniform distribution of energy and the presence of autospectrum anomalies may indicate localized zones with heterogeneity, likely related to fractured rock volumes.

Overall, the combined use of ambient seismic noise analysis and surface-wave attributes represents a valuable approach for understanding slope instability processes. Further analysis and extended monitoring may help to improve the interpretation of seismic parameters and their implications for slope stability.

References

Colombero C., Jongmans D., Fiolleau S., Valentin J., Baillet L., Bièvre G.; 2021: Seismic noise parameters as indicators of reversible modifications in slope stability: a review. Surveys in Geophysics, 42, 339–375, https://doi.org/10.1007/s10712-021-09632-w.

Burjánek J., Gischig V., Moore J.R., Fäh D.; 2018: Ambient vibration characterization and monitoring of a rock slope close to collapse. Geophysical Journal International 212(1), 297-310, https://doi.org/10.1093/gji/ggx424.

Colombero C., Baillet L., Comina C., Jongmans D., Vinciguerra S.; 2017: Characterization of the 3-D fracture setting of an unstable rock mass: from surface and seismic investigations to numerical modeling. J. Geophys. Res. Solid Earth, 122(8), 6346–6366, https://doi.org/10.1002/2017JB014111.

Colombero, C., Comina, C., Valentina Socco, L.; 2019: Imaging near-surface sharp lateral variations with surface-wave methods—Part 1: Detection and location. Geophysics, 84(6), EN93-EN111, https://doi.org/10.1190/geo2019-0149.1.

Lévy C., Baillet L., Jongmans D., Mourot P., Hantz D.; 2010: Dynamic response of the Chamousset rock column (Western Alps, France). Journal of Geophysical Research 115, F04043, https://doi.org/10.1029/2009JF001606.

Zerwer, A., M. A. Polak, J. C. Santamarina; 2005: Detection of surface breaking cracks in concrete members using Rayleigh waves: Journal of Environmental and Engineering Geophysics, 10, 295–306, https://doi.org/10.2113/JEEG10.3.295.

Corresponding author: lorena.ditoro@polito.it

Microtremor surveys and dense nodal acquisition to resolve the subsurface structure of the Colfiorito and Annifo basins (central Italy).

Maurizio Ercoli[1], **Giuseppe Di Giulio**[2], **Massimiliano Porreca**[1], **Elham Safarzadeh**[1], **Giorgio Alaia**[1], **Carlo Alberto Brunori**[3]

[1] *Dipartimento di Fisica e Geologia, Università degli Studi di Perugia, Perugia, Italy.*
[2]*Istituto Nazionale di Geofisica e Vulcanologia (INGV), sede di L'Aquila, Italy.*
[3] *Istituto Nazionale di Geofisica e Vulcanologia (INGV), sede di Perugia, Italy.*

Extensive surveys of microtremor recordings can contribute to depict the deep structure of active Quaternary intramountain basins. This study focuses on two sites in central Italy, the Colfiorito and the Annifo basins, which were struck by a significant seismic sequence in the 1997-1998 (Messina et al., 2002). In the framework of the First ILGE TNA-NOA Access Call, a dense passive seismic dataset was collected in 2024 aiming to improve the geologic characterization of such two basins. The microtremors acquisition, whose recording duration varied from a few hours up to 2 days, was carried out through a total of 160 single-station measurements, collected during 6 days of fieldwork and using 48 seismic nodes, equipped with 4.5 Hz triaxial sensors. Two seismic arrays of nodes with helicoidal geometries were deployed in the northern part of the Colfiorito plain, whilst one was collected in the southern sector of the Annifo area, to define accurate shear-wave profiles at depth (Di Giulio et al., 2003; 2006). Two additional seismic stations were also set up, equipped with medium-period (5s) Lennartz seismometers and Reftek datalogger, which were left in the field for a few days. Data analysis performed using the H/V Nakamura technique highlights distinct results for the two study areas. The Colfiorito basin shows two main H/V frequency ranges, the first included within 1.0-6.0 Hz, and the second approximately in the range 0.6-1.0 Hz located in the center of the basin (NW-SE direction). The Annifo basin shows H/V frequency peaks greater than 1.0 Hz, and a depocenter is in the southern portion of study area. Regarding the Colfiorito plain, our results show a distribution of the resonant frequencies that agrees with a recent gravimetric study by Di Filippo et al. (2025) founding two important gravimetric minima in the central sector of the basin.

Acknowledgments

This publication results from work carried out under transnational access/national open access action under the support of WP3 ILGE - MEET project, PNRR - UE Next Generation Europe program, MUR grant number D53C22001400005.

References

Di Filippo, M., Mancinelli, P., Cavinato, G. P., Pauselli, C., Sabatini, A., Mirabella, F., De Franco R., & Barchi M. R.; 2025: Bouguer gravity anomaly in the Colfiorito Quaternary continental basin, northern Apennines, central Italy. Journal of Maps, Vol. 21, n. 1, pp. 2503244, https://doi.org/10.1080/17445647.2025.2503244.

Di Giulio, G., Rovelli, A., Cara, F., Azzara, R. M., Marra, F., Basili, R., and Caserta A.; 2003: Long-duration asynchronous ground motions in the Colfiorito plain, central Italy, observed on a two-dimensional dense array. J. Geophys. Res., Vol 108, n. B10, pp. 2486, doi:10.1029/2002JB002367.

Di Giulio, G., Cornou, C., Ohrnberger, M., Wathelet, M., & Rovelli, A.; 2006: Deriving wavefield characteristics and shear-velocity profiles from two-dimensional small-aperture arrays analysis of ambient vibrations in a small-size alluvial basin, Colfiorito, Italy. Bulletin of the Seismological Society of America, Vol. 96, n. 5, pp. 1915–1933, https://doi.org/10.1785/0120060119.

Messina, P., Galadini, F., Galli, P. A. C., & Sposato, A.; 2002: Quaternary basin evolution and present tectonic regime in the area of the 1997–1998 Umbria–Marche seismic sequence (central Italy). Geomorphology, Vol. 42, n. 1-2, pp. 97–116, https://doi.org/10.1016/S0169-555X(01)00077-0.

Corresponding author: maurizio.ercoli@unipg.it

Monitoring of the saline wedge in the rivers of the Ferrara province (Emilia Romagna region, Italy).

Francesca Fongo[1] **and Enzo Rizzo**[1]

[1] *University of Ferrara (Dipartimento di Fisica e Scienze della Terra, Ferrara, Italy)*

Introduction

Saltwater intrusion represents a global threat to coastal ecosystems and water resources, made worse by climate change. Rising sea levels and reduced river flows alter the water balance in transition zones between rivers and the sea, allowing seawater to move upstream into rivers and coastal aquifers. Recent studies (Lee et al., 2025) predict a global average increase of 9.1% in saltwater intrusion under high emissions scenarios, with sea level rise contributing about twice as much as reduced river flow. Extreme intrusion events that currently happen once every 100 years are expected to become up to 25 times more frequent in most of the world's estuaries. To prevent or reduce the degradation of both surface and groundwater quality due to saltwater contamination, research has been conducted to fully understand the problem, identify key parameters, and evaluate possible corrective measures. The Po River Delta is a representative case of this vulnerability. The Ferrara area, characterized by minimal slopes and elevations mostly below sea level, is particularly exposed to this phenomenon. Climate projections indicate that the Po di Goro estuary could see an increase in saltwater intrusion of up to 63% annually and 120% in summer (Verri et al., 2024). The 2022 drought event highlighted the system's fragility, with saltwater reaching inland areas and compromising the use of river water for irrigation and domestic purposes. Saltwater intrusion into coastal aquifers is further worsened by excessive use of groundwater resources for human activities and reduced natural recharge due to climate change (Crestani, 2022). The consequences include compromised drinking water quality, damage to agricultural crops, alteration of natural habitats, and soil degradation processes. Reducing current or predicted negative effects can only be achieved through careful policies focused on coastal defense, flood mitigation, reduction of human-induced subsidence, and control of saltwater intrusion (Simeoni, 2009). River water salinity is currently measured using probe systems that evaluate water conductivity (EC). Traditional river salinity monitoring systems are based on point measurements of electrical conductivity (EC) using a moving boat approach, which provides low spatial and temporal resolution data, inadequate for accurate saltwater wedge modeling. These methods also require long acquisition times and are inefficient for systematic monitoring at the territorial scale.

Geophysical methods, particularly electrical resistivity tomography (ERT) and electromagnetic survey, offer an innovative alternative for rapid, high-resolution mapping of saltwater intrusion. Rizzo et al., 2023 demonstrated the usefulness of the combined ERT-FDEM approach in the Po di Goro to identify the advancement of the saltwater wedge and monitor its dynamic evolution in the subsurface. Mansourian et al., 2022 confirm the validity of these methods for delimiting saline domains in coastal areas. The integration of different geophysical techniques (ERT, FDEM, GPR) allows for multi-scale and multi-parameter characterization of the phenomenon, overcoming the limitations of individual techniques.

Objectives and expected results

This research activity is part of a PhD project, which aims to develop an integrated system for monitoring and predictive modeling of saltwater wedge intrusion in the Ferrara area, through the application of advanced geophysical methods and machine learning techniques. The new project will continue the previous long-term monitoring of saltwater intrusion in the Po di Goro (2022-2025) using only the FDEM method. The research project plans to continue these activities by introducing other geophysical methods, such as ERT and GPR, and extending them to other rivers in the Ferrara area (fig. 1).

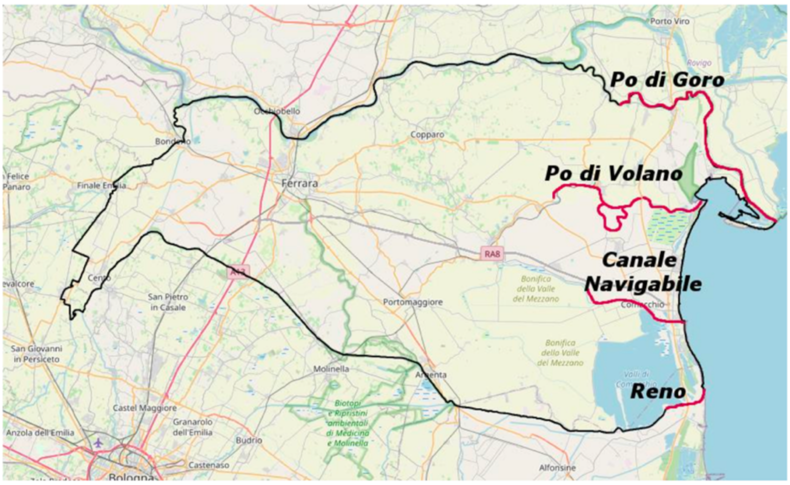

Fig 1 – Ferrara territory with the monitored rivers (Bignami et., 2019)

Expected results include: (1) precise mapping of the extent and depth of the saltwater wedge in the Ferrara area and quantification of its temporal evolution; (2) development of machine learning-based predictive tools to forecast the future evolution of saltwater intrusion, with identification of critical thresholds and main drivers; (3) provision of concrete tools (predictive scenarios) to support sustainable water resource management, agriculture, and territorial planning. The developed methodologies are transferable to other estuaries and deltas at national and international levels.

The project's originality lies in the innovative integration of high-resolution rapid geophysical methods with advanced machine learning techniques for monitoring and predicting saltwater intrusion. The project addresses a critical gap in coastal water resource management: the lack of systematic monitoring systems and reliable predictive tools. The increasing frequency of salinization episodes highlights the urgency of developing robust predictive capabilities that allow for preventive interventions. From an applied perspective, the project directly responds to the needs highlighted by the 2022 water crisis in the Po River basin and the alarming projections for the coming decades.

References

Bignami, D. F.; Rosso, R.; Gandolfi, C.; 2019: *Intrusione salina: le sfide dei territori della costa*. Politecnico di Milano, Dipartimento di Ingegneria Civile e Ambientale, Milano.

Crestani, E.; 2022: Large-Scale Physical Modeling of Salt-Water Intrusion. *Water*, Vol. 14, n. 8, 1183.

Lee, J.; Biemond, B.; van Keulen, D.; Huismans, Y.; van Westen, R. M.; de Swart, H. E.; Dijkstra, H. A.; Kranenburg, W. M.; 2025: Global increases of salt intrusion in estuaries under future environmental conditions. *Nature Communications*, Vol. 16, 3444, https://doi.org/10.1038/s41467-025-58783-6

Mansourian, D.; Hamidi, A.; Makarian, E.; Namazifard, P.; 2022: Geophysical surveys for saltwater intrusion assessment using electrical resistivity tomography and electromagnetic induction methods. Journal of the Earth and Space Physics, Vol. 48, n. 3, pp. 331–341, https://doi.org/10.22059/JESPHYS.2022.324755.1007328

Rizzo, E.; Boldrin, P.; Bondesan, A.; Droghetti, F.; Capozzoli, L.; De Martino, G.; Ferrari, E.; Fornasari, G.; Giampaolo, V.; Neri, F.; 2023: DC and FDEM salt wedge monitoring of the Po di Goro river (Italy). Abstract presented at *EGU General Assembly 2023*, Vienna (Austria), 24–28 April, EGU23-5297, https://doi.org/10.5194/egusphere-egu23-5297

Simeoni, U.; 2009: A review of the Delta Po evolution (Italy) related to climatic changes and human impacts. *Geomorphology*, Vol. 107, n. 1–2, pp. 64–71.

Verri, G.; De Lorenzis, A.; Santos da Costa, V.; Sorolla, A.; Löchner, A.; Ribot, M.; Martí, E.; Delgado, S. C.; Coppini, G.; Pinardi, N.; 2024: Salt-wedge estuary's response to rising sea level, reduced discharge, and Nature-Based Solution. *Frontiers in Climate*, Vol. 6, Article 1408038, https://doi.org/10.3389/fclim.2024.1408038

Corresponding author: francesca.fongo@unife.it

A classification of GPR pitfalls for better and more responsible usage

Emanuele Forte[1], Michele Pipan[1]

[1]*Department of Mathematics, Informatics, and Geosciences, University of Trieste, Trieste, Italy*

1. Introduction and motivation

Ground Penetrating Radar (GPR) is a high-resolution, non-invasive geophysical method widely used for subsurface imaging in geology, geomorphology, engineering, hydrology, and archaeology. Despite its versatility and popularity, GPR data face physical, environmental, and methodological limits that can compromise interpretation if not properly considered and addressed. An awareness of these pitfalls is therefore essential to avoid misinterpretation and to ensure reliable reconstructions.

The most serious problem of GPR equipment is the achievable penetration depth, as GPR signals cannot always penetrate all materials (e.g., Jol, 2009). This is directly related to the physical limitations on the propagation of electromagnetic (EM) waves into electrically conductive media and can only be partially mitigated by lowering the frequency of the exploited signal.

In addition to this point and the issues common to the other geophysical techniques, such as a lack of target contrast and possible low signal-to-noise ratios, it has long been recognised that GPR has some peculiar limitations. For instance, Annan, 2001 remarked that often only relative amplitudes can be extracted from GPR dataset, while absolute amplitude information is more challenging. Specific issues have been reported for void detection across different environments and applications (Nobes, 2018), for archaeological surveys such as the location of graves and burials (Martindale et al., 2024) and for the detection of linear structures (Leckebusch, 2011). Other specific problems have been reported about the actual possibility of differentiating between signal and coherent noise components (e.g., Radzevicius et al., 2000; Forte and Pipan, 2017), for GPR tomography (Nuzzo et al., 2008) and estimating EM velocity and target depth (e.g., Xie at al., 2018). Although previous work has identified various pitfalls associated with GPR, a clear, comprehensive description or classification of these challenges remains lacking. The main aim of this contribution is to begin addressing this gap by systematically outlining the major issues currently faced in GPR applications.

2. Pitfalls classification

When classifying GPR pitfalls, it is important to consider not only the inevitable subjectivity of data interpretation, but also all the factors that can lead to inaccurate or incorrect information being extracted from GPR data. Figure 1 provides a comprehensive, though not exhaustive, overview of the most significant GPR pitfalls, categorised into five groups (P1 to P5). For each category, the causes (column 2) and effects (i.e. the pitfalls themselves; column 3) are also reported.

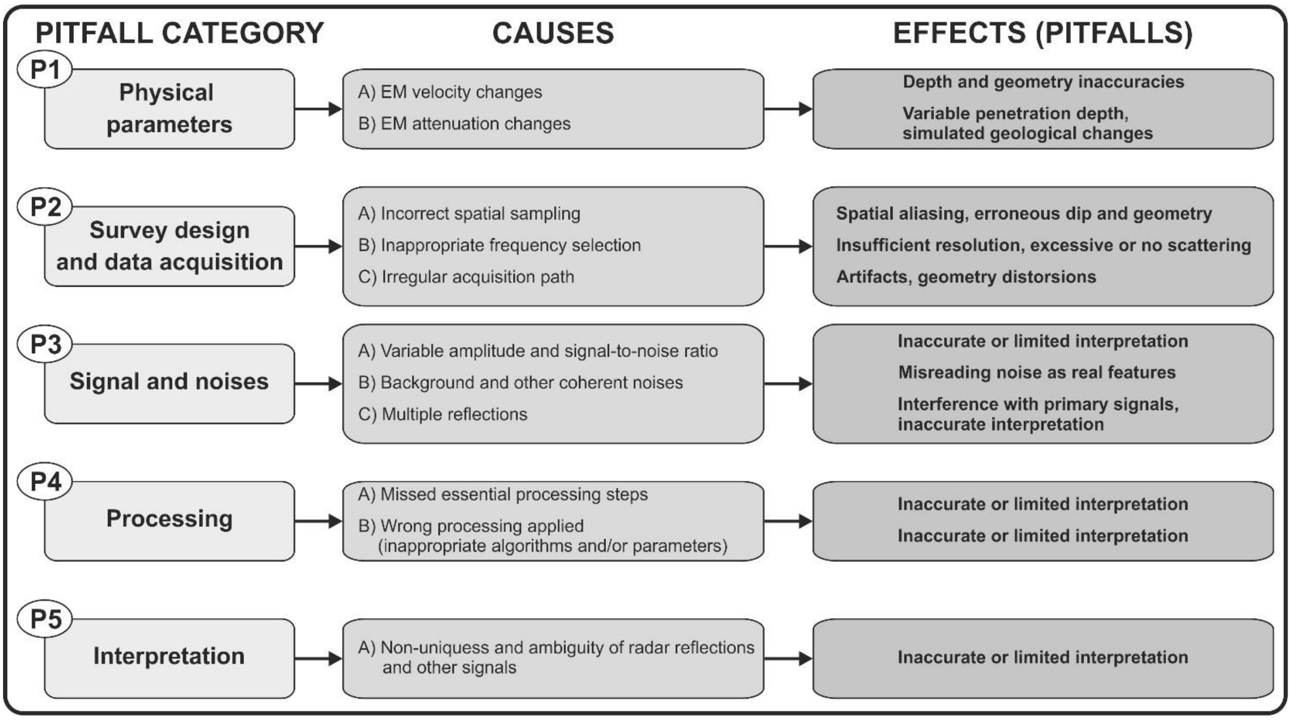

Fig. 1 – Scheme of the possible pitfalls in GPR, classified into five categories alongside their most relevant causes and typical effects.

2.1. P1 – Physical parameters

The main physical parameters affecting the GPR signals are the EM velocity and attenuation, which are in turn related to the electrical properties of the materials, with electrical conductivity and electrical permittivity being the most relevant. While variations in EM velocity, if not properly considered, can lead to erroneous depth and geometry reconstruction, spatially variable attenuation can limit the signal's penetration depth and result in completely inaccurate subsurface reconstruction. Figure 2 shows a paradigmatic example in which the abrupt lateral changes are due to surface materials with different attenuation (and thickness) above an almost homogeneous carbonate bedrock. The main fracture does not actually separate different materials, as might be supposed from the GPR profile. Since water (especially when brackish or salty water) is highly conductive, its presence can produce similar effects even when the host materials are similar, but the fluid content and salinity vary.

2.2. P2 – Survey design and data acquisition.

The survey design and the data acquisition phase are crucial steps in ensuring the quality of the collected data. Incorrect spatial sampling can produce aliased data, which in turn lead to erroneous shape interpretation (Forte et al., 2019). It is well established that the frequency of the transmitted signal is inversely proportional to the penetration depth and directly proportional to the resolution, but there are also some other peculiar effects related to the scattering. Scattering (diffraction) is in fact produced when a propagating EM wave interacts with objects that have different dielectric properties from their surroundings, and that are slightly smaller than or comparable to the wavelength of the incident wave (e.g., Tsang et al., 2000). In GPR data, scattering phenomena are quite common and are often used to detect local or elongated targets. If the signal frequency is not properly chosen, diffraction is not produced, making it difficult to detect the related targets. Other possible pitfalls include artefacts and geometric distortions due to irregular acquisition paths (Roncoroni et al., 2024).

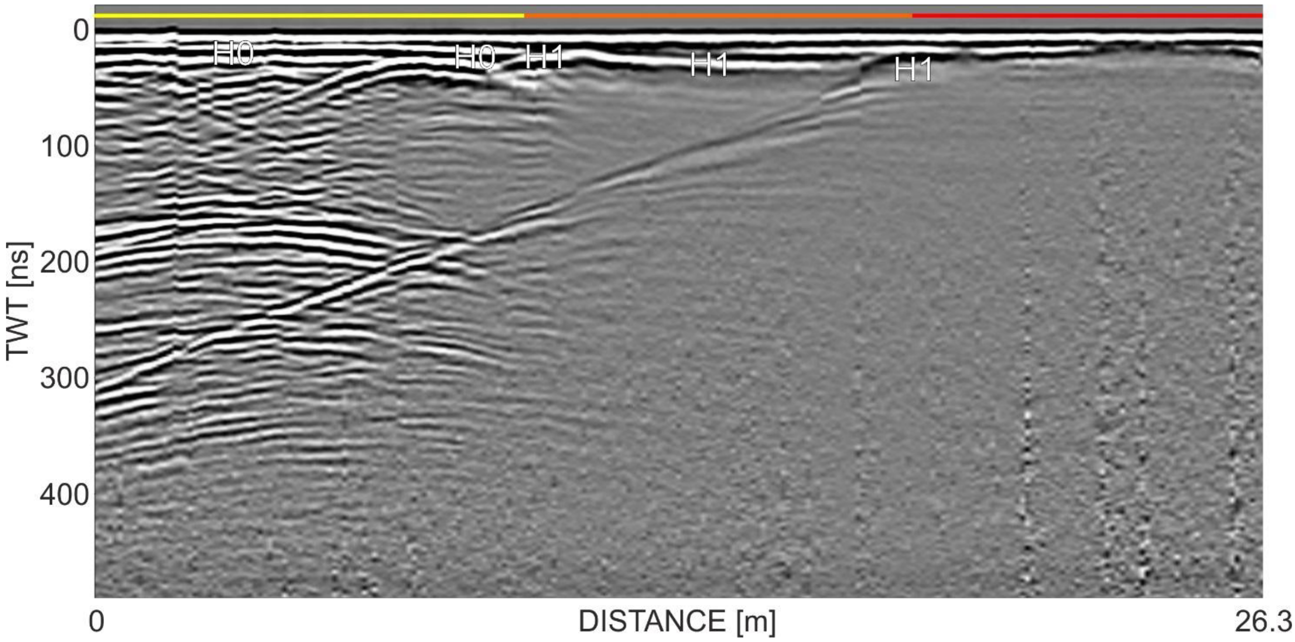

Fig. 2 – Example of lateral variations that are not real, due to surface materials with different attenuation and thickness. The layer marked by H0 has low overall attenuation (zone marked by the yellow segment), while the layer marked by H1 has higher attenuation, which limits the propagation of the GPR signal. Where the thickness is moderate (the zone marked by the orange segment), the signal can still penetrate to a certain depth. However, where the thickness is greater, the bottom cannot be detected in the section (the zone marked by the red segment) and the signal is almost completely attenuated.

2.3. P3 – Signal and noise

As with the other geophysical methods, low signal-to-noise ratios make it more difficult and less reliable to extract the information from the data. GPR signal is often affected by coherent noise arising from antennas interference and from interactions between the EM signal and highly conductive media, typically metals. The combination of these noises (usually referred to as background noise, clutter, ringing, and reverberations) interferes with the primary signals, and this interference is often difficult to completely remove, even with sophisticated filtering techniques. This, in turn, causes noise to be misread as real features, or to interfere with the signal. Similarly, multiple reflections, which occur only in specific situations in GPR records, can interfere with the primary signals, leading to an inaccurate interpretation (Nobes et al., 2005). In addition, signals travelling in the air can be reflected or diffracted above the surface and recorded by the receiving antenna, especially if it is unshielded. These events can be misinterpreted as coming from the subsurface.

2.4. P4 – Processing

The processing flow is an essential phase in any data analysis procedure. In GPR, especially when only single common offset and azimuth profiles are available, as is normal the case, the applied algorithms are limited and usually quite simple. While it is advisable for processing to be simple, real, systematic and consistent (Jol, 2009), there are cases in which omitting some processing steps or applying algorithms with incorrect parametrization can produce completely inaccurate results. This is particularly true of imaging algorithms when overly simplifying hypotheses (e.g., homogeneous materials) are considered or when knowledge of certain parameters (typically the EM velocity field) is inaccurate (Bradford et al., 2018). Furthermore, it is worth noting that applying different processing workflows to the same raw dataset can produce substantially different results.

2.5. P5 – Interpretation

As with the previous step, data interpretation has is inherently subjective, though subjectivity can be minimized, but never nullified. In fact, interpretation relies heavily on operator experience, which is difficult to quantify and measure objectively. In addition to human errors and oversimplifications due to limits of the interpreter, there are situations in which using only the reflection amplitude of 2-D profiles is insufficient and lead to interpretation errors. Figure 3 provides an example of this, showing that a GPR profile collected on a polythermal glacier is difficult to interpret without considering the glaciological context, its location, and accurate EM facies analysis. In fact, zones Z1 and Z2 may appear similar, but they are not. Z1 is an area characterized by the so called “warm ice”, while Z2 is a zone in which some debris is embedded within the ice. Discriminating between these alternative interpretations often requires numerical simulation (Ogier et al., 2023; Santin et al., 2023) and the calculation of specific signal attributes (Forte et al., 2025).

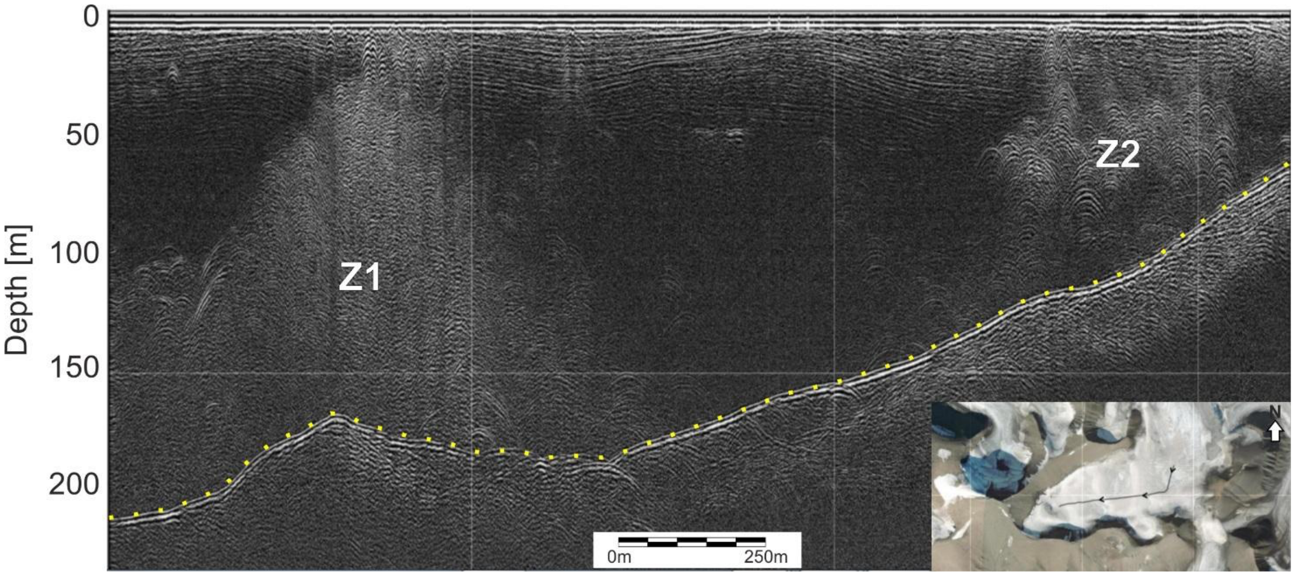

Fig. 3 – Example of a potential pitfall in the interpretation of GPR glaciological data. Zones Z1 and Z2 appear similar, however their EM signature is different: Z1 extends down to the yellow dotted horizon (glacier’s bottom) and is characterised by discontinuous and chaotic patterns, while Z2 lies above the horizon and is characterised by distinct diffraction hyperbolas. Z1 is related to warm ice facies, whereas Z2 is most likely due to internal debris within the ice body. Data from the “The Svalbard Radar Interpretation Experiment” (https://radar.mannerfelt.org), Slakbreen Glacier.

3. Conclusions

The analyses presented here demonstrate that reliable GPR imaging depends on the combined effects of subsurface physical properties, acquisition strategy, data quality, processing choices and interpretative constraints. Variations in EM velocity and attenuation can generate deceptive lateral changes that mask or mimic true structures, particularly where near-surface heterogeneities or conductive fluids influence signal propagation. Similarly, artefacts can be created by coherent noise, interference and even by improper processing that it is not physically consistent or appropriately parameterised. Data interpretation remains partially subjective, especially in complex environments. More reliable results are obtained by integrating contextual information, performing dedicated modelling and signal attribute calculation, and improving analysis, processing and inversion strategies. In any case, robust GPR prospecting requires a holistic approach that judiciously integrates acquisition, processing, and interpretation in order to avoid common pitfalls thus ensuring reliable subsurface reconstruction.

4. References

Annan, A.P.; 2001: GPR – Trends, history, and future developments, Proceedings of the EAGE 2001 Conference, Delft, the Netherlands, June 11-15, 2001.

Bradford, J.H., Privette, J., Wilkins, D., Ford, R.; 2018: Reverse-Time Migration from Rugged Topography to Image Ground-Penetrating Radar Data in Complex Environments, Engineering, 4(5), 661-666, 10.1016/j.eng.2018.09.004.

Forte, E., Pipan, M.; 2017: Review of multi offset GPR applications: data acquisition, processing and analysis, Signal Processing, 132C, 210-220, 10.1016/j.sigpro.2016.04.011.

Forte, E., Basso Bondini, M., Bortoletto, A., Dossi, M., Colucci, R.R.; 2019: Pros and cons in helicopter-borne GPR data acquisition on rugged mountainous areas: critical analysis and practical guidelines, Pure and Applied Geophysics, 176, 10, 4533-4554, 10.1007/s00024-019-02196-2.

Forte, E., Gutgesell, P., Securo, A., Marcer, M., Citterio, M., Machguth, H., Colucci, R.R.; 2025: Comparing GPR with ice thickness and thermal models: insights from two polythermal glaciers in West Greenland, Journal of Glaciology, 71, e97, 10.1017/jog.2025.10067.

Jol, HM.; 2009: Ground Penetrating Radar Theory and Applications, Elsevier Science, 10.1016/B978-0-444-53348-7.X0001-4, 524 pp.

Leckebusch, J.; 2011: Problems and Solutions with GPR Data Interpretation: Depolarization and Data Continuity, Archaeological Prospection, 18, 303-308, 10.1002/arp.422.

Martindale, A., Wadsworth, W.T.D., Simons, E., Whiting, B., Grier, C.; 2024: The challenges of signal interpretation of burials in ground-penetrating radar, Archaeological Prospection, 31(4), 337–351, 10.1002/arp.1920.

Nobes, D.C.; 2018: Interpretation pitfalls to avoid in void interpretation from ground-penetrating radar imaging, Interpretation, 6 (4): SL21–SL28, 10.1190/INT-2018-0049.1.

Nobes, D.C., Davis, E.F., Arcone, S.A.; 2005: “Mirror-image” multiples in ground-penetrating radar. Geophysics, 70 (1), K20–K22, 10.1190/1.1852781.

Nuzzo, L., Quarta, T., Galati, M.B., Fedi, M. and Garofalo, B.; 2008; Potential and pitfalls of GPR traveltime tomography for ancient buildings investigation: experiments on a small-scalem real and synthetic calcarenitic block, Near Surface Geophysics, 6, 207-219, 10.3997/1873-0604.2008016.

Ogier, C., van Manen, D.J., Maurer, H., et al.; 2023: Ground penetrating radar in temperate ice: englacial water inclusions as limiting factor for data interpretation, Journal of Glaciology, 69(278), 1874-1885, 10.1017/jog.2023.68.

Radzevicius, S.J., Guy, E.D., Daniels, J.J.; 2000: Pitfalls in GPR data interpretation: Differentiating stratigraphy and buried objects from periodic antenna and target effects, Geophysical Research Letters, 27, 20, 3393-339610.1029/2000GL008512.

Roncoroni, G., Forte, E., Santin, I., Černok, A., Rajšić, A., Frigeri, A., Pipan, M.; 2024: High frequency Lunar Penetrating Radar quality control, editing and data processing from Chang’E-4 lunar mission, Scientific Data, 11, 118, 10.1038/s41597-024-02963-4.

Santin, I., Roncoroni, G., Forte, E., Gutgesell, P., Pipan, M.; 2023: GPR modelling as a tool to quantify the debris content within ice, Near Surface Geophysics, 22, 2, 220-234, 10.1002/nsg.12274.

Xie, F., Wu, C.G.W., Lai, W.W.L., Sham, J.F.C.; 2018: Correction of multi-frequency GPR wave velocity with distorted hyperbolic reflections from GPR surveys of underground utilities, Tunnelling and Underground Space Technology, 76, 76-91, 10.1016/j.tust.2018.02.005.

Corresponding author: eforte@units.it

Integrating geophysical methods to characterize active paleo-landslides in Belgium

Agnese Innocenti[1], Anne-Sophie Mreyen[2], Léna Cauchie[3], David Caterina[2], Valmy Dorival[4], Yawar Hussain[5], Hans-Balder Havenith[4], Veronica Pazzi[1]

[1] Department of Earth Sciences, University of Florence, Italy
[2] Urban and Environmental Engineering, University of Liegi, Belgium
[3] ULiege Library, Faculty of Sciences, University of Liegi, Belgium
[4] Department of Geology, University of Liege, Belgium
[5] Department of Sustainable Earth Systems Sciences, The University of Texas at Dallas, USA

Introduction

Shallow landslides are a common instability process in hilly and mountainous areas. They are often triggered by intense rainfall, which increases pore-water pressure and reduces soil shear strength. Typically, they are translational phenomena (Hungr et al. 2014), and they develop along sub-horizontal interfaces with strong hydraulic and mechanical contrasts. Identifying basal shear surfaces is crucial for assessing landslide evolution, though detection remains challenging in soft sediments (Chandler 2020).

Geophysical methods are widely used in landslide investigations (Pazzi et al., 2019), including Electrical Resistivity Tomography (ERT), active seismic, and passive seismic techniques (Mreyen et al. 2021). Each method is sensitive to specific physical parameters and has limitations, such as seismic shadow zones or the need for strong impedance contrasts in passive seismic analyses (SESAME 2004). Therefore, integrated, multi-method approaches are needed to reduce interpretation ambiguity and improve model reliability. Within this framework, the Horizontal-to-Vertical Spectral Ratio (HVSR) technique complements active surveys (Pazzi et al. 2017). Active methods provide high-resolution but spatially limited data, while HVSR allows dense, non-invasive coverage. When converted into depth-domain sections assuming increasing shear-wave velocity with depth (Castellaro 2016), HVSR can delineate stratigraphic boundaries and potential slip surfaces, even in complex landslide settings.

The Pays de Herve region, near the northern Hockai Fault Zone (HFZ), is a dissected tableland with gentle slopes, generally <15° (Fig. 1a). This seismogenic structure hosts over 50 documented landslides (Mreyen et al. 2018). The geology consists of a folded Paleozoic basement (Upper Carboniferous Houiller shales) overlain by sub-horizontal Upper Cretaceous formations (Fig. 1a). Slope instability is controlled by an unfavourable lithology, where fine sands and silts of the Aachen Formation are overlain by clays and marls of the Vaals Formation. Aachen sands (~10 m thick) are prone to liquefaction and quicksand behaviour (Demoulin et al. 2003), while Vaals clays can reach ~25 m (Fig. 1b).

The Manaihan landslide (Fig. 1b), south of Battice on a gently east-facing slope (~4°), covers ~7 ha and is one of the best-monitored paleo-landslides in the region (Demoulin and Glade 2004). It affects Vaals clays (~12 m) over Aachen sands (~4 m). Damage since the 1990s is linked to anthropogenic loading and prolonged rainfall, with liquefaction of the Aachen sands likely promoting mixing with overlying clays (Demoulin et al. 2003).

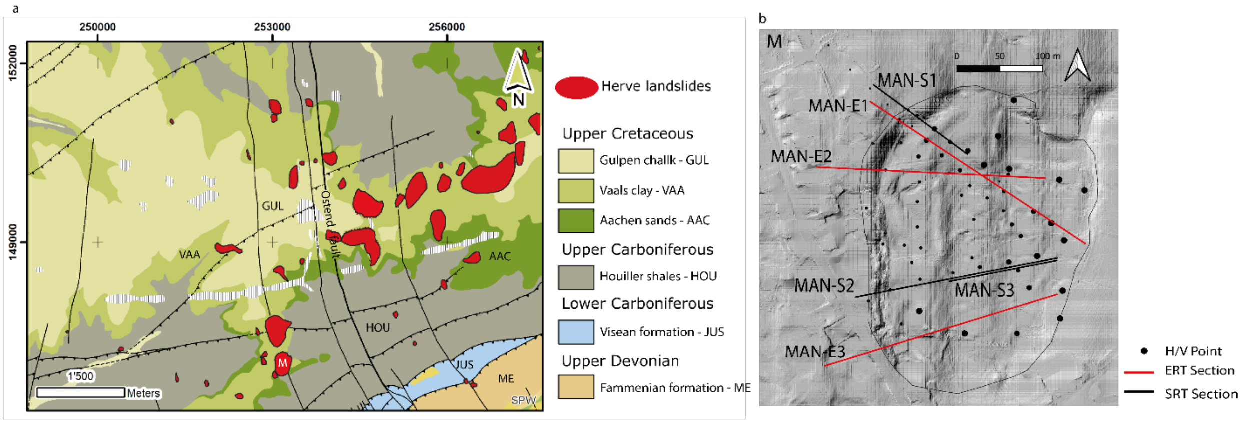

Fig. 1 – a) Geological context of the Pays de Herve with the Ostend fault and paleo-landslides mapped by Demoulin and Glade (2004); M, Manaihan landslide. b) hillshade analysis of Manaihan landslide with the corresponding geophysical measures (modified from Innocenti et al., 2025).

To investigate the subsurface structure of the Manaihan landslide and distinguish lithological contacts from landslide-related slip surfaces, an integrated geophysical approach was adopted, combining ERT, Seismic Refraction Tomography (SRT), Multi-channel Analysis of Surface Waves (MASW), and HVSR measurements.

Integrated geophysical dataset

Three ERT profiles (MAN-E1, MAN-E2, MAN-E3) (Fig. 1b) were acquired using an ABEM Terrameter LS system. Data were collected using Dipole–Dipole and Gradient electrode configurations and were jointly inverted using ErtLab™.

Similarly, three SRT profiles (MAN-S1, MAN-S2, MAN-S3) (Fig. 1b) were acquired using 48 vertical geophones and a 48-channel DAQLinkII seismograph. Hammer shots were used as the seismic source, and travel times were inverted using the reciprocal time method implemented in Seisimager 2D™.

MASW analysis was performed on the same seismic datasets to retrieve 1D shear-wave velocity (Vs) profiles. Dispersion curves were extracted using the f–k method in Geopsy and inverted with the dinver module, with the investigation depth limited to approximately one-third of the maximum analysed wavelength.

A total of 65 seismic noise measurements (Fig. 1b) were acquired using a Lennartz 3D/1 seismometer. Data processing followed SESAME (2004) guidelines and the ellipticity analysis was carried out by means of Wavepol by Burjánek et al. (2010, 2012). The fundamental resonance frequency (f_0) was interpreted as the response of soft sediments over a stiffer substratum. To extend the point-based HVSR information, data were converted into depth-domain representations and assembled into 2D H/V sections. This procedure assumes sub-horizontal layering and increasing

Vs with depth (Ibs-von Seht and Wohlenberg 1999; Delgado et al. 2000). Frequency-to-depth conversion used MASW-derived surface Vs values and a power-law relationship between f_0, Vs, and layer thickness (Castellaro 2016). Different Vs values were adopted for distinct landslide sectors to account for lateral variability.

The resulting 2D H/V sections, expressed in H/V amplitude, were aligned with the ERT profiles and used to identify the geometry and continuity of major seismic impedance contrasts, allowing extension of the interpretation to the entire landslide area.

Results

Results are limited to the MAN-E1 ERT profile, the MAN-S1 SRT profile, selected HVSR measurements (MAN-148, MAN-171, MAN-183, MAN-182), and the H/V section MAN-H/V1. Complete ERT, SRT and H/V datasets are presented in Innocenti et al. (2025).

The ERT profile MAN-E1 (Fig. 2a) shows a resistive near-surface unit (80–100 Ωm) in the upper slope, extending to ∼10 m depth. This unit overlies a laterally continuous conductive layer (10–40 Ωm), deepening upslope to ∼20 m and thinning downslope. The resistive unit is interpreted as Vaals clays locally mixed with Aachen sands, while the conductive layer corresponds to Houiller shales.

The SRT profile MAN-S1 (Fig. 2b) identifies two main seismic layers. The upper layer shows P-wave velocities of 500–800 m/s and reaches ∼20 m thickness near the scarp, thinning downslope to 2–5 m. The lower layer exhibits higher velocities (1500–2800 m/s), consistent with a consolidated substratum.

MASW results (Fig. 2g–i) confirm the SRT interpretation and highlight contrasts between stable areas and the landslide body. Outside the landslide, a ∼10 m thick layer shows Vs ≈ 200 m/s, whereas within the landslide it is thinner (~5 m) and softer (Vs ≈ 100 m/s). At greater depths, Vs increases to ∼400 m/s. Surface Vs decreases from west to east within the landslide, indicating spatial variability.

HVSR measurements at MAN-148, MAN-171, MAN-183, and MAN-182 (Fig. 2c–f) display clear resonance peaks between 2 and 5 Hz, with amplitudes close to 10. Measurements within the landslide show higher peak frequencies than those outside, indicating a shallower impedance contrast. Toward the toe, HVSR data suggest progressive shallowing of the main contrast, possibly related to localized deformation and topographic effects.

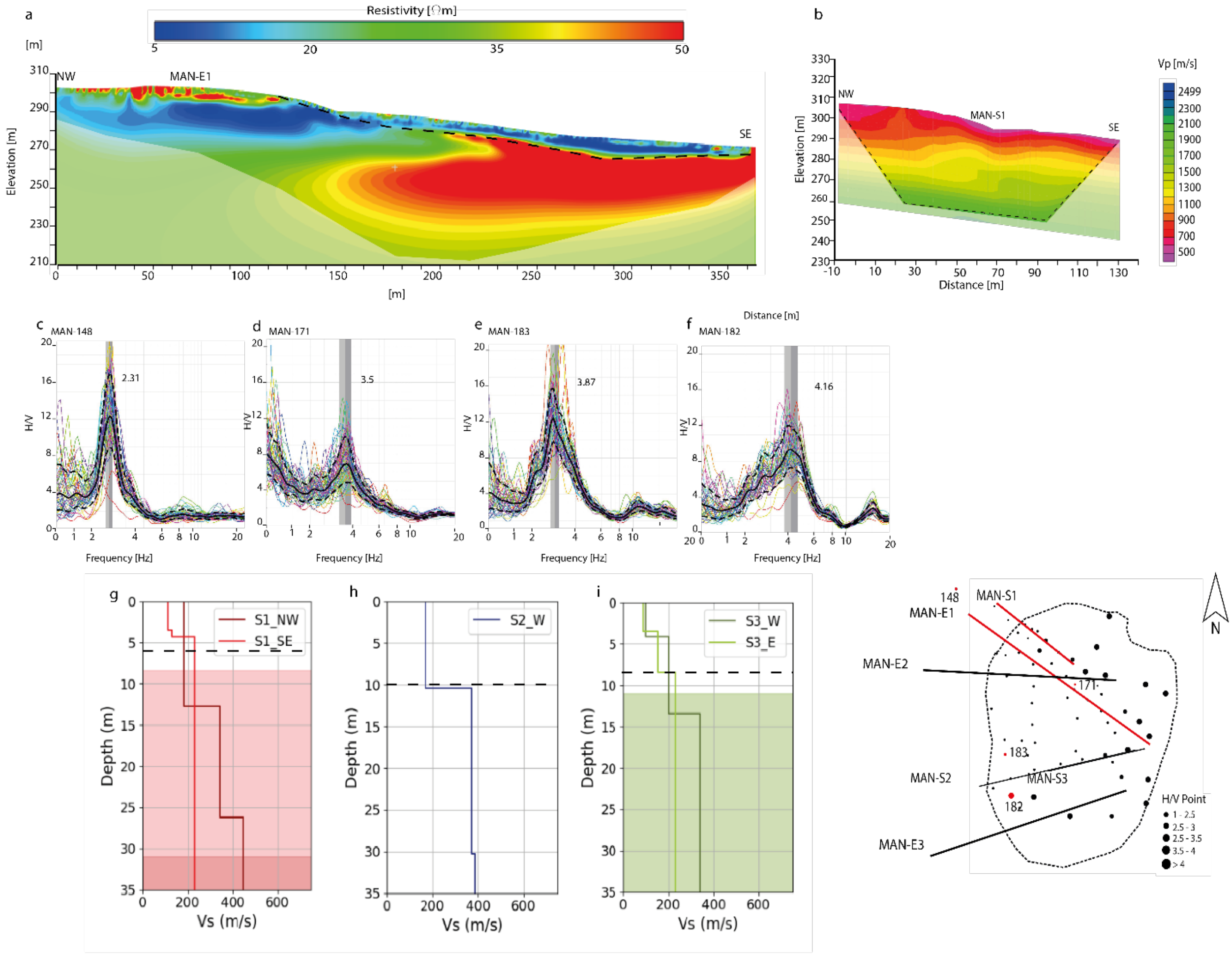

Fig. 2 – Geophysical investigations of the Manaihan landslide. The map shows the locations of ERTs and SRTs surveys as lines and the H/V acquisitions as dots; the sections and points analysed are highlighted in red. a) ERT of the MAN-E1 profile; whitened areas indicate zones characterized by higher model uncertainty. b) SRT of the MAN-S1 profile; black dashed lines together with the whitened areas delineate the outer limits of the ray paths used for the tomographic inversion. c), d), e), f) H/V measurements acquired at sites MAN-148, MAN-171, MAN-183, and MAN-182; the fundamental frequency peaks are highlighted by grey bars. h), i) one-dimensional Vs profiles derived from MASW analysis; each panel shows velocity profiles obtained from bidirectional shots. Coloured areas indicate subsurface depths affected by higher model uncertainty, while dashed lines mark the base of the landslide, defined by Vs ≤ 200 m/s (modified from Innocenti et al., 2025).

Discussions and Conclusions

The integrated interpretation of ERT, SRT, MASW, and HVSR data indicates that the basal shear surface of the Manaihan landslide is controlled by a major lithological interface. Electrical and seismic results consistently identify two laterally continuous units both inside and outside the landslide body. This interface, observed at depths ranging from approximately 10 to 30 m, is interpreted as the contact between the Upper Cretaceous Vaals–Aachen formations and the underlying Upper Carboniferous Houiller shales.

HVSR measurements, converted into depth-domain representations and constrained by MASW-derived shear-wave velocities, allow this interpretation to be extended beyond the limited coverage of active geophysical profiles. The reconstructed H/V section along MAN-H/V1 (Fig. 3a) highlights a continuous seismic impedance contrast at depths between ~15 and 40 m, spatially consistent with the lithological contact identified by ERT and SRT.

All geophysical datasets acquired at the Manaihan landslide were integrated into a 3D geomodel of the slope in its current state (Fig. 3b–f). Within this model, H/V measurements were incorporated as vertical logs using the same V_s values adopted for the H/V section reconstruction. The resulting impedance contrast, interpreted as the boundary between soft Cretaceous deposits and Upper Carboniferous shales, shows a strong agreement with both ERT and SRT data. The modelled H/V amplitudes provide constraints on the thickness and geometry of the subsurface units, allowing the definition of geological interfaces and volumes within the landslide body.

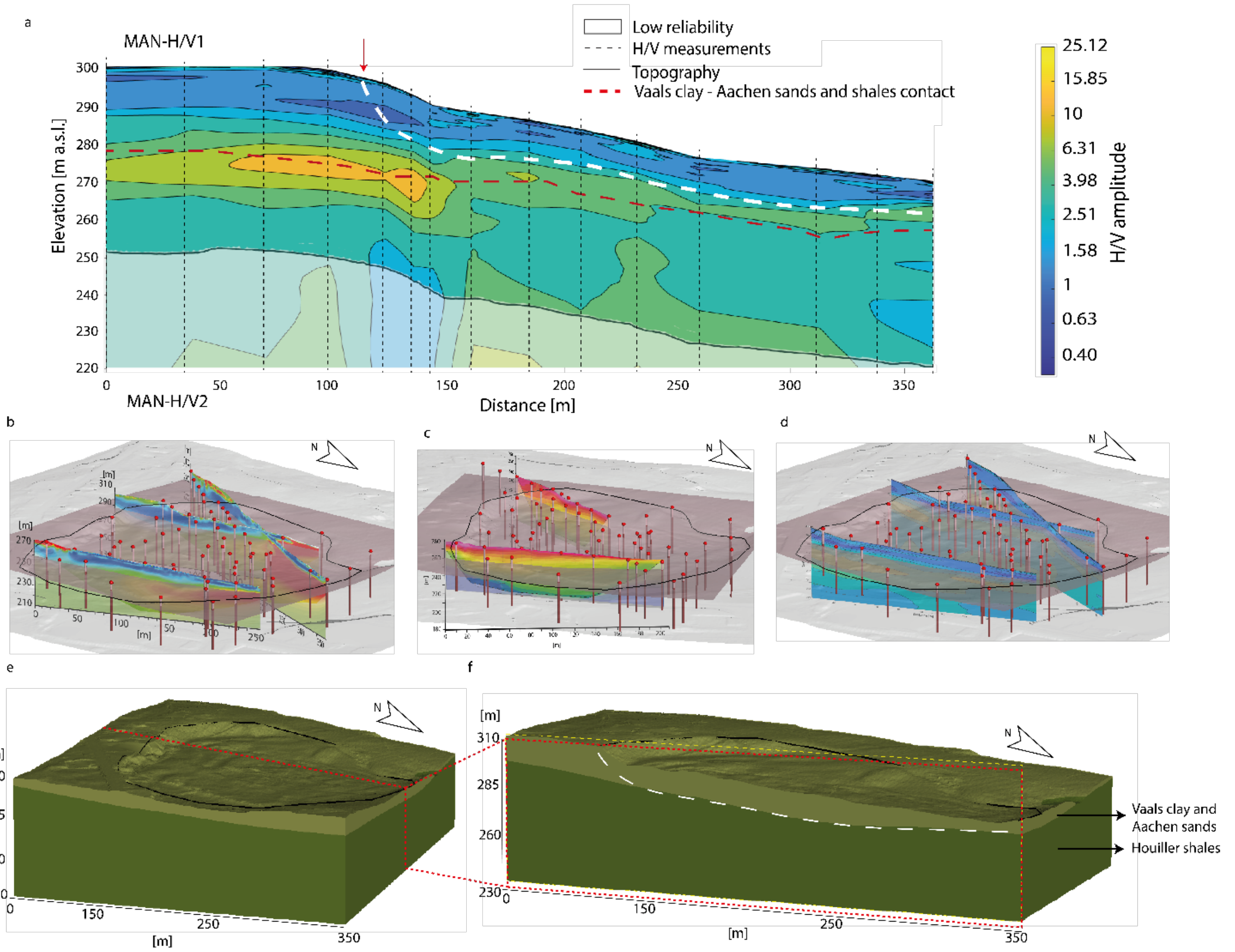

Fig. 3 – a) Contour plot of the H/V curves acquired following the alignments of the H/V measurements and converted from the H/V-frequency to the H/V-depth domain. The colour scale indicates the H/V amplitude. b), c) and d) geomodel construction of the Manaihan slope with modelling and insertion of 2D geophysical profiles, the integrated H/V logs and the contrast plane (pink) between the two materials identified by the acoustic impedance peaks. g) and h) the volumes, i.e., Vaals clay - Aachen sands mix and Houiller shales. The dashed red line represents the vertical cutting plane represented in f) by the dashed red rectangle. The dashed white line represents the possible sliding surface (modified from Innocenti et al., 2025).

This integrated approach, together with the ellipticity analysis, confirms that the Manaihan landslide is primarily controlled by a deep-seated geological interface rather than by internal deformation within the Cretaceous cover and demonstrates the effectiveness of combining active and passive geophysical methods for quasi-3D landslide characterization.

References

Burjánek, J., Gassner-Stamm, G., Poggi, V., Moore, J. R., & Fäh, D. (2010). Ambient vibration analysis of an unstable mountain slope. *Geophysical Journal International*, *180*(2), 820-828.

Burjánek, J., Moore, J. R., Yugsi Molina, F. X., & Fäh, D. (2012). Instrumental evidence of normal mode rock slope vibration. *Geophysical Journal International*, *188*(2), 559-569.

Castellaro S; 2016: The complementarity of H/V and dispersion curves. Geophys 81(6):323–338

Chandler RJ; 1986: Processes leading to landslides in clay slopes: a review. A. D. Abrahams (Ed.), Hillslope Processes, Allen and Unwin, Winchester, Massachusetts, 344–360

Delgado J, Lopez Casado C, Giner J, Estevez A, Cuenca A, Molina S; 2000: Microtremors as a geophysical exploration tool: applications and limitations. Pure Appl Geophys 157:1445–1462

Demoulin A, Pissart A, Schroeder C; 2003: On the origin of late quaternary palaeolandslides in the Liège (E-Belgium) area. Int J Earth Sci92(5):795–805

Demoulin A, Glade T; 2004: Recent landslide activity in Manaihan East Belgium. Landslides 1(4):305–310

Hungr O, Leroueil S, Picarelli L; 2014: The varnes classification of landslide types an update. Landslides 11(2):167–194

Ibs-von Seht M, Wohlenberg J; 1999: Microtremor measurements used to map thickness of soft sediments. Bull Seismol Soc Am 89(1):250–259

Mreyen AS, Demoulin A, Havenith HB; 2018: Seismotectonic activity in east Belgium: relevance of a major scarp and two associated landslides in the region of Malmedy. Geol Belg 21(3–4):101–110

Pazzi V, Tanteri L, Bicocchi G, D'Ambrosio M, Caselli A, Fanti R; 2017: H/V measurements as an effective tool for the reliable detection of landslide slip surfaces: case studies of Castagnola (La Spezia, Italy) and Roccalbegna (Grosseto Italy). Phys Chem Earth Parts A/B/C 98:136–153

Pazzi V, Morelli S, Fanti R; 2019: A review of the advantages and limitations of geophysical investigations in landslide studies. Int J Geophys.

Site EffectS Assessment using AMbient Excitations (SESAME); 2004: Guidelines for the implementation of the H/V spectral ratio technique on ambient vibrations measurements, processing and interpretation, SESAME European Research Project , WP12 - Deliverable D23.12

Corresponding author: Agnese Innocenti agnese.innocenti@unifi.it

Integrating Applied Geophysics for High-Resolution Soil Moisture Mapping and Hydrogeological Risk Assessment in Urban Environments

Luigi Martino[1,2], Giuseppe Calamita[1], Gregory De Martino[1], Erwan Gueguen[1], Teodosio Lacava[2], Ibraim G. Lando[2], Viola Cioffi[3], Sebastian Uhlemann[4], Filomena Canora[2] and Angela Perrone[1]

[1] *CNR-IMAA Institute of Methodologies for Environmental Analysis, Potenza, Italy,*
[2] *University of Basilicata, Department of Science, Potenza, Italy,*
[3] *University of Padova, Department of Geosciences, Padova, Italy*
[4] *University of Bremen, Bremen, Germany*

This research investigates the effectiveness of geoelectrical monitoring in quantifying spatio-temporal soil moisture dynamics within the unsaturated zone, focusing on a peri-urban slow-moving landslide in the Southern Apennines of Basilicata, Italy (Fig. 1). In an era where extreme climatic events, spanning from prolonged droughts to intense rainfall, exacerbate cascading hydrological challenges, understanding subsurface moisture behavior is critical for managing a wide range of hydrological challenges (e.g. agricultural water scarcity, urban water management, slope instability and landslide risk). **Hydrogeophysics**, enhanced by integrated **environmental monitoring**, plays a critical role in this task (Binley et al., 2015; Parsekian et al., 2015).

The predictive capacity of modern hydrology and watershed modeling is fundamentally constrained by the uncertainty surrounding the structure and distribution of subsurface materials. This complexity arises not only from the magnitude of heterogeneity within single properties but also from its dynamic nature and the way its manifestation shifts across scales, a phenomenon long recognized as **hydrological scaling** (Neuman & Di Federico, 2003).

Grounded in this principle, we implemented a multi-scale characterization of the landslide body, employing a "**zoom-in**" strategy that transitions from the watershed scale down to the specific unsaturated zone of interest. This preliminary phase was designed not to answer the primary research question directly, but to engineer the monitoring system with precision. At the watershed scale, microtremor (HVSR) measurements defined the contact with the seismic bedrock, while landslide-scale geomorphological surveys and 2-meter resolution Digital Elevation Models (DEM) delineated active sectors. Integrating these data with coarse Electrical Resistivity Tomography (ERT) validated the landslide's geometry and boundaries. These insights directly informed the technical design of the station, dictating the placement of tensiometers at critical depths and the selection of a high-resolution 1.2-meter electrode spacing for time-lapse monitoring, currently in its pilot testing stage. This ensured the system was optimized to capture the specific hydraulic dynamics of the site's unsaturated zone. The methodology further integrates this high-resolution TL-ERT with a suite of hydrological sensors, including piezometers, soil moisture probes, and tensiometers (Fig. 2). This field setup is complemented by a customized laboratory environment, building upon the framework developed by Boyd et al. (2024), designed to replicate coupled geoelectrical and hydrogeological measurements under controlled conditions (Fig. 3). The laboratory phase involves drying cycle experiments on saturated samples from varying depths, utilizing a complex 289-quadrupole configuration. Initial results indicate that resistivity measurements remain stable until reaching tensiometric limits (i.e. cavitation and air entry point) though vertical array data currently exhibits noisier distribution requiring advanced filtering. By employing machine learning to merge these multi-scale observations, this research ultimately seeks to derive a robust field-scale petrophysical model capable of transforming geoelectrical data into reliable insights for hydrogeological risk management.

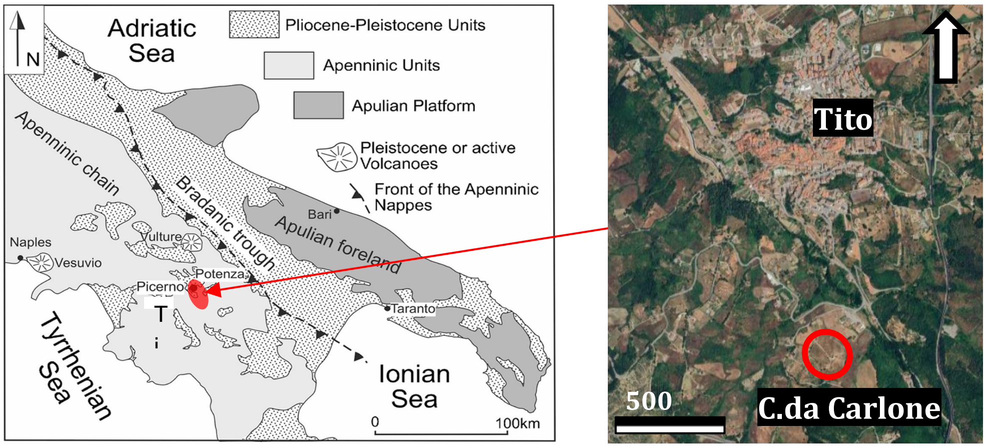

Fig. 1 – The study site is located in a peri-urban area near Tito municipality (Pz) in t southern Appennine (Italy)

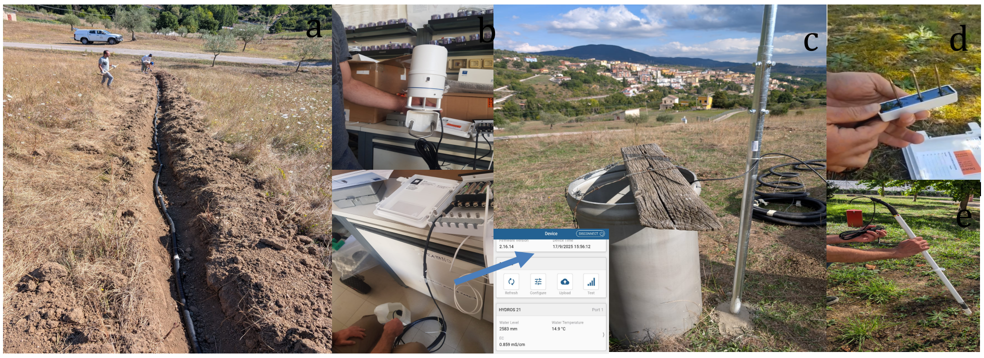

Fig. 2 – The monitoring station made of TL ERT system (a), environmental (b) and hydraulic sensors (piezometer - c, soil moisture sensor - d, and tensiometer - e)

Fig. 3 – The Lab setup, composed by GeoTom resistivimeter and a Hyprop 2 (Meter group) using a customized sample holder.

Acknowledgments

Our research is part of the WP7-7.4 task within the ITINERIS project (Italian Integrated Environmental Research Infrastructures System, PNRR M4C2 Inv.3.1 IR), funded under the EU's Next Generation program. The authors would like to acknowledge the ITINERIS project for the provision of the equipment/instrumentation used in this study.

References

Binley, A., Hubbard, S. S., Huisman, J. A., Revil, A., Robinson, D. A., Singha, K., & Slater, L. D. 2015: The emergence of hydrogeophysics for improved understanding of subsurface processes over multiple scales. Water resources research.

Boyd J. P., Binley A., Wilkinson P., Holmes J., Bruce E., Chambers J. 2024a: Practical considerations for using petrophysics and geoelectrical methods on clay rich landslides. Engineering Geology.

Neuman S. P., Di Federico V. 2003. Multifaceted nature of hydrogeologic scaling and its interpretation. Reviews of Geophysics, 41.

Parsekian A. D., Singha K., Minsley B. J., Holbrook W. S., Slater L. 2015: Multiscale geophysical imaging of the critical zone. Reviews of Geophysics.

Corresponding author: luigimartino@cnr.it

Exploring the Integrated Imaging of GPR and Magnetic Data through an Arithmetic approach

Francesco Mercogliano[1,2], Andrea Barone[2], Giuseppe Esposito[2], Raffaele Castaldo[2], Pietro Tizzani[2], Ilaria Catapano[2]

[1] *Dipartimento di Ingegneria (DI), Università degli Studi di Napoli "Parthenope", Italy*
[2] *Istituto per il Rilevamento Elettromagnetico dell'Ambiente, Consiglio Nazionale delle Ricerche (IREA CNR), Italy*

The concept of data integration is widely recognised in geophysics and geophysical exploration. Although it is generally understood that an integrated survey should involve the use of multiple complementary techniques to gather as much information as possible on the subsurface, the definition of the optimal approach for the effective integration of the resulting dataset is still not univocal. Broadly, data integration aims to provide more information that can be derived from each of the single dataset alone, thereby enhancing information content and reducing interpretative ambiguities. Despite being a widespread faced research topic, data integration is not yet fully explored, and remains an open issue, which strongly depends on the available data and, consequently, on the considered geophysical methods and sensing technologies.

Among the different geophysical methods, this study deals with Ground Penetrating Radar (GPR) and magnetic methods. GPR is an active geophysical method that is sensitive to dielectric permittivity contrasts, whereas magnetic method is passive and sensitive to magnetic susceptibility contrasts. Despite being fundamentally different, these two methods are commonly used together in several applications (e.g., geo-environmental, archeologic, geotechnical and engineering). This is mainly due to their cost-effectiveness, versatility, data collection capabilities and non-invasiveness. Moreover, both methods enable the detection and localization of buried targets through the analysis of electromagnetic and magnetic anomalies occurring within the investigated space.

GPR data are typically represented as radargrams, which provide information on the position and depth of subsurface targets based on the travel time of the electromagnetic signal. Magnetic method, in turn, yields spatial maps of the magnetic field, where anomalies correspond to the presence in the subsurface of magnetized bodies. Once properly processed and filtered, the results obtained from both GPR and magnetic methods are commonly analyzed jointly to enhance the interpretation and understanding of the subsurface. Moreover, beyond standard processing and filtering procedures, these methods benefit from advanced imaging approaches, such as microwave tomography (MWT) for GPR and Depth from EXtreme Points (DEXP) for magnetometry, which allow obtaining further information for subsurface interpretation.

The primary aim of this study is to develop an approach for the quantitative integration of GPR and magnetic data exploiting the results obtained from their respective imaging techniques. In principle, such integration would entail the development of a new joint imaging methodology for both GPR and magnetic data simultaneously. However, it must be emphasized that the two methods are based on entirely different and unrelated physical properties. Accordingly, the proposed approach is based on the arithmetic integration of the results obtained by MWT and DEXP yielding a single composite image, which enhances the interpretability of survey results and the characterization of anomalous targets in terms of morphology, position, and depth.

The proposed approach was validated through simulated magnetic and GPR datasets under different scenarios. Data were processed by means of DEXP and MWT, respectively, and then the quantitative arithmetic integration was performed. These preliminary results show how the integrated images can outperform the results from individual methods, overcoming their limitations and enabling more accurate and detailed subsurface models. This represents a promising step towards real-world applications, with further developments aimed at refining the approach for broader geophysical purposes.

Acknowledgments

This research has been founded by EU - Next Generation EU Mission 4, Component 2 - CUP B53C22002150006 - Project IR0000032 – ITINERIS - Italian Integrated Environmental Research Infrastructures System.

Corresponding author: francesco.mercogliano001@studenti.uniparthenope.it

Full-3d ERT sequences for archaeological prospection: comparison of different strategies

A. Merico[1], **A. Vergnano**[1], **C. Comina**[1]

[1] *Università degli Studi di Torino, Italy*

Introduction

Typically, ERT surveys are designed to generate 2D resistivity profiles that reveal the internal structure of the subsurface along a predefined transect. These profiles can be interpolated across multiple survey lines to create quasi-3D visualizations such as depth slices or volumetric models, which aid in the interpretation of subsurface features (e.g., Karaoulis et al., 2024; Louvaris et al., 2025). This quasi-3D approach has been widely adopted due to its practicality in fieldwork and data processing, especially in contexts where time, cost, or site conditions constrain the use of more elaborate acquisition strategies.

However, a growing number of studies have demonstrated the added advantages of adopting a full-3D data acquisition framework, wherein measurements are planned and executed to optimize spatial coverage in three dimensions (Casas et al., 2018). These cases often produce more robust models, capable of resolving structures that might be misrepresented or entirely missed in quasi-3D surveys (Papadopoulos et al., 2006). Methodological literature on ERT in archaeological settings tends to focus heavily on data interpretation and visualization, while less attention is paid to the practical and technical aspects of survey design: although numerous studies showcase the effects of array choice and dipole spacing (e.g. Casas et al., 2018; Karaoulis et al., 2025; Comina et al., 2025; Louvaris et al., 2025; Simyrdanis et al., 2021; Uhlemann et al., 2018; Vergnano et al., 2025), measurement sequencing in 3D arrays for the acquisition of full 3D data is still under-investigated.

This study aims to critically examine the role of measurement sequences in full-3D ERT surveys seeking to contribute to a more systematic understanding of how measurement design influences data quality, model reliability, and ultimately archaeological interpretation. To this aim, several acquisition sequences were tested both on synthetic data and on data acquired at a real test site in the archaeological area of Tyndaris (Messina, Italy).

Methodology

One of the sequences tested in this work was specifically developed through a custom open-source quadrupole sequence generator, optimized for achieving high sensitivity to archaeological remains within the first meters of subsoil. This sequence had been previously employed in a geophysical survey at the archaeological site of Augusta Bagiennorum (Cuneo, Italy), where it successfully revealed the layout of buried wall structures with a high degree of correspondence to features observed in multichannel Ground Penetrating Radar (GPR) time-slices (Vergnano A. et al., 2025).

This work aims to further verify the robustness of the developed survey design of this sequence by comparing it to several other acquisition sequences that are commonly available through commercial software (i.e. ERTLab by Geostudi Astier and Electre Pro by IRIS instruments).

In addition to the number of measurements they contain, a key factor distinguishing each sequence is their underlying acquisition strategy – that is, the logic by which electrode combinations are selected and ordered, as well as the optimisation of each sequence to the instrumentation employed on field. Each strategy follows a different spatial logic designed to emphasize specific geometries or coverage patterns in the subsurface. To aid visualise how sequences activate current and potential dipoles over time, a conceptual representation on a 12x12 squared electrode grid is presented in Figure 1.

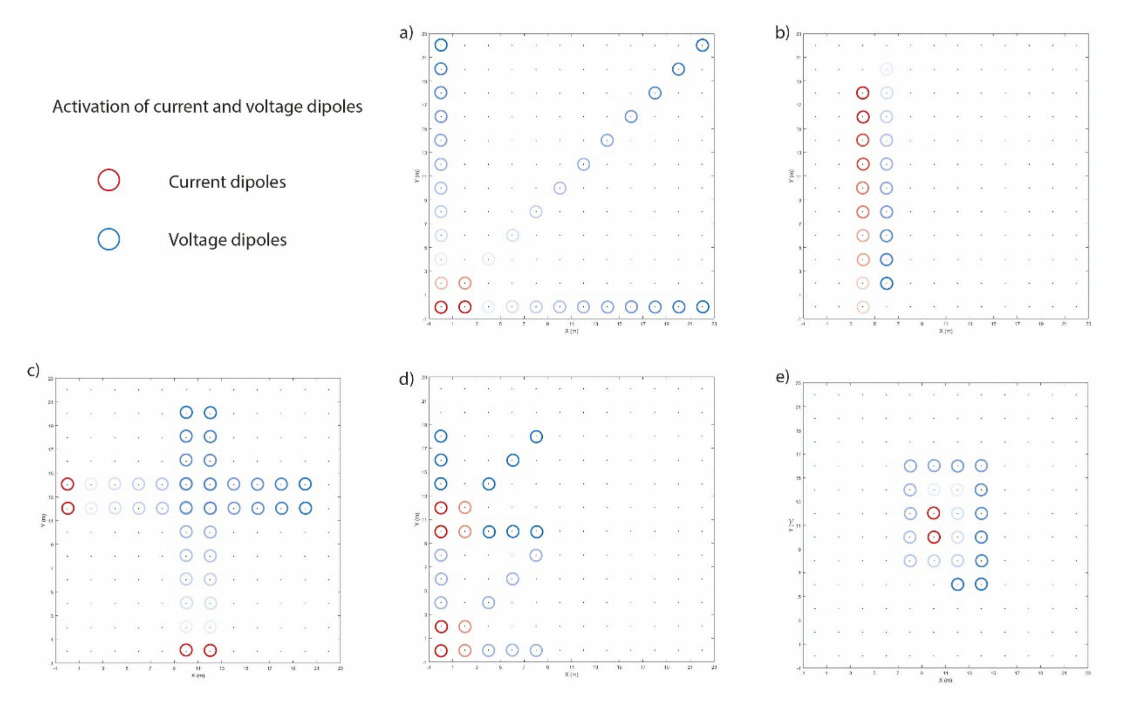

Fig. 1 The activation of current and voltage electrodes on a 12x12 grid with 2 m spacing. In order, the sequences illustrated are: a) CROSS, b) DIFFCA, c) EQU, d) LINE, e) VER.

To test the potential results of all sequences both synthetic tests and field tests data were adopted. For both datasets inversions were performed using consistent parameters across all datasets to ensure a uniform and unbiased basis for comparison. The inversion process was carried out using ResiPy, which implements an "Occam-style" inversion approach (Blanchy et al., 2020). This method minimises a regularised objective function that combines a data misfit term – based on a least squares formulation – with a model smoothness constraint.

Synthetic data

For synthetic tests a 20x20 m model with the presence of a target anomaly was created in Gmsh, a complementary mesh manager for ResiPy, to fit a 144 electrodes squared grid with 2 m spacings. The target is a four-arms crooked cross, to simulate wall-like anomalies having different orientations (0, π/4, 5π/6 and 5π/4), surrounded by a torus (Figure 2a). The arms of the cross are 5.8 m long, while the torus has a radius of 8 m and a thickness of 0.4 m. Both elements are found 1 m below the surface and extend vertically for 0.5 m; depth slices of the inverted resistivities with each sequence from Figure 2 are therefore extracted at 1.25 m depth, which is the barycentre of the anomalies.

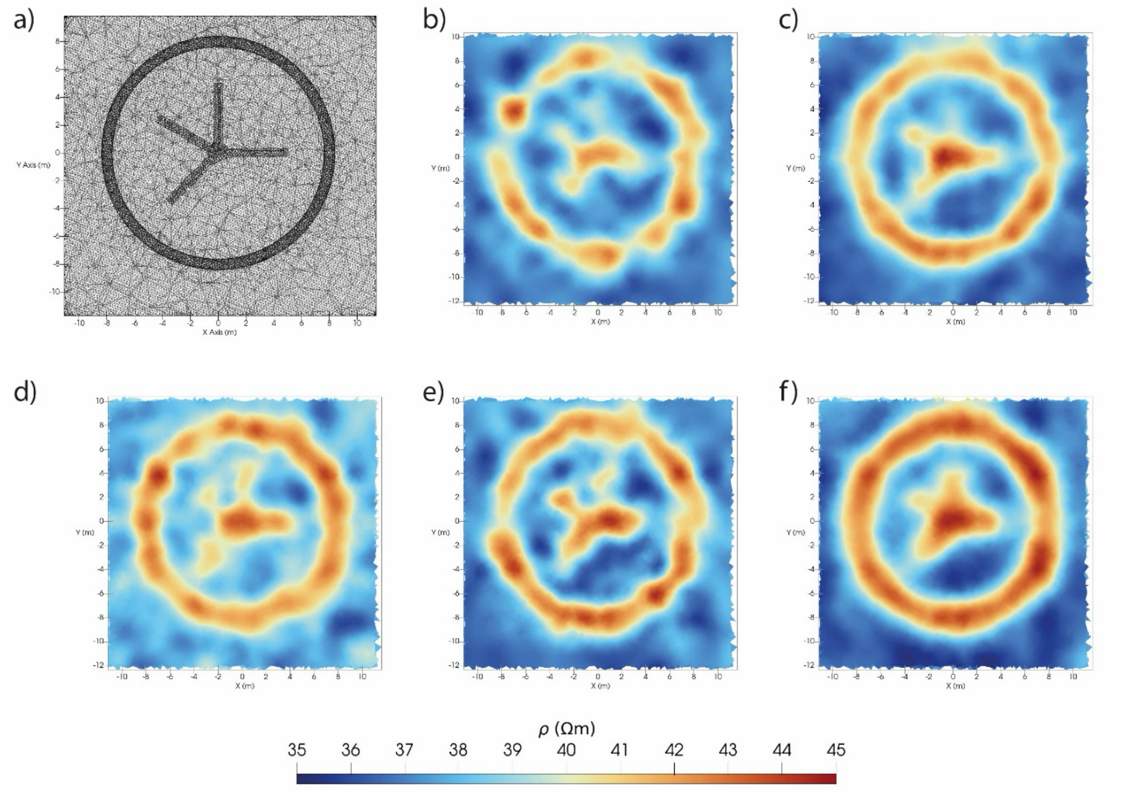

Fig. 2 Resistivity depth slice (-1.25 m from mesh surface) of all sequences: a) Reference mesh, b) CROSS, c) DIFFCA, d) EQU, e) LINE, f) VER.

Field survey

Field data were collected as part of an investigation campaign in the archaeological park of Tyndaris. Several areas were surveyed through 3D ERT, including one previously investigated by means of multichannel GPR (Comina et al., 2025). This area (Figure 3a) was the object of the methodological approach carried out in this study, in which the same acquisition was run over multiple sequences.

Similarly to numerical modelling, the results of the field survey are displayed as horizontal resistivity depth maps. A representative set of these results is displayed in Figure 3, which show the resistivity depth maps from all sequences, which were obtained by slicing the resistivity volume with a plane parallel to the topographic surface at -1.25 m from ground level.

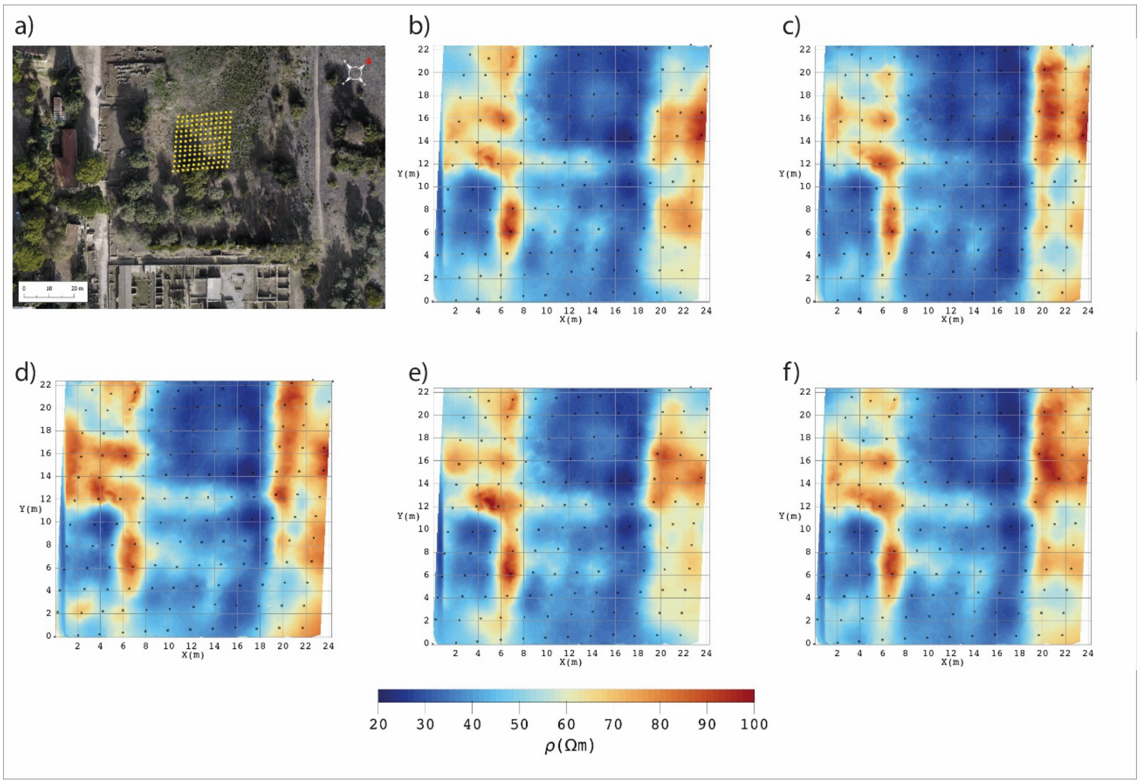

Fig. 3 Resistivity depth slice (-1.25 m from mesh surface) of all sequences: a) Electrode grid, b) CROSS, c) DIFFCA, d) EQU, e) LINE, f) VER.

Results

To evaluate the performance of each sequence in both numerical modelling and field data inversion, we performed quantitative image analysis on the entire results dataset, including:

- For numerical modelling:
  - Image difference between a control image (the modelled target) and the depth slices from each inversion.
  - Electric resistivity masking through anomaly thresholding.
  - Comparison of digital number (DN) intensity over a line and a ring profile.
- For field data, since a control dataset was missing:
  - Electric resistivity masking through anomaly thresholding.
  - Analysis of inversion performance through statistical L-curve comparisons: for each sequence, 10 inversions with different initial parameters (initial resistivity of the model, ranging from 10 to 5000 Ωm) were launched, to evaluate their robustness.

The analyses carried out on the results allowed us to distinguish clear differences brought by sequence choice, both from an operational point of view (such as acquisition time on field) and results produced.

Synthetic data

The depth slices obtained from the resistivity volume after inversion (Figure 2) of all sequences display the presence of the modelled anomaly with its shape being outlined with varying degrees of sharpness. Table 1 provides a qualitative synthesis of the performance of the tested acquisition sequences. The evaluation is based on three main interpretative criteria: a) the number of clearly recognisable arms of the cross-shaped target, b) the degree of continuity of these arms – specifically accounting for the so-called tip effect, whereby the terminal portion of an arm appears as a localized bulge rather than as a continuous extension of the anomaly body – and c) the continuity of the torus anomaly surrounding the cross.

Tab. 1 A qualitative summary of the performance of each sequence tested.

Sequence	Cross	Ring
CROSS	3 arms, tip effect	Discontinuous
DIFFCA	3 arms, tip effect	Continuous
EQU	4 arms, tip effect	Continuous
LINE	4 arms, tip effect	Continuous
VER	4 arms, no tip effect	Continuous

Image difference and threshold masking confirm the insights drawn from depth slices, while at the same time introducing a more robust way to identify the areas in which the candidate sequence came closer to representing the target. DN maps along the line and ring profiles served as a tool to evaluate image "fidelity" on a controlled subset of the depth maps, allowing to focus on specific areas and verify the closeness of the candidate image to the reference through profile difference RMSE and Normalised Cross-Correlation.

Field survey

The analysis of depth slices across all sequences (Figure 3) illustrates the arrangement of buried structures within the subsurface. The observed features exhibit continuity, and the high signal-to-noise ratio enables clear identification of shapes. Resistive anomalies are detected on both the left (SE) and right (NW) sides of the survey area. In contrast, the central region is predominantly characterised by a substantial conductive infill, which is occasionally interrupted by faint, quasi-horizontal linear features trending from southeast to northwest.

It is important to note that the ability to resolve these targets with continuity varied among different sequences – as evidenced through threshold masking – and that L-curve based analysis of inversion performance evidenced heterogeneity in residual/roughness trade-off and standard deviation in the set of inversions. Based off these considerations, the evaluations of on-field results closely follow those derived from numerical modelling, in which the best results were obtained from sequence VER, while the remaining approaches – although providing information about the subsurface – did not allow an equally clear or unambiguous interpretation of the investigated features.

Conclusions

This study highlights the impact of measurement sequence design on the quality of full-3D ERT data, both in synthetic models and real-world archaeological applications. The results indicate that sequence choice significantly influences the resolution and continuity of subsurface features, with some sequences providing more distinct and continuous representations of target anomalies. Notably, sequences that minimize target boundary effects (tip effect) and optimize the continuity of structures, such as the VER sequence, were more effective in accurately representing complex archaeological targets. Field data further corroborated the synthetic findings, revealing differences in inversion robustness and target resolution across sequences. These results underscore the importance of tailored acquisition strategies in archaeological prospection, with implications for both survey design and data interpretation.

Acknowledgements

We thank the Archaeological Park of Tindari for allowing us to perform our survey on their premises and Professor Rosina Leone (Università degli Studi di Torino, Department of Archaeology and Ancient History) for her continuous support during the investigation. We are indebted to the Applied Geophysics Laboratory of the Department of Environment, Land and Infrastructure Engineering at Polytechnic of Turin for the availability of ERT instrumentation.

References

Blanchy, G., Saneiyan, S., Boyd, J., McLachlan, P., & Binley, A. (2020). ResIPy, an intuitive open source software for complex geoelectrical inversion/modeling. *Computers and Geosciences*, *137*. https://doi.org/10.1016/j.cageo.2020.104423

Casas, A., Cosentino, P. L., Fiandaca, G., Himi, M., Macias, J. M., Martorana, R., Muñoz, A., Rivero, L., Sala, R., & Teixell, I. (2018). Non-invasive Geophysical Surveys in Search of the Roman Temple of Augustus Under the Cathedral of Tarragona (Catalonia, Spain): A Case Study. In *Surveys in Geophysics* (Vol. 39, Issue 6, pp. 1107–1124). Springer Netherlands. https://doi.org/10.1007/s10712-018-9470-6

Karaoulis, M., Tsokas, G. N., Tsourlos, P., Bogiatzis, P., & Vargemezis, G. (2025). 3D Electrical Resistivity Tomography Using a Radial Array and Detailed Topography for Tumuli Prospection. *Archaeological Prospection*, *32*(1), 197–208. https://doi.org/10.1002/arp.1966

Comina C., Leone, R., Palmisano, I., & Vergnano, A. (2025). Off-line stacking for multichannel GPR processing in clay-rich 2 archaeological sites: the case study of Tindari (Sicily). Cesare Comina. *Appl. Sci*, *2025*. https://doi.org/10.3390/xxxxx

Louvaris, P. K., Tsourlos, P. I., Vargemezis, G. N., & Tsokas, G. N. (2025). Three-Dimensional Electrical Resistivity Tomography Schemes Optimized for Imaging Wall Foundations. *Archaeological Prospection*, *32*(3), 726–739. https://doi.org/10.1002/arp.1991

Simyrdanis, K., Papadopoulos, N., & Oikonomou, D. (2021). Computation of optimized electrode arrays for 3-D electrical resistivity tomography surveys. *Applied Sciences (Switzerland)*, *11*(14). https://doi.org/10.3390/app11146394

Uhlemann, S., Wilkinson, P. B., Maurer, H., Wagner, F. M., Johnson, T. C., & Chambers, J. E. (2018). Optimized survey design for electrical resistivity tomography: Combined optimization of measurement configuration and electrode placement. *Geophysical Journal International*, *214*(1), 108–121. https://doi.org/10.1093/gji/ggy128

Vergnano, A., Franco, D., Merico, A., Pace, F., Uggè, S., & Comina, C. (2025). Survey and Sequence Strategies for Full-3D Electrical Resistivity Tomography in Archaeological Sites: A Case Study on a Domus of the Roman Town of Augusta Bagiennorum (NW Italy). *Archaeological Prospection*. https://doi.org/10.1002/arp.70013

Corresponding author: antonio.merico@unito.it

Assessment of ice-related ambiguities in petrophysical-driven joint inversion

A. L. Miño [1], M. Pipan[1]

[1] *University of Trieste, Italy*

Quantitative estimation of liquid water, ice, air, and rock-matrix fractions is essential for a process-based understanding of periglacial environments and their evolution under climate forcing. Seismic refraction and electrical resistivity tomography provide complementary sensitivities to frozen-ground properties (Hauck et al., 2011; Mollaret et al., 2020); however, the interpretation of observed anomalies remains ambiguous, particularly with respect to the physical role of ice. Phase-based petrophysical joint inversion approaches address this ambiguity by coupling seismic and electrical data through constitutive relationships, enabling direct estimation of volumetric phase fractions while enforcing physical bounds.

In this study, we perform a systematic comparison of three inversion strategies to investigate how increasing levels of petrophysical, and rock-physics complexity affect the interpretation of periglacial subsurface structures. First, we consider an independent petrophysical interpretation in which seismic and electrical responses are analyzed separately using effective-medium theory (EMT). Second, we apply the classical four-phase petrophysical joint inversion after Hauck et al. (2011), where seismic slowness is modelled using a time-average equation and electrical resistivity is described by Archie's law (Archie, 1942), treating ice as a volumetric phase that affects phase proportions but does not contribute to elastic stiffness (Wagner et al., 2019). Third, we evaluate a proposed extension of the four-phase framework in which the seismic forward response is governed by effective-medium rock-physics formulations, allowing ice to contribute to elastic frame stiffness. Within this framework, seismic data constrains the relationship between ice distribution and elastic response, while ERT primarily identifies frozen versus unfrozen portions of the subsurface under Archie-type assumptions.

Frozen soils and rock glaciers are treated conceptually as two end-members of ice distribution in the subsurface, representing pore-filling and massive ice, respectively. Synthetic experiments are designed to simulate these end-members as well as intermediate states through patchy mixtures of pure-ice and ice-in-pore domains. Ice-related elastic properties are modelled using a modified self-consistent approximation scheme following Stemland et al. (2020), while electrical resistivity remains primarily controlled by liquid water content. Synthetic seismic and electrical datasets are subsequently inverted using the different inversion schemes.

The results demonstrate that both independent EMT-based and phase-based petrophysical joint inversions are generally able to fit the seismic and electrical datasets by adjusting phase fractions, thereby providing robust first-order estimates of ice presence but limited discriminatory power with respect to ice type. In contrast, the introduction of rock-physics formulations in which ice contributes to the elastic frame leads to asymmetric sensitivities of seismic and electrical data. Under controlled assumptions, this asymmetry allows testing whether observed seismic and electrical anomalies are physically consistent with pore-filling or mechanically active ice scenarios. While unique identification of ice type is not achievable, the proposed approach enables the rejection of physically inconsistent interpretations and highlights the role of rock physics as a diagnostic tool for reducing ambiguity in the interpretation of periglacial environments.

References

Archie, G. E.; 1942. The electrical resistivity log as an aid in determining some reservoir characteristics. Transactions of the AIME, 146, 54–62.

Hauck C., Böttcher M. & Maurer H.; 2011: A new model for estimating subsurface ice content based on combined electrical and seismic data. The Cryosphere, 5, 453–469. ISSN 1994-0424. https://doi.org/10.5194/tc-5-453-2011.

Mollaret C., Wagner F.M., Hilbich C., Scapozza C. & Hauck C.; 2020: Petrophysical joint inversion of electrical resistivity and refraction seismic applied to alpine permafrost to image subsurface ice, water, air, and rock contents. Frontiers in Earth Science, 8, 85. ISSN 2296-6463. https://doi.org/10.3389/feart.2020.00085.

Stemland H. M., Johansen B. O., Ruud B. O., Mavko G.; 2020: Elastic properties as indicators of heat flux into cold near-surface Arctic sediments. *Geophysics*; 85 (5): MR309–MR323. doi: https://doi.org/10.1190/geo2019-0662.1

Wagner F. M., Mollaret C., Günther T., Kemna A., Hauck C.; 2019: Quantitative imaging of water, ice and air in permafrost systems through petrophysical joint inversion of seismic refraction and electrical resistivity data, Geophysical Journal International, Volume 219, 1866–1875, https://doi.org/10.1093/gji/ggz402

Corresponding author: aryleonel.mino@phd.units.it

Ambient vibration analysis on Cà di Sotto earthflow (Northern Italy)

E. Paolucci[1], A. Zuccarini[2], M. Zanetti[1], A. Armigliato[1], M. Bartola[2], M. Berti[2], S. Castellaro[1], N. Dal Seno[2], E. Ioriatti[2], R. Rani[2], F. Zaniboni[1].

[1] Department of Physics and Astronomy "A. Righi", University of Bologna, Bologna, Italy
[2]Department of Biological, Geological and Environmental Sciences, University of Bologna, Bologna, Italy

Slope destabilization events of various types, sizes and velocities affect mountainous and hilly areas and can have a significant impact on life and material damage of private and public properties. The risk can be reduced by anticipating slope failures thanks to early-warning systems, which usually involve monitoring ground deformation, rainfall, or groundwater levels. To do this, an adequate knowledge of the internal structure of the materials involved and their mechanical properties should be required.

In the last decades, geophysical methods have been used as an indirect approach to investigate the internal structure of landslides, as well as their hydrological and mechanical properties, with particular focus on earthflows (e.g., Jongmans and Garambois, 2007), providing insights into their dynamics through monitoring. In this framework, seismic methods can be considered suitable for retrieving the reference engineering-geological model of the landslide bodies; given their greater penetrating capacity compared to active techniques, measurements based on the acquisition of the ambient vibration wavefield can be of great help when huge accumulation volumes are involved in the slope failure.

The aim of this work is to show the preliminary results of the ambient vibration survey performed in the Cà di Sotto earthflow, located in the municipality of San Benedetto in Val di Sambro (about 30 km from Bologna), in the Northern Apennines. This landslide reactivated in June 1994 and again in October 2024 after 30 years of dormancy following an extreme rainfall event. The Cà di Sotto earthflow spans approximately 2 km in length and 200 m in width; the area involved is about 430000 m^2, with an estimated volume of 5-10 million m^3. Following its reactivation in 2024, the displacement of the landslide mass has been monitored through periodic and continuous GNSS measurements, hourly readings from an automated total station, and qualitatively documented using time-lapse cameras.

In addition to estimating the thickness of the deposits and reconstructing the reference engineering-geological model of the area, the initial aim of this activity was to investigate the relationships between the variations of the seismic velocity of the materials over time, the meteorological events and the eventual reactivation of the landslide (or the onset of its small localized movements). To try to accomplish these results, 48 seismic three-component nodes made available by the INGV ESITO Laboratory (https://www.ingv.it/monitoraggio-e-infrastrutture/laboratori/laboratorio-effetti-di-sito) were used: in particular, the use of these instruments was obtained through the national open access supported by ILGE-MEET project (https://ilge.ct.ingv.it/). The seismic instrumentation was deployed in two distinct areas of the landslide body: a set of 35 nodes was installed on the toe, and 13 were located in the middle part, at about 700 m from the valley floor. The first zone was chosen due to the considerable movements that affected this part after the 2024 reactivation during significant rainfall. The geometry selected for the first deployment was of the concentric type, with a sensor located on the center and the others placed on circles with different radii (about 3, 10, 30, 50, 70, 100 m); the minimum inter-sensor distance was 3 m and the maximum of about 200 m. A similar deployment was also chosen for the other zone, where the radii of the concentric circles were 3 and 15 m. Moreover, some sensors were placed on the stable ground on both sides of the landslide; for the toe area and for the upper area, a pair and 3 sensors were installed in this condition, respectively. After completing the installation, the ambient vibration wavefield was acquired continuously for 14 days (starting from 6/05/25 to 20/05/25) at 250 Hz: despite a few episodes of heavy rainfall during this period, these meteorological events did not result in significant displacements of the monitored landslide body.

Despite that, Horizontal to Vertical Spectral Ratios (HVSRs) and Rayleigh phase velocity dispersion curves were computed for every hour in order to check if significant differences occurred over time. In the first case, the analysis was performed using the HVNEA tool (Vassallo et al., 2023): the outcomes show a clear peak amplitude increase related to specific periods, associated to safety works located in the downstream area. Taking advantage of the presence of these noisy periods, which are characterized by a specific directionality, an evaluation of linear array reliability for velocity changes monitoring was performed. Finally, through joint inversion procedures of the HVSR and dispersion curves, the shear wave velocity profile for different zones of the study area was computed: this last step allowed to define the main features of the landslide deposits and the reference engineering-geological model that can be taken into account for subsequent stability analyses.

References

Jongmans D., Garambois S.; 2007: Geophysical investigation of landslides: a review. Bulletin de la Societe Geologique de France 178, 101–112, https://doi.org/10.2113/ gssgfbull.178.2.101.

Vassallo V., Riccio G., Mercuri A., Cultrera G., Di Giulio G.; 2023: HV Noise and Earthquake Automatic Analysis (HVNEA). Seismol. Res. Lett., 94, 350-368, doi: 10.1785/0220220115.

Acknowledgements

This study was carried out within the RETURN Extended Partnership and received funding from the European Union Next-GenerationEU (National Recovery and Resilience Plan – NRRP, Mission 4, Component 2, Investment 1.3 – D.D. 1243 2/8/2022, PE0000005).

A special thanks to INGV ESITO Laboratory Team (G. Di Giulio, G. Cultrera, D. Famiani, A. Mercuri, G. Riccio, M. Vassallo) for the ambient vibration survey and HVNEA analysis support.

Corresponding author: enrico.paolucci3@unibo.it

An eigenfrequency abacus for rapid estimation of block volumes from seismic noise measurements

Veronica Pazzi[1], Simone Francesco Fornasari[2], Stefano Devoto[2], Giovanni Costa[2], Emanuele Forte[2]

[1] *Department of Earth Sciences, University of Florence, Florence, Italy*
[2] *Department of Mathematics, Informatics, and Geosciences, University of Trieste, Trieste, Italy*

Introduction

Estimating the volume of rock masses is fundamental for the landslide characterization in areas prone to detachment, but it is challenging. The orientation and properties of discontinuities play a fundamental role. It has been shown that rock blocks' volume could be underestimated if joints are erroneously assumed to be persistent, or overestimated if they are not fully detected. Unfortunately, in common practice, it is not easy to define the blocks' volume because it is quite hard to estimate the actual shape and in particular the height of a block: non-open discontinuities, in fact, affect the portion of the block actually separated, influencing the height that has to be considered in the volume estimation.

In engineering geology and geophysics, natural frequency refers to the fundamental modes of vibration of materials, rock masses, soil layers, entire slopes, as well as different man-made structures. A variety of studies have explored the natural frequency and resonance phenomena across contexts such as rock mass stability, slope resonance, sedimentary basin amplification, and material characterisation, using both experimental and numerical approaches. The simplest model proposed in literature to calculate the natural or fundamental resonance frequency f_0 of a rock assimilates the rock to a single-degree-of-freedom block (i.e., free to vibrate only in the vertical plane) and the rock-slope connection to a tension-compression spring (Xie et al., 2021). Thus, f_0 is a function of the physical properties of the block, i.e., its mass and the stiffness. However, along with the vertical vibration, an object can also perform swaying or rotational vibrations, which make the calculations more complex. Relations that link the natural frequency to other physical parameters of the object are frequently used to derive the mechanical parameters from the measured (or modelled) natural frequency by fixing the mass as a constant. Alternatively, they can be used to estimate the natural frequency of an object with a fixed mass based on its measured or estimated mechanical parameters.

The main objective of this study is to estimate the volume (i.e., the mass) of rock blocks using the frequency f_{HV}, i.e., that estimated from H/V passive seismic geophysical measurements (Nakamura, 1989; Kleinbrod et al., 2019; Molnar et al., 2022), which is considered a good approximation/estimator of f_0 (the block eigenfrequency). In fact, as reported in literature by several authors (e.g., Got et al., 2010; Kleinbrod et al., 2019; Galea et al., 2014; Iannucci et al., 2020), from seismic noise data it is possible to identify frequencies that are linked to the volume of blocks (normal-mode vibrations) rather than to stratigraphic resonance effects, as usually supposed. These frequencies are the eigenfrequencies of the block and could be visible (or not if the vertical component is amplified) as peaks in the H/V curve but are always characterised by a strong polarisation normal to the dominant fracture network and by a strong linearity of the ellipticity (Burjánek et al., 2010; Kleinbrod et al., 2019; Iannucci et al., 2020). Therefore, this work presents an *ad hoc*-developed eigenfrequency-volume abacus, and the procedure to employ it to obtain an approximation of the order of magnitude of the block's volume.

Methods and Results

In the majority of real cases, the eigenfrequency of a block cannot be obtained by means of analytical equations but requires specific numerical simulations. Blocks with small geometric ratios W/Z^2, being W the smallest horizontal dimension (i.e., the thickness against which bending occurs) and Z the height of the block, can be approximated to an Euler–Bernoulli cantilever with rectangular cross section, as they share similar boundary conditions (i.e. in both cases the structures are rigidly fixed at their base and free at the other side). Thus, the eigenfrequency-volume abacus was built calculating the regression curves of simulated data. The numerical simulations, based on the finite element method implemented in the CalculiX software, provided the natural resonance frequencies of homogeneous rock blocks with defined dimensions and material properties. Because the eigenfrequency-volume relation varies for each specific geological background, the numerical simulations were carried out by fixing certain mechanical parameters based on the study area.

To validate the abacus seismic noise datasets, acquired along the northwestern coast of Malta Island (central Mediterranean Sea) at two distinct test sites, namely Anchor Bay (Il-Prajjet) and Il-Qarraba peninsula, were used. These two sites were selected because independent measures of the blocks' volumes and areas are available from field measurements, direct observations, and feature analysis using satellite images and the outcomes of UAV-Digital Photogrammetry technique (Devoto et al., 2020).

The numerical simulations were carried out assuming that: a) the blocks are singular rectangular cuboids with different aspect ratios for their horizontal dimensions, as well as being of multiple heights; b) each block has been constrained at its base using a fixed boundary condition (that is quite realistic for the test sites, as the blocks are separated from each other laterally by persistent fractures, while at their base, they are locked by - and sometimes sunk - into a clay layer (Blue Clay Formation); c) the properties of the materials have been selected from available estimates in literature (Iannucci et al., 2018; Iannucci et al., 2020) and in particular: the Young modulus is set to $E = 3.04\ GPa$, the density is set to $\rho = 1900$ kg/m^3, and the Poisson ratio is fixed to $\nu = 0.25$. These parameters correspond to a S-wave velocity of about 850 m/s, in agreement with the literature. The selection of a homogeneous composition and fixed boundary conditions represents key model assumptions made to simplify the analysis of the results while making them more general. In reality, it is clear that the composition is never actually homogeneous, even at a very local scale. This could lead to inaccuracies in the parametrisation. However, a constant value can usually be considered a good enough approximation at least for order-of-magnitude estimates, as in the present case. The vibration mode with the lowest frequency with displacement along a specific axis have been extracted from the results of each simulation. The obtained abacus is shown in Fig. 1.

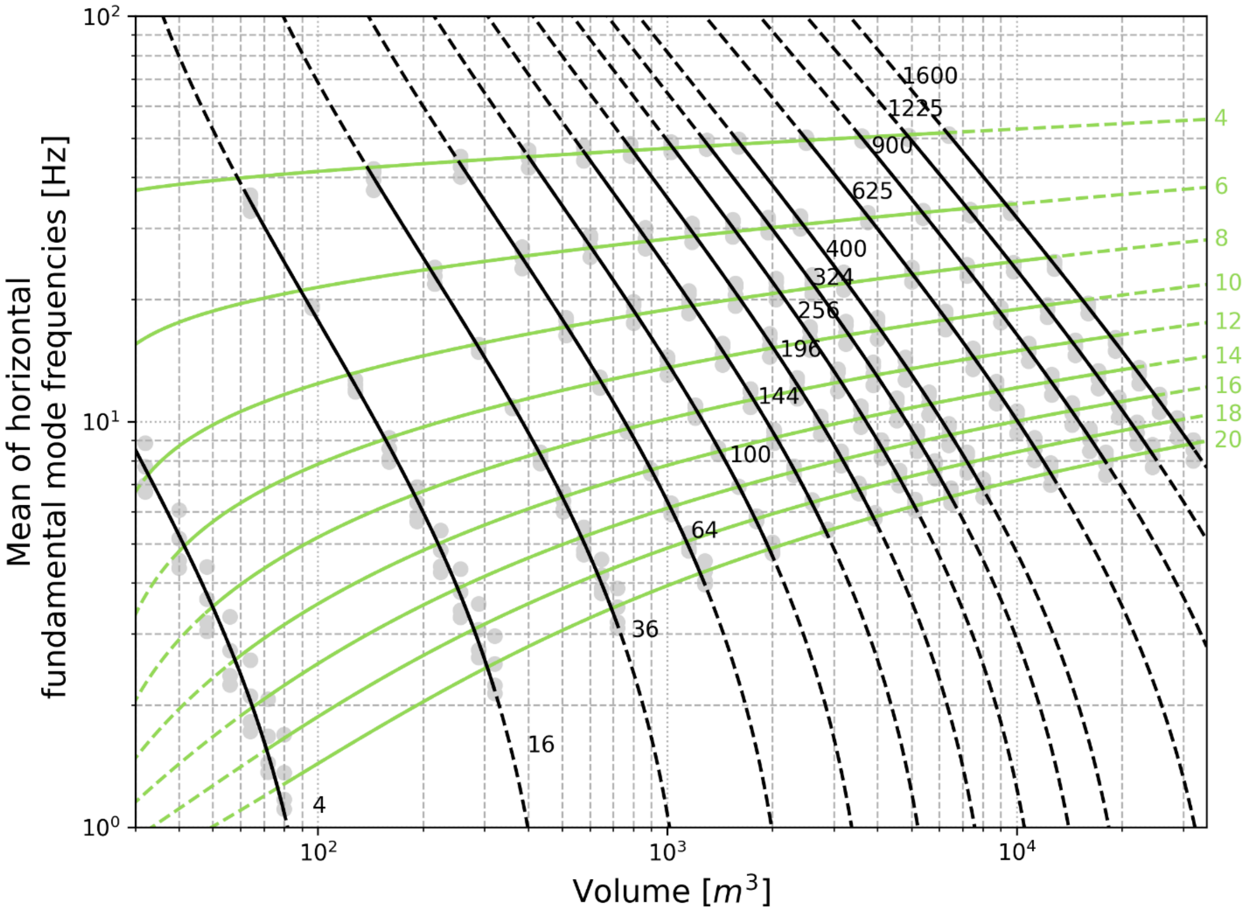

Fig. 1 – Eigenfrequency-volume abacus. The trend of the average of the horizontal fundamental frequency is shown as a function of the volume, given a fixed surface area (black curves) or a fixed height (light green curves). The grey dots represent the simulation results used for the regression. The dashed lines represent the extrapolated trends.

The result of the numerical simulations can be summarised as follows: given a specific site, the expected block's natural frequency f_0 (being f_0 the lowest values between f_W and f_L) is inversely proportional to the block's volume, with f_0 tending to zero for blocks of infinite size (e.g., a stable area in mountainous sites or a compact plateau located on the edge of a cliffs, like in the present case).

In the field, it is hard to evaluate f_0, while, as already shown by some works (Got et al., 2010; Kleinbrod et al., 2019; Galea et al., 2014; Iannucci et al., 2018, 2020) and remarked in the Introduction, it is easier to estimate the block natural frequency by the H/V curves (f_{HV}). Thus, a procedure to estimate the volume of a block from the results of the H/V curves is proposed and summarised in Fig. 2.

The proposed procedure is divided in six steps: Step 1: select the study area and acquire seismic noise data; Step 2: analyse data to obtain H/V curves, spectra of the three components, particle motion, directivity, and polarisation analysis; Step 3: integrate results and identify the different frequencies (e.g., identifying and not considering those related to stratigraphic picks, which are common to all measures, or those related to human activities); Step 4: estimate the area (A) of the block by independent data; Step 5: enter the abacus with values of Step 3 and Step 4; Step 6: estimate the volume.

The procedure’s step that allows to identify different typologies of H/V peaks (Step 3) is not trivial or straightforward and must comply with various criteria, including the analysis of the shape of the spectra of the three components, as well as that of the results of the polarisation analysis.

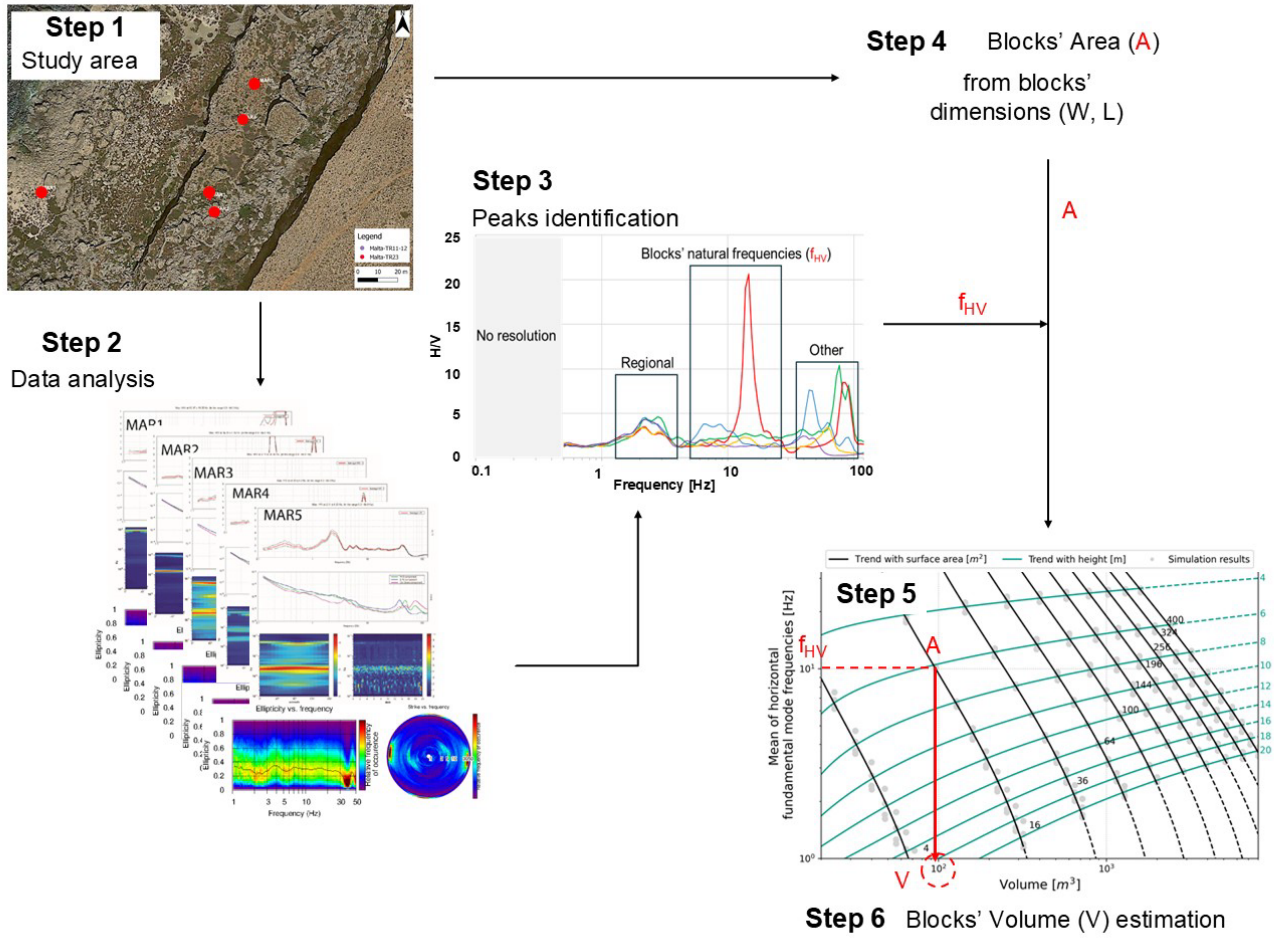

Fig. 2 – Pictorial diagram of the proposed procedure to estimate the block’s volume from seismic noise measurements using the proposed abacus (modified from Pazzi et al., 2025).

The obtained abacus and procedure were validated by means of seismic noise data recorded in two sites. In particular, for each seismic noise measure a f_{HV} value was selected on the basis of the strike and of the ellipticity, and the volume of the block was retrieved from the eigenfrequency-volume abacus, knowing the block’s area from available independent data. The value obtained from the abacus was then compared with that calculated by means of these independent measures available. For three selected measures, Fig. 3a illustrates the H/V curves as well as the area and volume values obtained by independent measurements, Fig. 3c shows the ellipticity and the strike, and Fig. 3b the volume obtained by means of the abacus.

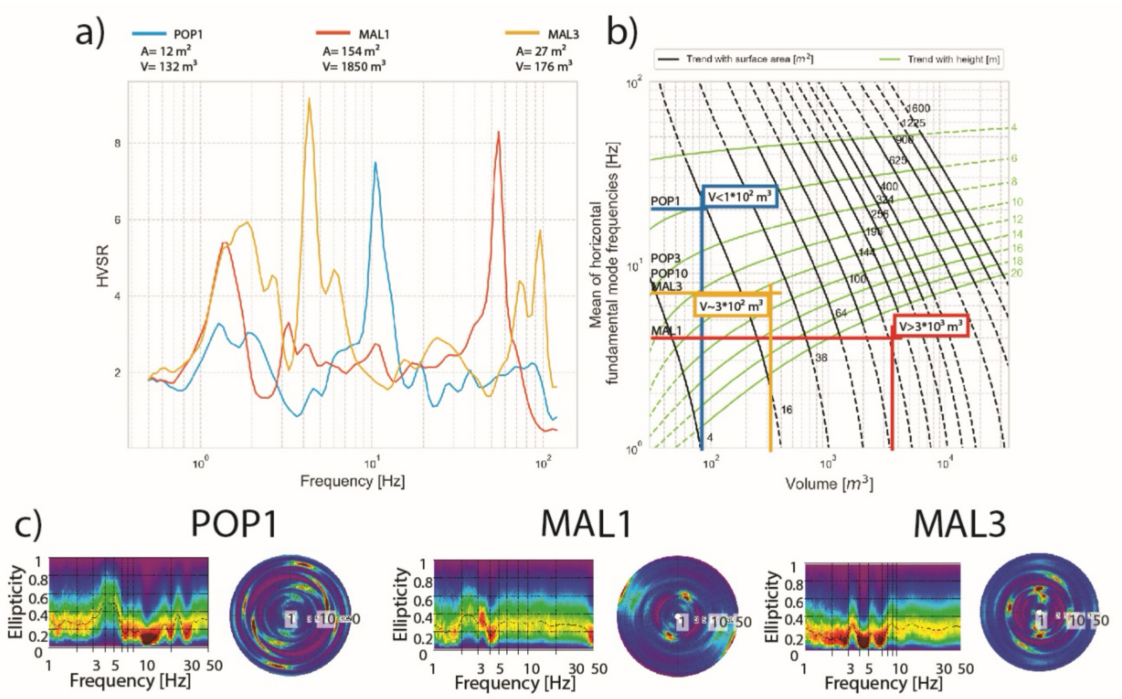

Fig. 3 – Some selected H/V curves. a) For each acquisition, the value of the area (*A*) used in panel b) and that of the volume (V) obtained by independent measures is indicated, while the ellipticity and strike are shown in panel c). b) Illustration of the Step 6 of the procedure for the selected blocks.

Discussion and Conclusions

The rationale behind this work is that some peaks of the H/V curves acquired over rock blocks are not linked to the geological regional stratigraphy of the site, but rather to the volume of the blocks themselves. Thus, the f_{HV} has been considered as a proxy of the block natural frequency f_0, and a procedure to estimate the blocks' volume from the H/V curves has been developed. Synthetic and field data collected at two different sites in Malta Island demonstrated the effectiveness of the proposed procedure, which has some inherent limitations. First of all, if the stratigraphy of the study area is not known, or it is very complex and inhomogeneous, or it is not possible to highlight volume-controlled frequencies, the proposed procedure cannot be applied. Secondly, a robust selection of the correct f_{HV} is essential to the practical application of the proposed method, because an incorrect selection of this frequency would result in an incorrect volume estimate. Nevertheless, we experienced that an error of ±1 Hz in the estimation of f_{HV} does not significantly affect the estimation of the volume's magnitude order. Thirdly, the eigenfrequency-volume abacus was built based on specific geophysical and rheological parameters, thus it cannot be applied in sites where these characteristics are very different. A different abacus must be therefore implemented, considering different geophysical and rheological parameters in the modelling.

On the other hand, the main advantages of the proposed abacus are that seismic noise measures can be performed quite easily and that the two horizontal dimensions of the blocks can often be straightforwardly estimated exploiting UAV-DP or satellite-images. Moreover, it is important to highlight that some deviations between the data calculated with the proposed geophysical method (the abacus) and the field-derived measurements may be linked to a different persistence of the fracturing than expected/considered. The presence of discontinuities, in fact, affects the shear-wave velocity. Therefore, the study of specific blocks, especially contiguous ones, may require different boundary conditions, as these may have a major influence on the results of the simulations. the persistence and aperture of the fractures play a fundamental role in controlling the block's volume prone to falling. Thus, if some seismic noise measures are acquired over a rock cliff and the volumes estimated (V_{est}) applying the abacus are different from the one calculated by independent measures (V_{calc}), this means that the aperture and persistence values of the visible discontinuities are different from expected. In particular, if V_{est} is lower than V_{calc}, it means that the fractures are less persistent and only partially isolate the blocks, differently from field-derived observations. On the contrary, if V_{est} is higher than V_{calc}, it means that the discontinuities are more persistent than they seem, possibly completely isolating the analysed block from the surrounding rock masses.

Future research will extend the field examples to consider different geological backgrounds, lithologies and geometries. For more information on the abacus and its use in the study areas, please refer to Pazzi et al., (2025).

Acknowledgments

We would like to thank Prof. Mauro Soldati (University of Modena e Reggio Emilia, Italy) for giving us the opportunity to start researching landslides in Malta and Darren Saliba (Il-Majjistral Natural Park, Malta) for the technical support during all the acquisition campaigns.

References

Burjánek, J., Gassner-Stamm, G., Poggi, V., Moore, J. R., Fäh, D.; 2010: Ambient vibration analysis of an unstable mountain slope. Geophysical Journal International, Vol. 180, pp. 820–828, https://doi.org/10.1111/j.1365-246X.2009.04451.x.

Devoto, S., Macovaz, V., Mantovani, M., Soldati, M., Furlani, S.; 2020: Advantages of using UAV digital photogrammetry in the study of slow-moving coastal landslides. Remote Sensing, Vol. 12, pp. 3566, https://doi.org/10.3390/rs12213566.

Galea, P., D'Amico, S., Farrugia, D.; 2014: Dynamic characteristics of an active coastal spreading area using ambient noise measurements—Anchor Bay, Malta. Geophysical Journal International, Vol. 199, pp. 1166–1175, https://doi.org/10.1093/gji/ggu318.

Got, J. L., Mourot, P., Grangeon, J.; 2010: Pre-failure behaviour of an unstable limestone cliff from displacement and seismic data. Natural Hazards and Earth System Sciences, Vol. 10, pp. 819–829, https://doi.org/10.5194/nhess-10-819-2010.

Iannucci, R., Martino, S., Paciello, A., D'Amico, S., Galea, P.; 2018: Engineering geological zonation of a complex landslide system through seismic ambient noise measurements at the Selmun Promontory (Malta). Geophysical Journal International, Vol. 213, pp. 1146–1161, https://doi.org/10.1093/gji/ggy025.

Iannucci, R., Martino, S., Paciello, A., D’Amico, S., Galea, P.; 2020: Investigation of cliff instability at Għajn Ħadid Tower (Selmun Promontory, Malta) by integrated passive seismic techniques. Journal of Seismology, Vol. 24, pp. 897–916, https://doi.org/10.1007/s10950-019-09898-z.

Kleinbrod, U., Burjánek, J., Fäh, D.; 2019: Ambient vibration classification of unstable rock slopes: A systematic approach. Engineering Geology, Vol. 249, pp. 198–217, https://doi.org/10.1016/j.enggeo.2018.12.012.

Molnar, S., Sirohey, A., Assaf, J., Bard, P.Y., Castellaro, S., Cornou, C., Cox, B., Guillier, B., Hassani, B., Kawase, H., Matsushima, S.; 2022: A review of the microtremor Horizontal-to-Vertical Spectral Ratio (MHVSR) method. Journal of Seismology, Vol. 26, pp. 653–685, https://doi.org/10.1007/s10950-021-10062-9.

Nakamura, Y.; 1989: A method for dynamic characteristics estimation of subsurface using microtremor on the ground surface. Railway Technical Research Institute Quarterly Report, 30.

Pazzi, V., Fornasari, S.F., Devoto, S., Costa, G., Forte, E.; 2025: Fast estimation of landslide blocks’ volume from seismic noise measurements. Communications Earth & Environment, 10.1038/s43247-025-02999-3.

Xie, M., Liu, W., Du, Y., Li, Q., Wang, H.; 2021: The evaluation method of rock mass stability based on natural frequency. Advances in Civil Engineering, 1 (2021), 6652960, https://doi.org/10.1155/2021/6652960.

Corresponding author: veronica.pazzi@unifi.it

Advancing petrophysical coupling of electrical and seismic tomographic data including shear waves

Guido Penta de Peppo[1], Michele Cercato[1], Giorgio De Donno[1]

[1] *"Sapienza" University of Rome – DICEA*

Petrophysical characterization, widely applied in deep geophysical investigations such as reservoir exploration, remains challenging in the near-surface environments due to the strong complexity and variability of shallow subsurface properties (Linde and Doetsch, 2016). High-resolution tomographic imaging offers significant potential, as the spatial distribution of these properties is typically inferred qualitatively from geophysical data, with broad implications for civil and environmental applications.

Electrical resistivity tomography (ERT) is sensitive to key properties such as porosity, fluid content, and pore-fluid conductivity (Archie, 1942), while seismic refraction tomography (SRT) maps variations in elastic properties related to density and porosity (Wyllie et al., 1956). Induced polarization (IP) further enhances the detection of fine-grained materials and fluid- or composition-related contrasts. Over recent decades, the integration of electrical and seismic methods has significantly improved imaging resolution and reduced interpretational bias, with structural joint inversion approaches (e.g., Penta de Peppo et al., 2024) becoming widely adopted. These strategies are generally preferred to explicit petrophysical coupling in the near surface, where empirical relationships are less reliable due to pronounced heterogeneity (Linde and Doetsch, 2016).

Wagner et al. (2019) introduced a petrophysical joint inversion (PJI) framework combining ERT and SRT for quantitative permafrost characterization. Penta de Peppo et al. (2025) extended this framework by incorporating IP data through advanced electrical modelling, enabling applications beyond rock glaciers, such as coastal aquifer characterization.

The seismic modelling underlying these approaches is commonly based on Wyllie's equation (1959), which relates compressional-wave velocities to porosity through average travel times. However, this relation is known to overestimate velocities when porosity exceeds 40% (Paillet and Cheng, 1991), or when pores contain gas, the rock is incompletely lithified, or fractures are present (Saleh and Castagna, 2004). Consequently, porosity estimates in high-porosity or structurally complex near-surface materials remain approximate, and Wyllie's relation is more suitable for qualitative trend assessment than for quantitative characterization.

To address these limitations, we developed a PJI framework that jointly integrates SH-wave SRT with ERT and, optionally, time-domain IP data. The robustness and effectiveness of the approach are evaluated by comparing results with those obtained using conventional P-wave seismic data, following the algorithm described by Penta de Peppo et al. (2025).

Preliminarily, we tested our algorithms on a synthetic model, resembling a typical range of variation of parameters encountered for geophysical investigation on unconsolidated sediments. The synthetic example is a four-layer petrophysical model (Figs. 1g, 1i, 1k and 2g, 2i, 2k), consisting of an unsaturated shallow layer (0-3 m), overlying a saturated unit exhibiting strong lateral (from 0.4 to 0.7) and vertical (from 0.4 to 0.2) porosity variations. After converting the data into geophysical models for both the P-wave (Figs. 1a, 1c, 1e) and S-wave (Figs. 2a, 2c, 2e) cases, we simulated the tomographic datasets using an acquisition geometry including 48 sensors (electrodes and geophones) spaced 2 m apart. The results of PJI are shown in terms of petrophysical parameters in Figs. 1f, 1h, 1j, 1l and 2f, 2h, 2j, 2l, for P-wave and S-wave data, respectively. The conversion to geophysical cross-sections is also presented for the sake of completeness in Figs. 1b, 1d, 1f and 2b, 2d, 2f, for a visual comparison with the starting models.

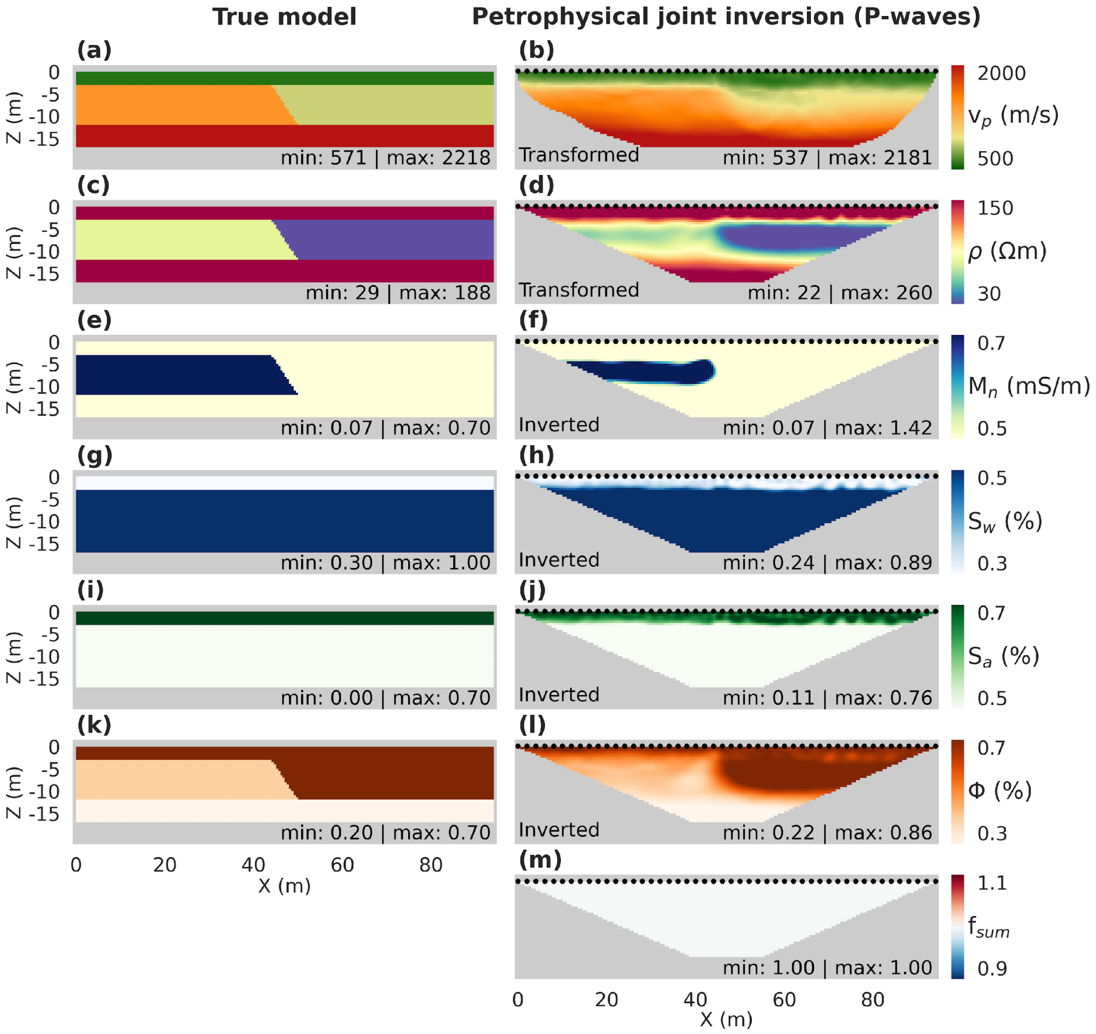

Fig. 1 – Synthetic model (left) and inversion results (right) including P-waves.

Although in both cases the transition between unsaturated to saturated conditions is accurately depicted (Figs. 1f, 1h and 2f, 2h), the values of the high-porosity zone are much closer to the true one when including shear waves (maximum value of 0.74 for the SH-wave case compared to 0.86

for P-wave case), together with an improvement in the reconstruction of geometry of the steep layer interface. In both cases, the joint inversion ensures physically consistent results, with the sum of the volumetric fractions equal to one in each cell (Figs. 1m and 2m).

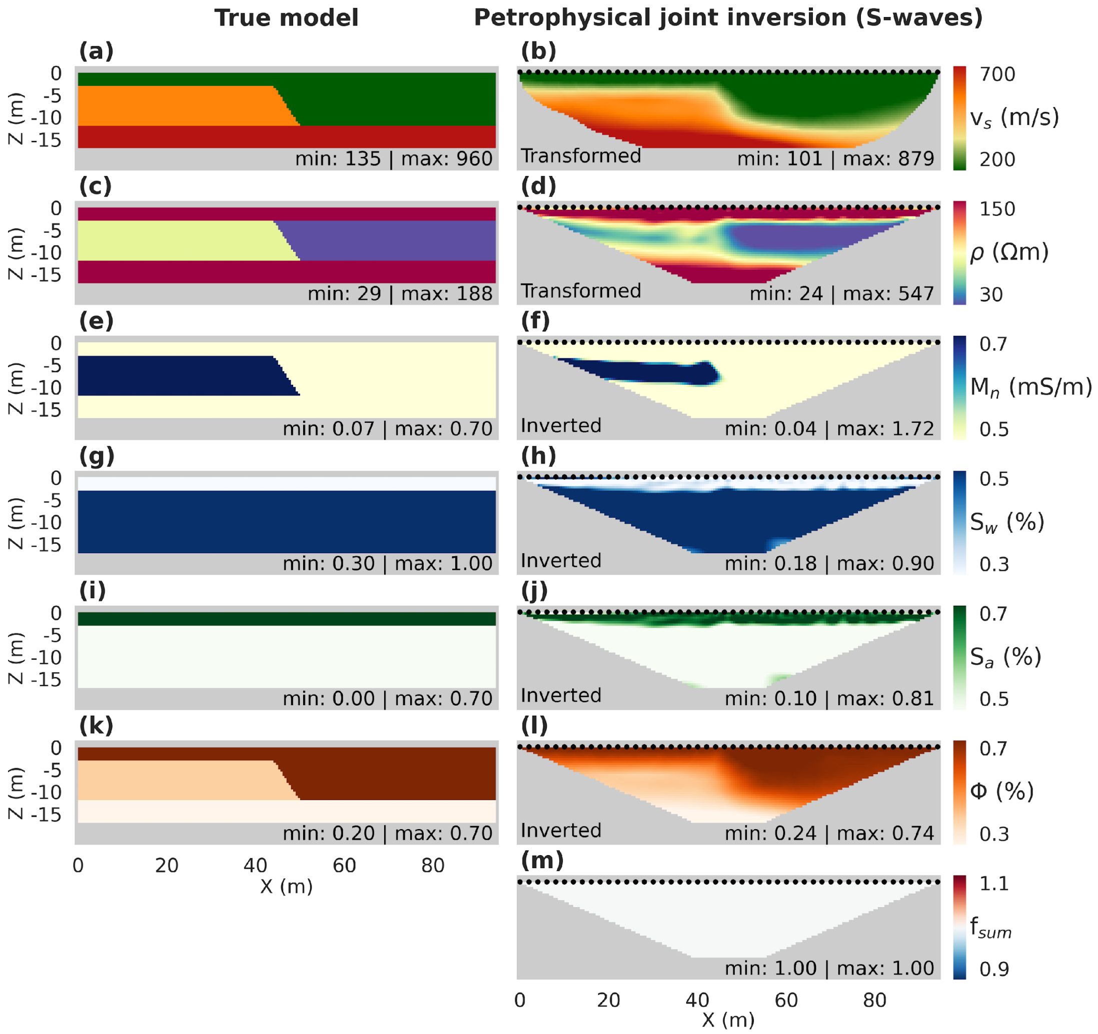

Fig. 2 – Synthetic model (left) and inversion results (right) including SH-waves.

The proposed methodology was applied to the Pontine Plain field case (Penta de Peppo et al., 2025). While air and water saturation reconstructions (Figs. 3g, 3i and 3h, 3j) and their conversion to geophysical quantities (Figs. 3a, 3c, 3e and 3b, 3d, 3f) are largely insensitive to whether P- or S-wave data are included, porosity estimates differ substantially (Figs. 3k and 3l). Although lateral and vertical trends are consistently recovered in both cases, inversions incorporating S-wave data yield more reliable porosity values, consistent with those expected for sandy materials with silt–clay inclusions.

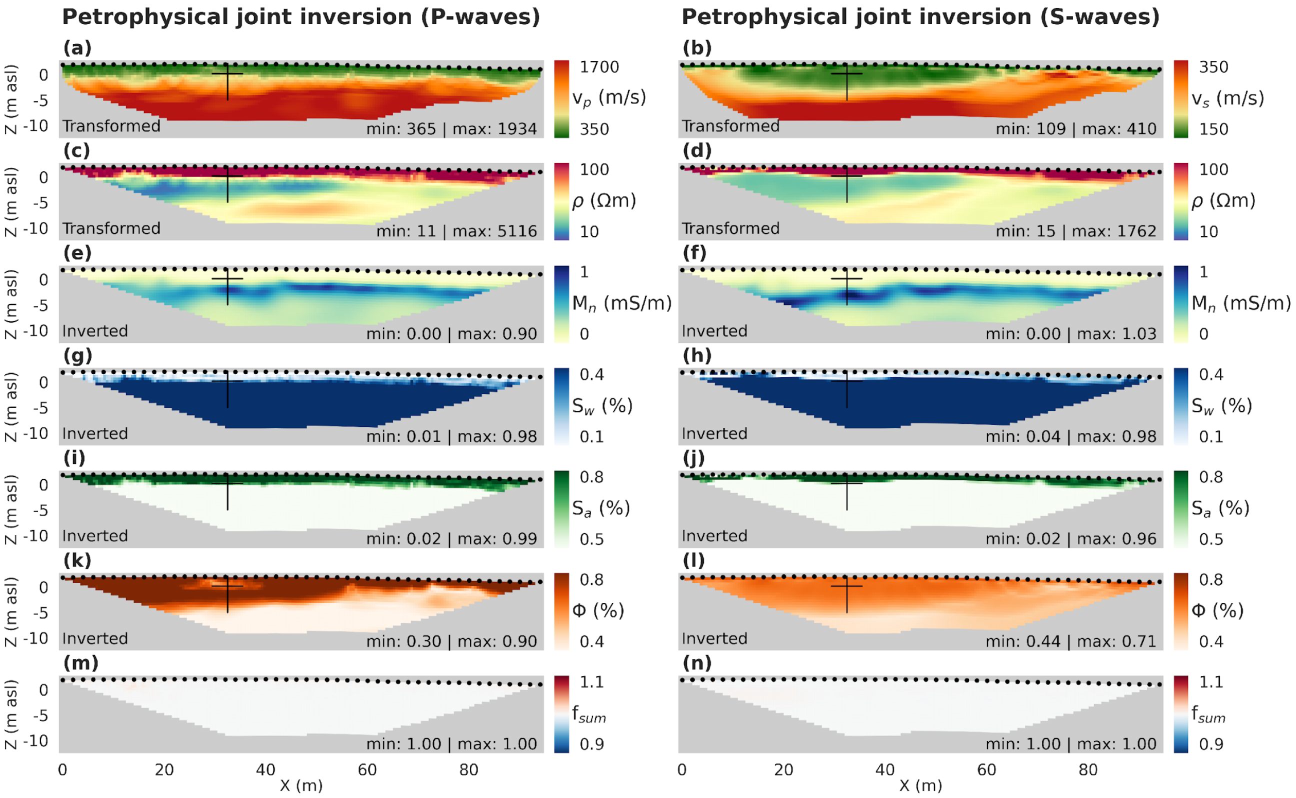

Fig. 3 – Inversion results at the Pontina Plain field case including P-waves (left) and SH-waves (right).

The presented results show that, while the framework proposed by Penta de Peppo et al. (2025), incorporating P-wave data, provides excellent estimates of saturation levels, porosity estimates are affected by the limitations of the Wyllie's model, yielding values that are qualitatively representative but less reliable in a quantitative sense. Conversely, the joint inversion scheme proposed in this study replacing P-wave with S-wave data and adopting a different seismic petrophysical model, achieves equally robust saturation estimates while significantly improving porosity estimation, both in terms of spatial trends and absolute values. Overall, the proposed PJI framework introduces a novel inversion approach capable of retrieving accurate petrophysical properties across a wide range of hydrogeological settings and represents a new tool for high-resolution near-surface characterization.

References

Archie G. E.; 1942: The Electrical Resistivity Log as an Aid in Determining Some Reservoir Characteristics. Trans., 146(01), 54–62.

Linde N. and Doetsch J.; 2016: Joint inversion in hydrogeophysics and near-surface geophysics, in Integrated Imaging of the Earth, 7, 119–135, Wiley.

Paillet F. L., and Cheng H. C.; 1991: Acoustic waves in boreholes, CRCPress.

Penta de Peppo G., Cercato M. and De Donno G.; 2024: Cross-gradient joint inversion and clustering of ERT and SRT data on structured meshes incorporating topography. Geophysical Journal International, 239(2), 1155–1169.

Penta de Peppo G., Cercato M. and De Donno G.; 2025 Petrophysical joint inversion of seismic refraction, resistivity and time-domain induced polarization tomographic data for quantitative imaging of coastal aquifers. GEOPHYSICS, in press.

Saleh A. A. and Castagna J. P.; 2004: Revisiting the Wyllie time average equation in the case of near-spherical pores. Geophysics, 69 (1), 45–55.

Wagner F. M., Mollaret C., Günther T., Kemna A. and Hauck C.; 2019(3): Quantitative imaging of water, ice, and air in permafrost systems through petrophysical joint inversion of seismic refraction and electrical resistivity data. Geophysical Journal International, 219, 1866–1875.

Wyllie M. R., Gregory A. R. and Gardner G.H.F.; 1956: Elastic wave velocities in heterogeneous and porous media. GEOPHYSICS, 21, 41–70.

Corresponding author: guido.pentadepeppo@uniroma1.it

Monitoring the alpine environment using fiber-optic cables: case-studies on permafrost seasonal fluctuations and snow-cover characterisation

N. Piana Agostinetti[1,2], A.Prokop[3], G. Crosta[1], B. Grasemann[3], A. Villa[1], E. Valbuzzi[1], B. Anwander[3], F. Riva[4], A. Caccia[1], L. Cifeca Recinella[1], D. Collino[1], M. Arcangeli[1], J. Ziegler[1] and G. Saccorotti[5]

[1]*Department of Earth and Environmental Sciences, University of Milan Bicocca, Italy.*
[2]*Istituto Nazionale di Geofisica e Vulcanologia, Osservatorio Nazionale Terremoti, Rome, Italy.*
[3]*Department of Geology, University of Vienna, Vienna, Austria.*
[4]*Scuola di Scienze e Tecnologie, Universita' di Camerino, Italy*
[5]*Istituto Nazionale di Geofisica e Vulcanologia, Sezione di Pisa, Pisa, Italy.*

Introduction

Monitoring the environment in remote and high-altitude areas is challenging, due to the harsh conditions and the lack of dedicated infrastructures, but necessary to understand the effect, for example, of climate changes. Monitoring such regions can be performed through the repeated analysis of satellite images recorded during subsequent orbits. However, remote sensing suffers from two main drawbacks: (a) orbit repetition is usually done over a period that can vary between one and two weeks (3-4 days in best case scenario, but using restricted, pay-walled data) which can only be useful for long-term, yearly, monitoring purposes and, moreover, in case of cloud coverage, the data can be of limited use for some frequency bands; and (b) the spatial resolution of satellite images is not high enough for monitoring single mountain slopes or specific areas. In this contribution, we present results from two different studies where fiber-optic (FO) cables have been installed for monitoring relevant elements of the alpine environment, namely the permafrost and the snow cover. Monitoring is performed using Distributed Acoustic Sensing (DAS) technology, which repurposes FO cables into distributed sensing units. The main advantages are that FO cables are relatively cheap and easy to install in remote areas, without the need of a difficult maintenance as done usually with sensor networks. The second advantage is that DAS technology is able to reach unprecedented spatial resolution (e.g. one sensor per meter of cable), opening to a number of innovative investigations.

Data and Methods

We present the results from two different experiments. The first has been held in Lech am Alberg (Austria), for multiple periods, from 2012-2013 and 2021-2025 (Prokop et al., 2023). During such surveys, we monitored man-made snow avalanches in a ski resort, where explosions are operated to reduce the snow avalanche risk on the ski track. The duration of the DAS recordings and FO cable geometry changed during the different years, from a S-shaped FO cable buried in the soil at shallow depth (2012-2013, Figure 1) to a shallow trenched cable in the snow cover (2021-2025, Figure 2). The seismic waves originated by the explosion have been analysed to measure the thickness and the P-wave seismic velocity of the snow cover. In fact, seismic waves travel in both the snow cover (as Guided waves trapped in the low velocity layer, and in the air. From analysis of the two seismic phases, and their frequency content, we are able to estimate the snow cover physical properties.

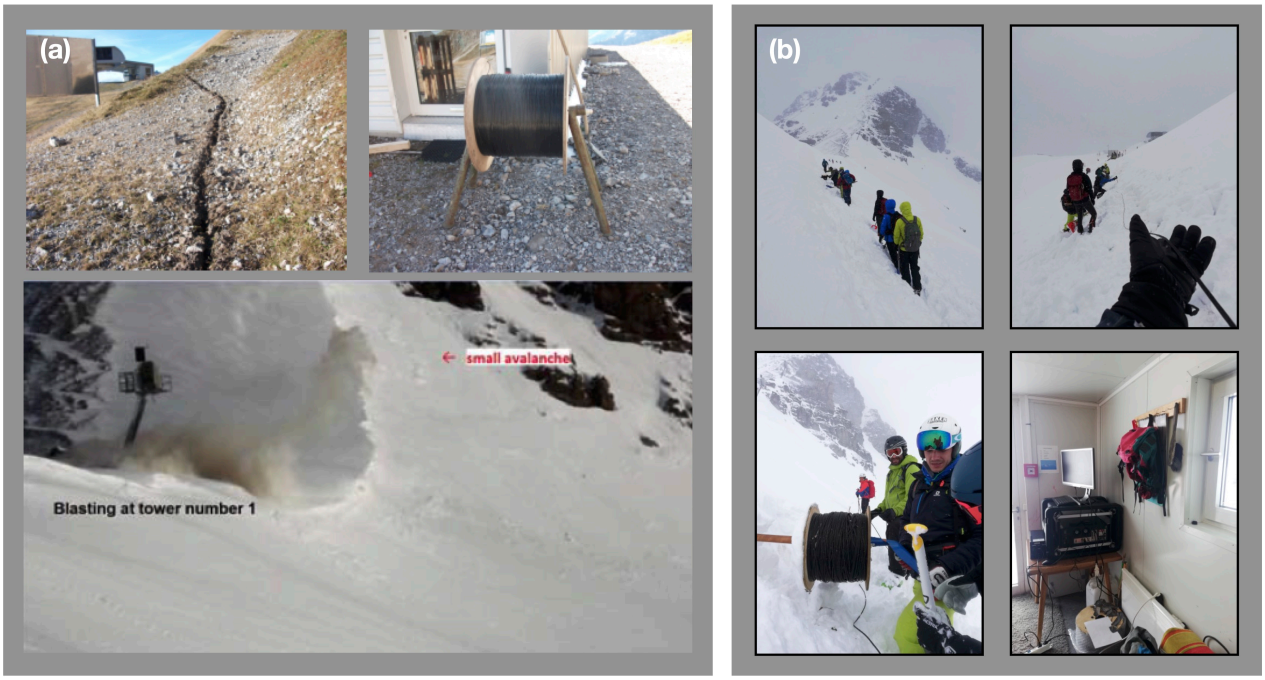

Figure 1: FO cable deployment in different years. (a) The 2012-2013 campaigns, where the FO cable was buried in the ground; (b) the 2021 campaign, where the FO cable was shallow trenched in the snow cover.

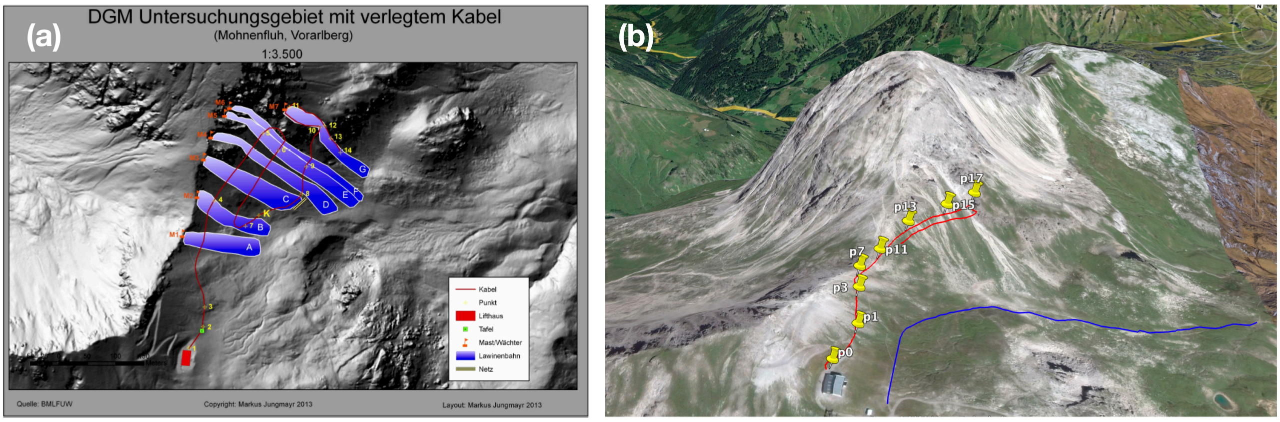

Figure 2: FO cable geometry in different years. (a) The 2012-2013 campaigns, where the FO cable has been deployed with multiples bending along the slope; (b) the 2021 campaign, where the FO cable was deployed with a single U-shaped track.

The second experiment has been held in the Alpine region close to Val D’Aosta, during the 2023 winter-to-summer season. During such period, the state of the permafrost has been monitored using anthropic seismic signals propagating regularly (four times per hour) along the mountain slope (Arcangeli, 2024). By cross-correlating the anthropic signal generated at the surface and recorded in the underground, we are able to measure the delay-time due to the propagation the signal through the frozen terrain. The seasonal variations of such delay-time can furnish a proxy for the state of the permafrost in such mountain slope.

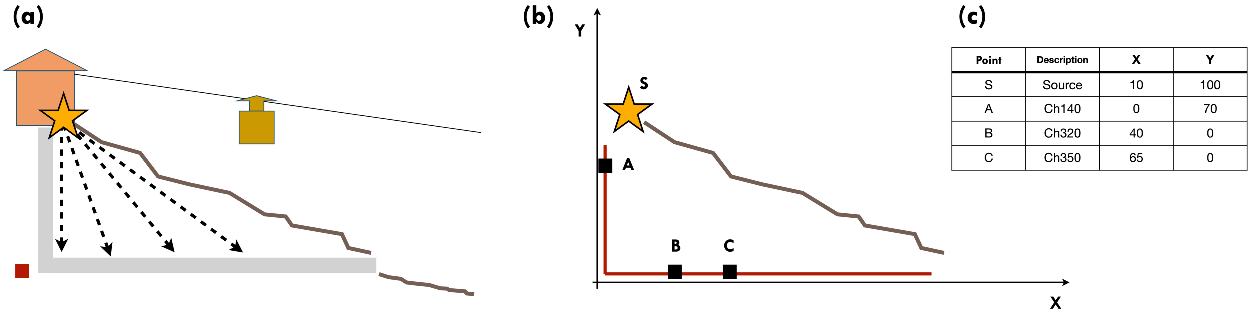

Point	Description	X	Y
S	Source	10	100
A	Ch140	0	70
B	Ch320	40	0
C	Ch350	65	0

Figure 3: Setting of the experiment for monitoring the state-of-the-permafrost in the Alpine region. (a) Sketch depicting the geometry of the geophysical investigation. The yellow star indicates the position of the anthropic source of seismic signals. The red square is the DAS interrogator units. The FO cable was installed along the grey-shaded tunnels. Arrows show the propagation of seismic waves across the mountains slope. (b) Details of the geometry of the FO cable. (c) Table of the relevant source and receiver positions.

Results

For our two case-studies, our preliminary results show that seismic properties of the snow cover, like thickness and P-wave velocity, can be measured along shallow buried FO cables, and can furnish key-information about the snow state useful, for example, for snow-avalanche risk management (Collino, 2024).

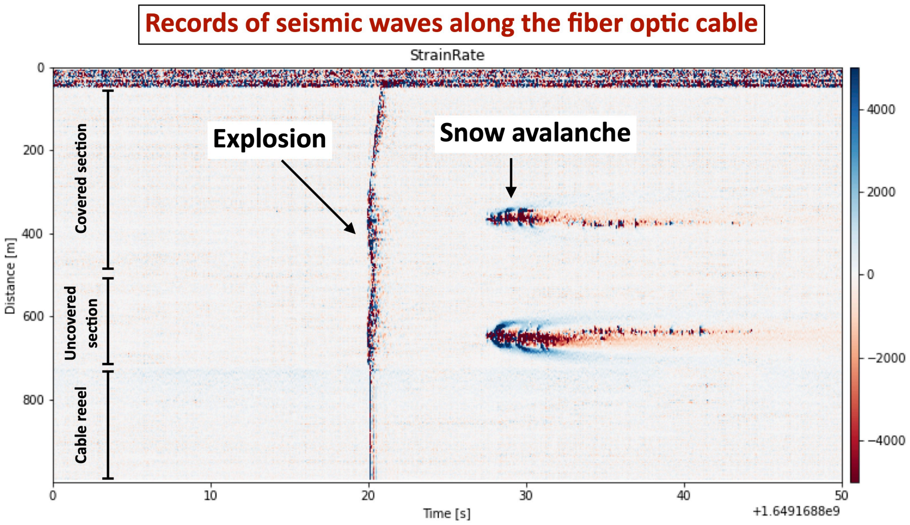

Figure 4: Seismic data recorded during a man-made explosion in Lech am Alberg, during the 2021 winter season. On the x-axis, time is displayed, on the y-axis the FO cable is reported. Color-scale refer to strain-rate along the single 1m-portion of the FO cable. After few seconds from the explosion, also recorded in the strain-rate data, the snow-avalanche passed on the FO cable.

Result from the second experiment show that seasonal variation of permafrost seismic properties can be retrieved with time-repeated DAS measurements of active sources, with potential implications in detecting alpine slope instabilities.

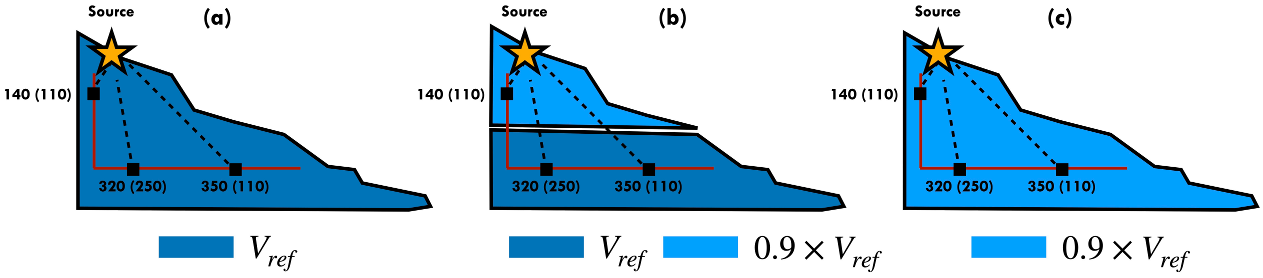

Figure 4: Conceptual sketch of the variation of seismic velocity retrieved from cross-correlation of the active source signals during different seasons.(a) Winter season; (b) Spring season; and (c) late summer season.

References

Arcangeli M. (2024) Analysis of persistent noise sources for monitoring rock elasticity in alpine terrain: a case-application for Distributed Acoustic Sensing data, Ms Thesis, Universita' degli Studi di Milano-Bicocca

Collino D. (2024) MEASURING SNOW-COVER PROPERTIES WITH DAS DATA, Ms Thesis, Universita' degli Studi di Milano-Bicocca

Prokop, A., Piana Agostinetti, N., and Grasemann, B. (2023) Measuring snow and avalanche properties using acoustic and seismic distributed fiber optic sensing, EGU General Assembly 2023, Vienna, Austria, 24–28 Apr 2023, EGU23-5851, https://doi.org/10.5194/egusphere-egu23-5851

Corresponding author: nicola.pianaagostinetti@unimib.it

Imaging the Buried Bedrock of the Venosta Valley (Italy) Using Seismic Nodal Arrays, DAS, Reflection Seismics, and Gravity Data

G. Sgattoni[1], G. Alessandrini[1], C. Morelli[2], G. Cultrera[1], G. Di Giulio[1], D. Famiani[1], S. Maraio[1], F. Muccini[1], N. Piana Agostinetti[3], G. Tarabusi[1], M. Vassallo[1]

1 Istituto Nazionale di Geofisica e Vulcanologia (Italy)
2 Ufficio Geologia e Prove Materiali, Provincia Autonoma di Bolzano, Cardano, Italy
3 Department of Environmental and Earth Sciences, University of Milano-Bicocca, Milan, Italy

This study presents an integrated geophysical investigation of the Venosta Valley (Italy), an Alpine valley in the Eastern Alps. The research focuses on a ~20 km long valley segment between Lake Resia and Lasa and aims to image the subsurface through a combination of seismic and gravimetric methods.

The study integrates multiple geophysical datasets collected along a total of 19 profiles, mostly oriented transverse to the valley axis. These include seismic data acquired with nodal arrays, gravimetric measurements, seismic reflection profiles, and a Distributed Acoustic Sensing (DAS) line. A unique opportunity for data acquisition was provided by the partial drainage of Lake Resia in May 2024, during which seismic and gravimetric surveys were conducted on the exposed lake floor. Additional field campaigns were carried out in 2025 across other sectors of the Venosta Valley. These included a dedicated profile where nodal array recordings, DAS measurements, and seismic reflection data were acquired simultaneously, complemented by previously collected gravimetric data.

The integrated interpretation of seismic and gravimetric observations allows for a multi-scale characterization of the subsurface, improving constraints on bedrock morphology and sedimentary infill architecture. In addition, we aim to investigate the dynamic behavior and seismic response of this Alpine valley through the mapping of resonance frequencies and the analysis of seismic wave propagation using array-based measurements.

Seismic nodal data are analyzed using both single-station techniques to identify resonance frequencies and array-based methods to investigate wavefield propagation and derive Vs profiles. These are integrated with gravity anomaly analysis to build a subsurface geological model constrained by seismic reflection profiles.

This study highlights the benefits of integrating different geophysical methods and provides an opportunity for their joint application and comparison within a single geological setting.

The research is carried out within a cooperation agreement between the Istituto Nazionale di Geofisica e Vulcanologia (INGV) and the Geological Survey of the Autonomous Province of Bolzano.

Corresponding author: giulia.sgattoni@ingv.it

Seismic and electrical monitoring of an earthen dam: first results from Fourcare test site (NW Italy)

V. Strallo[1], C. Colombero[1], A. Godio[1]

[1] *Politecnico di Torino, Department of Environmental, Land and Infrastructure Engineering (DIATI), Italy*

Introduction

Earthen dams, embankments and levees are often constructed in alpine regions for water storage, flood management and power generation. The dams could be subjected to incidents and failures due to overtopping, seepage, internal erosion, showing their vulnerability to aging and degradation processes (Chongxun et al., 2008; Talukdar & Dey, 2019). Earthen embankments located in alpine regions, are also exposed to freezing-thawing cycles and environmentally-linked natural hazards which can further affect their mechanical properties, emphasizing the need of continuous monitoring and assessments of long-term stability (Jabbarzadeh & Mousavi, 2025; Papathoma-Köhle et al., 2011).

Traditional monitoring techniques (e.g. monitoring of the piezometric level within the dam) are often invasive and offer only spatially limited information. For this purpose, integrating geophysical monitoring can provide a comprehensive image of subsurface conditions and allow the early detection of internal erosion processes. Electrical Resistivity Tomography (ERT) is a well-established technique to estimate preferential seepage pathways in earthen embankments (e.g., Camarero et al., 2017; Moreira et al., 2022; Oh, 2012; Panthulu et al., 2001), while ERT time-lapse can be used to monitor temporal variations in saturation under changing environmental conditions and to track the evolution of preferential flow pathways.

Previous studies have proven passive seismic monitoring effective in estimating shear-wave velocity and stiffness modifications of earthen dams caused by internal erosion, showing its potential to identify critical geotechnical conditions that may require intervention (e.g., Aguiar & Maciel, 2022; Planes et al., 2015).

In this study, we integrate both ERT and passive seismic monitoring to estimate temporal hydraulic and mechanical modifications in an earthen dam in northern Italy. Particularly, we have installed a network of seismic 3-component stations and an array of electrodes for the monitoring of geophysical parameters of the dams; the monitoring activity lasted for 8 months, in order to investigate the dam response to different environmental conditions.

Test site

The selected test site is the Fourcare dam located in Aosta Valley (Northwestern Italy, Fig. 1) at an elevation of 2325 m. Commissioned by Monterosa S.p.A, it was constructed as a water basin for the production of artificial snow for the nearby ski facilities. The reservoir is fed by the nearby Fourcare stream and, with a maximum depth of approximately 12.5 m, it can store around 127,000 m^3 of water. The embankment slopes are composed of mechanically compacted coarse-grained material and, to prevent water infiltration, an impermeable layer was installed between the dam body and the reservoir.

Seven inclinometers and four piezometers are installed along the embankment perimeter. Piezometer reveal a heterogeneous water table suggesting non uniform seepage conditions, whereas inclinometer measurements indicate localized deformations of the embankment. Furthermore, from local inspections, water seepage has been observed along the southern side of the embankment, while a naturally formed pond on the northwestern side could indicate a potential connection to the reservoir, although this has not been confirmed.

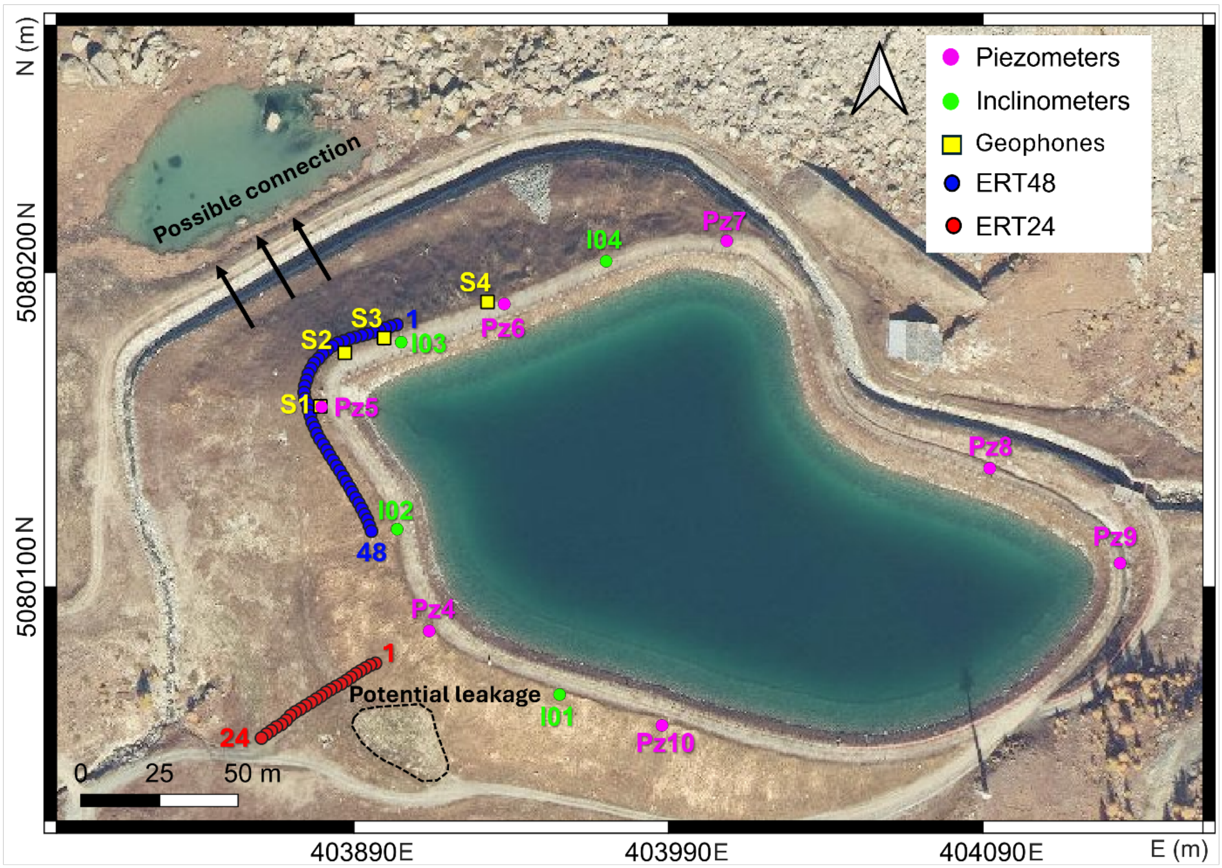

Fig. 1 - Test site showing the location of seismic geophones and electrical lines, together with the installed piezometers and inclinometers. Potential leakage zones are reported in black.

The array for the ERT monitoring were located along two main profiles (ERT48, ERT24 in figure 1), disposed on the north-western and southern sides of the embankment; the main target of the ERT time lapse measurements were to relate the temporal changes of electrical resistivity with the variations of the water content, close to two critical areas of the dams. Four 3C geophones (S1-4) were located along the Northen side of the dam, partially overlapped to ERT48, with S4 deployed in an area not covered by it.

Methods

Two ERT lines (ERT48 and ERT24), installed in October 2023, have been acquiring daily subsurface resistivity measurements until April 2024 through a Syscal Pro (IRIS Instruments) resistivity meter. ERT48, consisting of 48 electrodes at 2-m spacing, was positioned at the corner of the northern and western sides of the dam crest, to monitor a possible connection with the naturally formed pond highlighted in Fig. 1. ERT24, with 24 electrodes and the same spacing, was installed along the southern slope, close to the identified potential leakage area (black dashed line in Fig.1). To achieve both adequate lateral and vertical resolution of resistivity variations, data were acquired along both profiles using Wenner-Schlumberger and Dipole-Dipole array configuration, with automatic sequences. The time lapse inversion of the 2D pseudo-sections was performed using ResiPy (Blanchy et al., 2020). To better visualize saturation modifications over time, daily resistivity changes were computed as in percentage differences relative to the first reference acquisition.

Four geophones (S1 to S4) were installed at the north-western side of the reservoir and have been acquiring continuous passive seismic data until the first months of 2025. Each station includes a 2 Hz triaxial high-sensitivity geophone (200 V/(m/s)) and an on-purpose designed digitizer/recorder (GEA–GPS, developed by PASI s.r.l. and Iridium Italia s.a.s.) ensuring continuous seismic noise recording at 250 Hz sampling rate and daily remote information about the system state of health by a GSM–GPRS module. Synchronization between the different stations is provided by GPS timing. Data are stored in 1 h files in an internal 32 GB memory card. Spectral analysis of the continuous recordings was carried out to identify the embankment’s natural frequency. For this purpose, we computed single-station spectral ratios applying standardized filtering, windowing and smoothing procedure reported in literature (Colombero et al., 2018).

Results

Figure 2 (a to c) shows the electrical resistivity section measured along ERT24, using Wenner-Schlumberger configuration, on October 30, 2023, January 30, and March 30, 2024, respectively. A progressive enlargement of a high-resistivity zone at the beginning of the profile, can be observed over time, extending over the first 15 m of the profile on March 30, 2024. This trend may be also observed from Figure 2d and e, indicating the freezing of saturated soil during winter period. Between January and March, at approximately 20 m along the profile, a sudden decrease in resistivity is observed, possibly indicating presence of melting water.

A strong and continuous amplification of the signal can be observed at 10 Hz, indicating this value as the resonance frequency of the dam body. This can be observed in Figure 3a, dealing with the single station spectral ratios computed for station S4. This hypothesis was further confirmed by 3D numerical modelling of the dam eigenfrequencies performed in COMSOL Multiphysics. Despite temperature and precipitation fluctuations (Fig. 2b), the peak frequency remains quite constant, suggesting that the overall structural stiffness is stable and not significantly influenced by seasonal freezing–thawing cycles. A delayed and weak response to air temperature modifications is depicted at the daily and seasonal scales. However, during transitional seasons (mid-September, late October 2023 and late Aprile, 2024) some local fluctuations can be observed, possibly indicating local instabilities related to water seepage.

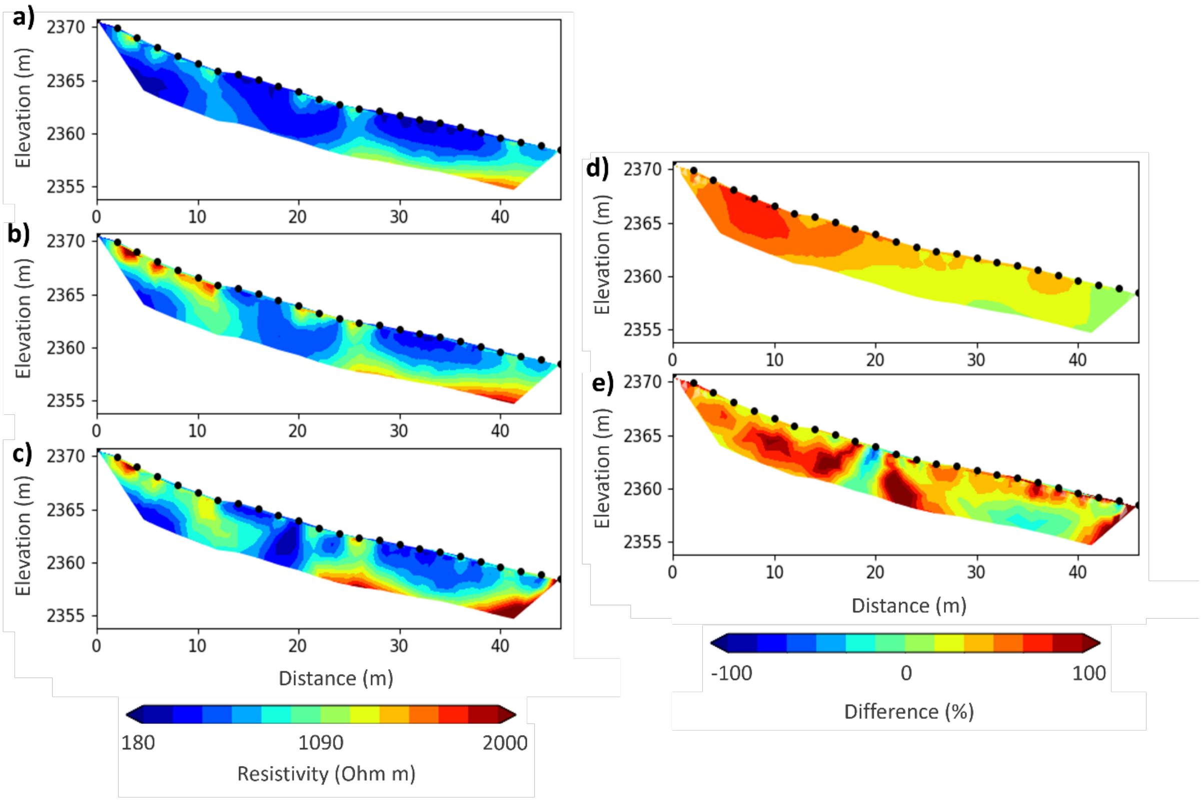

Fig. 2 - Time-lapse ERT24, obtained using Wenner-Schlumberger arrays, for three acquisition dates spanning approximately five months: (a) October 30, 2023; (b) January 30, 2024; (c) March 30, 2024. Panels (d) and (e) show the percentage resistivity differences relative to October 30, 2023, for January 30, and March 30, 2024, respectively.

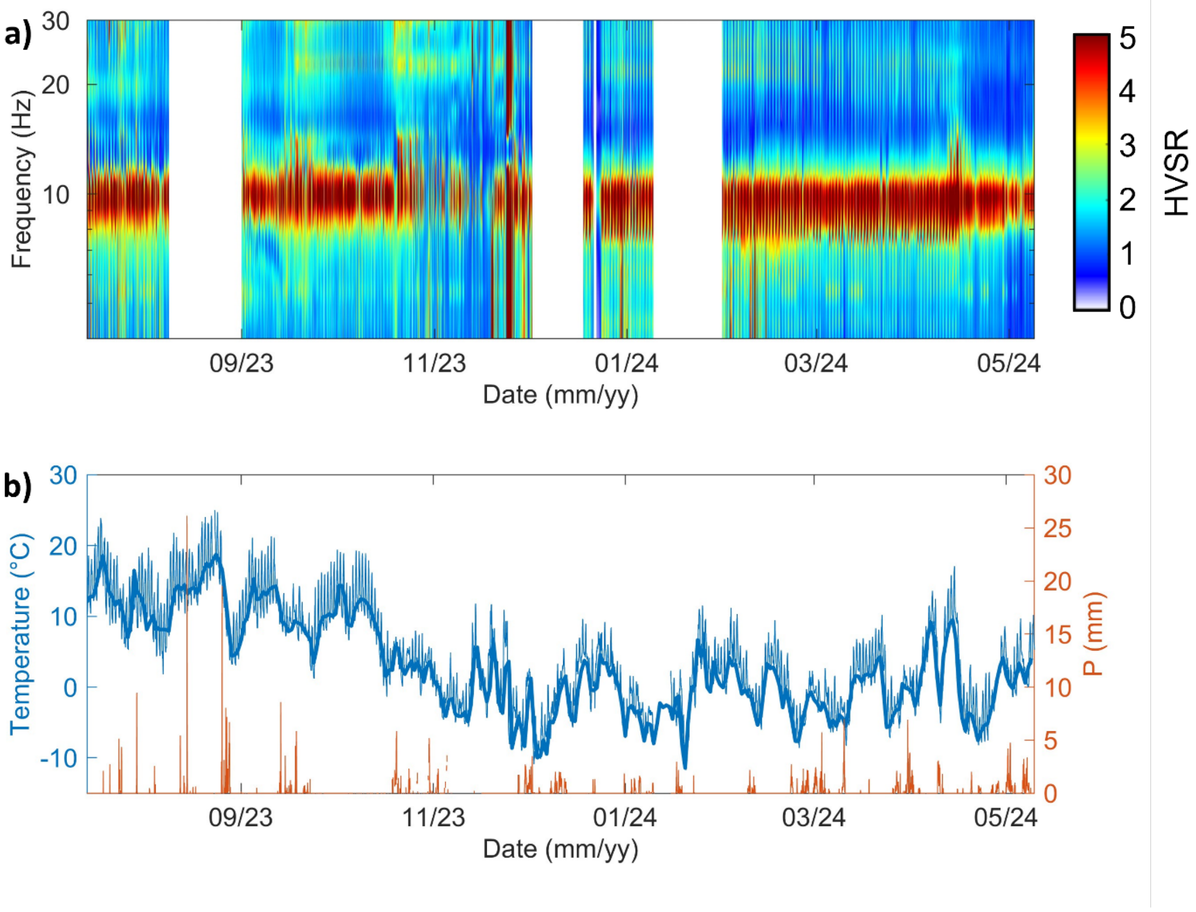

Fig. 3 - (a) Horizontal to Vertical Spectral Ratio (HVSR) measured at S4 from August 2023 to May 2023. White bands refer to periods with no data. (b) Temperature and precipitation acquired at the nearest weather station.

Conclusions

We monitored the hydraulic and mechanical behaviour of the Fourcare earthen dam in the Aosta Valley using an integrated geophysical approach combining ERT time-lapse and passive seismic monitoring. ERT time-lapse revealed temporal variations in soil saturation, with high resistivity zones forming during winter, indicating soil freezing and sudden resistivity drops in late winter/early spring, likely associated with melting water. Passive seismic monitoring allowed for the estimation of the resonance frequency of the dam, measured at 10-Hz. The peak frequency showed no strong dependency on environmental fluctuations, suggesting that the overall structural stiffness of the embankment is not significantly affected by freezing–thawing cycles. Local fluctuations in resonance frequency, were detected during transitional seasons, potentially indicating areas of localized instability related to water seepage.

Acknowledgments

The authors would like to thank Diego Franco and Andrea Vergnano for their valuable support in data acquisition. The research activities of this paper were funded by the NODES project, which has received funding from the MUR-M4C2 1.5 of PNRR funded by the European Union - NextGenerationEU (grant agreement no. ECS00000036).

References

Aguiar, G., & Maciel, S.; 2022: Earthen dam monitoring using passive seismic: A forward modeling study. *Brazilian Journal of Geophysics*, *40*. https://doi.org/10.22564/brjg.v40i2.2152

Blanchy, G., Saneiyan, S., Boyd, J., McLachlan, P., & Binley, A.; 2020: ResIPy, an intuitive open source software for complex geoelectrical inversion/modeling. *Computers & Geosciences*, *137*, 104423. https://doi.org/10.1016/j.cageo.2020.104423

Camarero, P. L., Moreira, C. A., Universidade Estadual Paulista, Brazil, & Universidade Estadual Paulista, Brazil.; 2017: Geophysical investigation of earth dam using the electrical tomography resistivity technique. *REM - International Engineering Journal*, *70*(1), 47–52. https://doi.org/10.1590/0370-44672016700099

Chongxun, M., Fanggui, L., Mei, Y., Rongyong, M., & Guikai, S.; 2008: Risk analysis for earth dam overtopping. *Water Science and Engineering*, *1*(2), 76–87. https://doi.org/10.3882/j.issn.1674-2370.2008.02.008

Colombero, C., Baillet, L., Comina, C., Jongmans, D., Larose, E., Valentin, J., & Vinciguerra, S.; 2018: Integration of ambient seismic noise monitoring, displacement and meteorological measurements to infer the temperature-controlled long-term evolution of a complex prone-to-fall cliff. *Geophysical Journal International*, *213*(3), 1876–1897. https://doi.org/10.1093/gji/ggy090

Jabbarzadeh, M., & Mousavi, Z.; 2025: Coupled multi-physics modeling of spatio-temporal behavior of embankment subjected to freeze-thaw cycles considering layered construction phases. *Cold Regions Science and Technology*, *240*, 104652. https://doi.org/10.1016/j.coldregions.2025.104652

Moreira, C. A., Guireli Netto, L., Camarero, P. L., Bertuluci, F. B., Hartwig, M. E., & Domingos, R.; 2022: Application of electrical resistivity tomography (ERT) in uranium mining earth dam. *Journal of Geophysics and Engineering*, *19*(6), 1265–1279. https://doi.org/10.1093/jge/gxac082

Oh, S.; 2012: Safety assessment of dams by analysis of the electrical properties of the embankment material. *Engineering Geology*, *129–130*, 76–90. https://doi.org/10.1016/j.enggeo.2012.01.016

Panthulu, T. V., Krishnaiah, C., & Shirke, J. M.; 2001: Detection of seepage paths in earth dams using self-potential and electrical resistivity methods. *Engineering Geology*, *59*(3), 281–295. https://doi.org/10.1016/S0013-7952(00)00082-X

Papathoma-Köhle, M., Kappes, M., Keiler, M., & Glade, T.; 2011: Physical vulnerability assessment for alpine hazards: State of the art and future needs. *Natural Hazards*, *58*(2), 645–680. https://doi.org/10.1007/s11069-010-9632-4

Planes, T., Mooney, M., Rittgers, J., Parekh, M., Behm, M., & Snieder, R.; 2015: Time-lapse monitoring of internal erosion in earthen dams and levees using ambient seismic noise. *Géotechnique*, *66*, 301–312. https://doi.org/10.1680/jgeot.14.P.268

Talukdar, P., & Dey, A.; 2019: Hydraulic Failures of Earthen Dams and Embankments. *Innovative Infrastructure Solutions*, *4*. https://doi.org/10.1007/s41062-019-0229-9

Corresponding author: valeria.strallo@polito.it

TRACKING COHERENT SEISMIC WAVEFIELD FEATURES IN ACTIVE-SOURCE DAS DATA BY 2-D NORMALIZED CROSS-CORRELATION

L. Suranna[1], N. Piana Agostinetti[1]

[1] *Department of Earth and Environmental Sciences, University of Milan-Bicocca, Milan, Italy*

Distributed Acoustic Sensing (DAS) has become an increasingly important tool in active-source and near-surface seismology, thanks to its ability to provide dense spatial sampling of the seismic wavefield along fiber-optic cables. Despite these advantages, the identification and tracking of coherent seismic features across multiple DAS shot records remain challenging due to strong amplitude variability, spatially variable coupling, and differences in source radiation and energy partitioning. Robust and objective methods for following the same physical wavefield feature across different shots are therefore essential for systematic analysis of DAS datasets.

In this study, we present an automated and fully reproducible workflow for tracking coherent seismic wavefield features across multiple DAS shot records using two-dimensional zero-mean normalized cross-correlation (ZNCC). The proposed approach is designed to identify and follow the same physical seismic feature, such as a refracted or reflected arrival, across a sequence of active-source DAS records, while minimizing the effects of amplitude scaling, baseline offsets, and background noise that are intrinsic to DAS measurements.

The workflow is applied to data acquired during a seismic field campaign conducted in September 2024 in the Budoia-Aviano area (Friuli Venezia Giulia, NE Italy), within the framework of near-surface investigations of active and capable fault systems. In this contribution, we focus on a subset of five representative DAS shots selected from the full dataset to demonstrate and validate the proposed feature-tracking methodology.

The DAS data consist of strain-rate measurements acquired along a linear fiber-optic cable with a gauge length of 4.0 m and a channel spacing of 1.0 m, resulting in 221 effective channels and an active aperture of approximately 221 m. Each shot record has a duration of approximately 10 s and is stored as a two-dimensional array of 10,909 temporal samples by 221 spatial channels, with data type float32. The measured physical quantity is strain rate (s^{-1}), which is particularly sensitive to near-surface seismic wavefields. The effective sampling frequency, estimated directly from the data, is approximately 1091 Hz, while the nominal acquisition BlockRate is 1000 Hz; the small discrepancy is attributed to buffering and concatenation of acquisition blocks (Fig. 1). Although the total available fiber length is about 1250 m, only a subset corresponding to the active seismic line is used in this analysis.

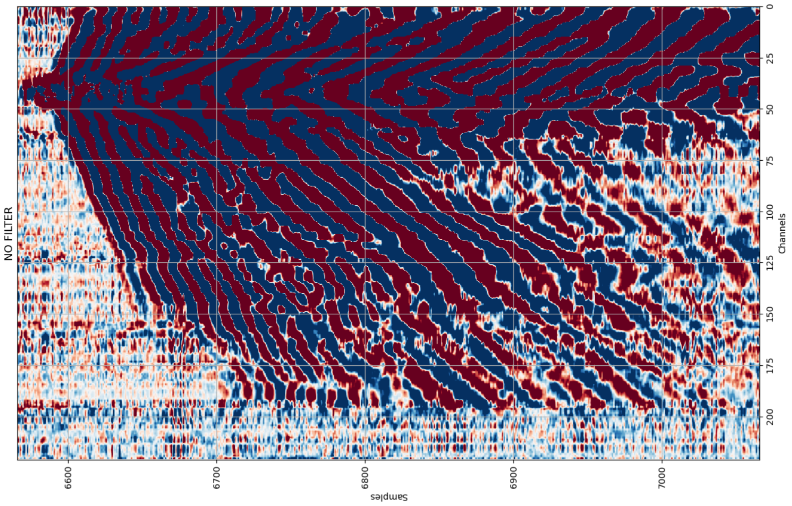

Fig. 1: Example of an unfiltered DAS shot record displayed as strain-rate versus time and channel number, highlighting a coherent seismic wavefield characterized by strong amplitude variability and spatially continuous arrivals.

The workflow operates on DAS shot records organized in a consistent (samples × channels) format, which is used throughout all processing steps, including windowing, correlation, and visualization. For each shot, a rectangular time-channel search window is defined a priori based on expected arrival times and spatial extent of the target feature. These shot-specific search windows represent physically motivated constraints that significantly reduce computational cost and limit the risk of false matches outside the region of interest.

A two-dimensional template representing the seismic feature of interest is extracted from a reference shot. The template is selected from the central portion of the reference search window and defined with fixed dimensions in both time and channel space, ensuring compatibility with all subsequent search windows. Feature matching is performed by sliding the template over each search window and computing the ZNCC coefficient at every possible position. By removing the mean and normalizing by the standard deviation of both the template and the search sub-window, ZNCC provides a similarity measure that is robust to amplitude scaling and offset differences, which are common in DAS recordings due to variable coupling and source conditions.

Tracking is performed sequentially across shots following their acquisition order. Two alternative strategies are implemented: a fixed-template approach, in which the original template extracted from the reference shot is used throughout the sequence, and an adaptive-template approach, in which the template is updated at each step using the best-matching patch from the previous shot. The adaptive strategy allows gradual evolution of the tracked feature while preserving continuity across shots, and is particularly suitable when the wavefield varies smoothly with source position.

For each shot, the algorithm automatically identifies the location that maximizes the ZNCC score and stores the corresponding temporal and spatial bounds, correlation value, search window limits, and relative offsets within the window. All tracking results are compiled into a structured tabular dataset and exported in CSV format, enabling straightforward reuse for further quantitative analysis and visualization. Visual quality-control plots are generated for each shot, showing the search window and the detected feature overlaid, providing an essential qualitative check on tracking consistency and physical coherence (Fig. 2).

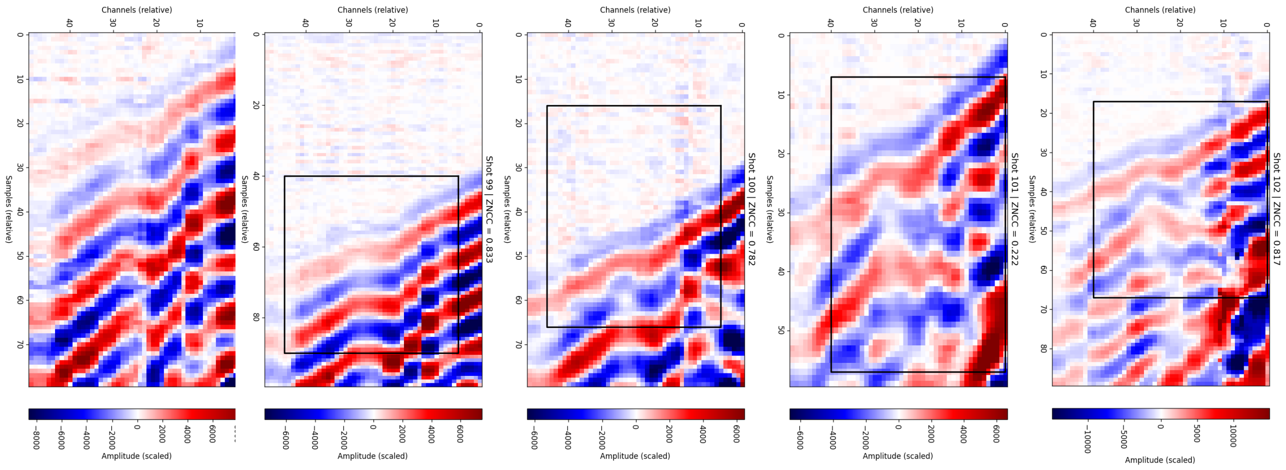

Fig. 2: Automated tracking of a coherent seismic wavefield feature across five representative DAS shot records. For each shot, the time–channel search window is shown together with the best-matching template location identified by 2-D zero-mean normalized cross-correlation (ZNCC). The tracked feature exhibits consistent spatial and temporal continuity despite strong amplitude variability between shots

The entire workflow is implemented in Python within a reproducible Jupyter notebook and requires no manual intervention once the input data, search windows, and template dimensions are defined. The methodology is general and can be readily extended to larger DAS datasets, different acquisition geometries, or alternative seismic applications.

Future developments will focus on the integration of numerical wavefield modeling using SPECFEM2D to simulate DAS responses under controlled conditions. This will allow quantitative assessment of the tracking performance, investigation of waveform evolution with source–receiver geometry, and improved interpretation of tracked features in terms of subsurface structure and fault-related processes.

References

L. Suranna, N. Piana Agostinetti (2025), DAS Feature Tracking Across Multiple Shots (ZNCC-based) (unpublished Python Script)

Corresponding author: Lorenzo Suranna lorenzo.suranna@unimib.it – lsura24@gmail.com

Comparison and validation of Frequency Domain Electromagnetic Methods and Electrical Resistivity Tomography for Seawater Intrusion Mapping in Shallow Coastal Aquifers

B. Surian[1], E. Forte[1], L. Zini[1]

[1] *Department of Mathematics, Informatics and Geosciences, University of Trieste, Trieste, Italy*

1. Introduction

Coastal aquifers are increasingly affected by seawater intrusion, driven by groundwater overexploitation, reduced recharge, and climate-induced variations in sea level and salinity patterns (Mastrocicco & Colombani, 2021). Mapping the distribution of saline and fresh groundwater is therefore essential for the sustainable management of vulnerable coastal plains. Electrical Resistivity Tomography (ERT) is widely used for characterising saltwater intrusion, but its deployment is often restricted by long acquisition times and logistical constraints.

Electromagnetic induction techniques (EMI), particularly Frequency Domain Electromagnetics (FDEM), offer a rapid and contactless alternative that enables large-area surveying in significantly reduced acquisition times. However, questions remain about their depth sensitivity, robustness, and calibration requirements. Comparisons between multiple FDEM instruments and ERT are still limited, especially in shallow (i.e., a few meters deep) coastal systems, characterised by high heterogeneity, variable salinity levels, and a strong dependency on even smoothed topography.

This study presents a systematic comparison between ERT and two commercially available FDEM instruments, a multi-coil, single-frequency equipment (CMD Explorer, GF Instruments) and a multi-frequency equipment (GEM-2, Geophex), across four test sites located within the Grado Lagoon coastal plain (Friuli Venezia Giulia region, north-eastern Italy). The sites represent diverse geomorphological and hydrogeological conditions, ranging from reclaimed lowlands to a coastal dune system. The objective is to evaluate the reliability of FDEM for shallow salinity mapping, assess the consistency of qualitative and quantitative responses between the different methods, and identify the role of site-specific calibration in ensuring accurate quantitative bulk electrical conductivity estimates.

2. Study area

The Grado Lagoon comprises a low-lying coastal system formed by lagoonal, fluvial, and aeolian deposits (Marocco, 1995). Three of the investigated sites lie within reclaimed agricultural land that is often below sea level, while the fourth is located on a coastal dune ridge. The area experiences varying degrees of shallow aquifer salinisation, documented through vegetation stress, salt crusts, and limited existing hydrochemical data.

The four test sites (TS1-TS4) were selected to represent:

- a homogeneous saline phreatic aquifer during dry conditions (TS1),
- a comparable setting under high-recharge conditions (TS2),
- a palaeochannel environment with lateral heterogeneity (TS3),
- a coastal dune with strong topographic gradients, hosting very low salinity groundwater (TS4).

These contrasting contexts enable evaluation of instrument performance across a broad conductivity and hydrogeological range.

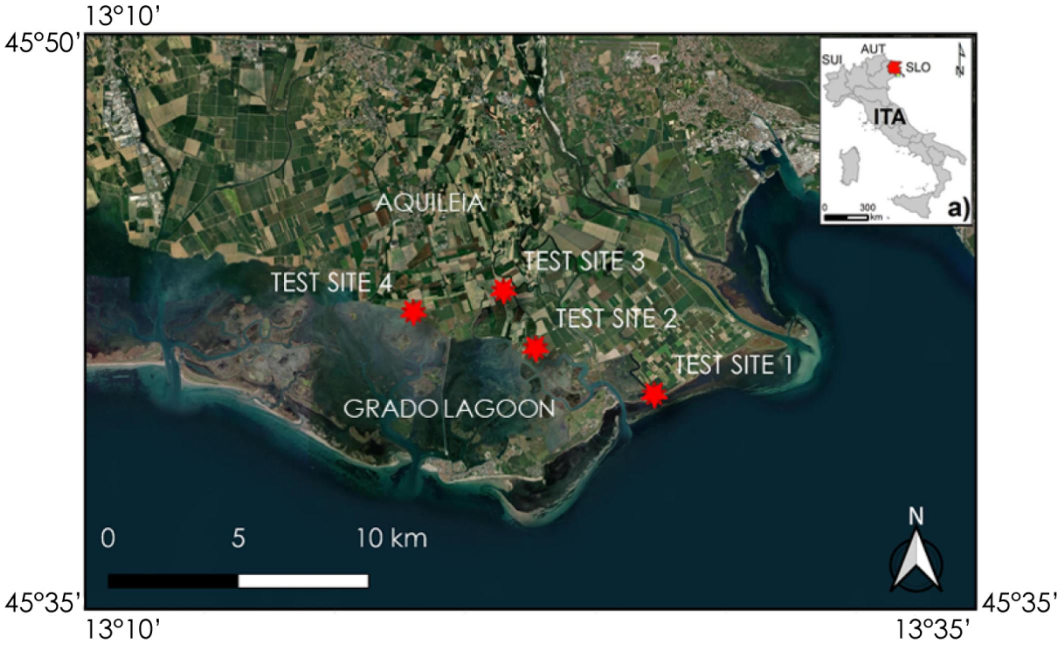

Fig. 1 - Location maps of the four test sites (red stars) close to the northern limit of the Grado Lagoon (NE Italy).

3. Methods

All surveys were carried out along coincident profiles, allowing direct comparison of apparent electrical conductivity (ECa).

FDEM surveying was performed using:

- CMD Explorer (single frequency at 10 kHz; three coil spacings; combined HCP and VCP modes);

- GEM-2 (multiple frequencies from ~2 to 93 kHz), enabling variable penetration depths but potentially affected by non-LIN (Low Induction Number) conditions, especially in highly conductive soils (Everett, 2012).

ERT surveying, performed for independent comparison, used a Wenner-Schlumberger configuration with 48 electrodes (2 m spacing). Only the upper 6-7 m were considered, matching the effective FDEM investigation depth.

Since ERT and FDEM sampling were not perfectly spatially coincident, a positional tolerance was applied to pair measurements. Cross-plots were generated for each site using ERT-derived ECa assumed as reference values. Linear regressions provided correction parameters (slope and intercept), which were then applied to normalise FDEM datasets. Coefficients of determination (R^2) and Spearman correlation coefficients (ρ) were also computed to evaluate respectively the strength of the linear correlation and the monotonic relationships between ERT and FDEM data, independently of absolute calibration (Paz et al., 2024; Blanchy et al., 2024).

In situ water conductivity was measured at TS2, TS3 and TS4 to support interpretation. Bulk conductivities were estimated using Archie's law (Archie, 1942) for unconsolidated sandy sediments, enabling a qualitative comparison with geophysical values.

4. Results and discussion

4.1 Cross-plot and regression analyses

Comparison across the four sites demonstrates that CMD Explorer consistently shows the strongest agreement with ERT, yielding R^2 values between 0.58 and 0.85 and Spearman coefficients up to 0.94. This indicates robust detection of spatial conductivity patterns even when absolute values differ.

GEM-2 presents greater variability, with R^2 as low as 0.48 at the dune site (TS4). This instrument often displays higher scatter, depth-dependent offsets, and occasional frequency-related anomalies requiring removal or correction before calibration. Still, its high Spearman coefficients (up to 0.86) indicate strong monotonic relationship and sensitivity to shallow features.

4.2 Representative comparison: Test Site 1

Fig. 2 presents a representative example from TS1, highlighting cross-plots and the three conductivity pseudo-sections derived from ERT, CMD Explorer, and GEM-2 after the above-described calibration.

Both FDEM instruments reproduce the main ERT structure:

a thin, low-conductivity unsaturated layer, an abrupt increase in ECa associated with a shallow saline phreatic aquifer, laterally homogeneous conditions reflecting lagoon fine-grained sediments.

CMD Explorer offers the closest quantitative match with ERT, whereas GEM-2 captures sharper near-surface variations but tends to underestimate the conductivity of deeper saline layers. Despite these differences, all datasets coherently delineate the shallow freshwater-saltwater transition and its local variations.

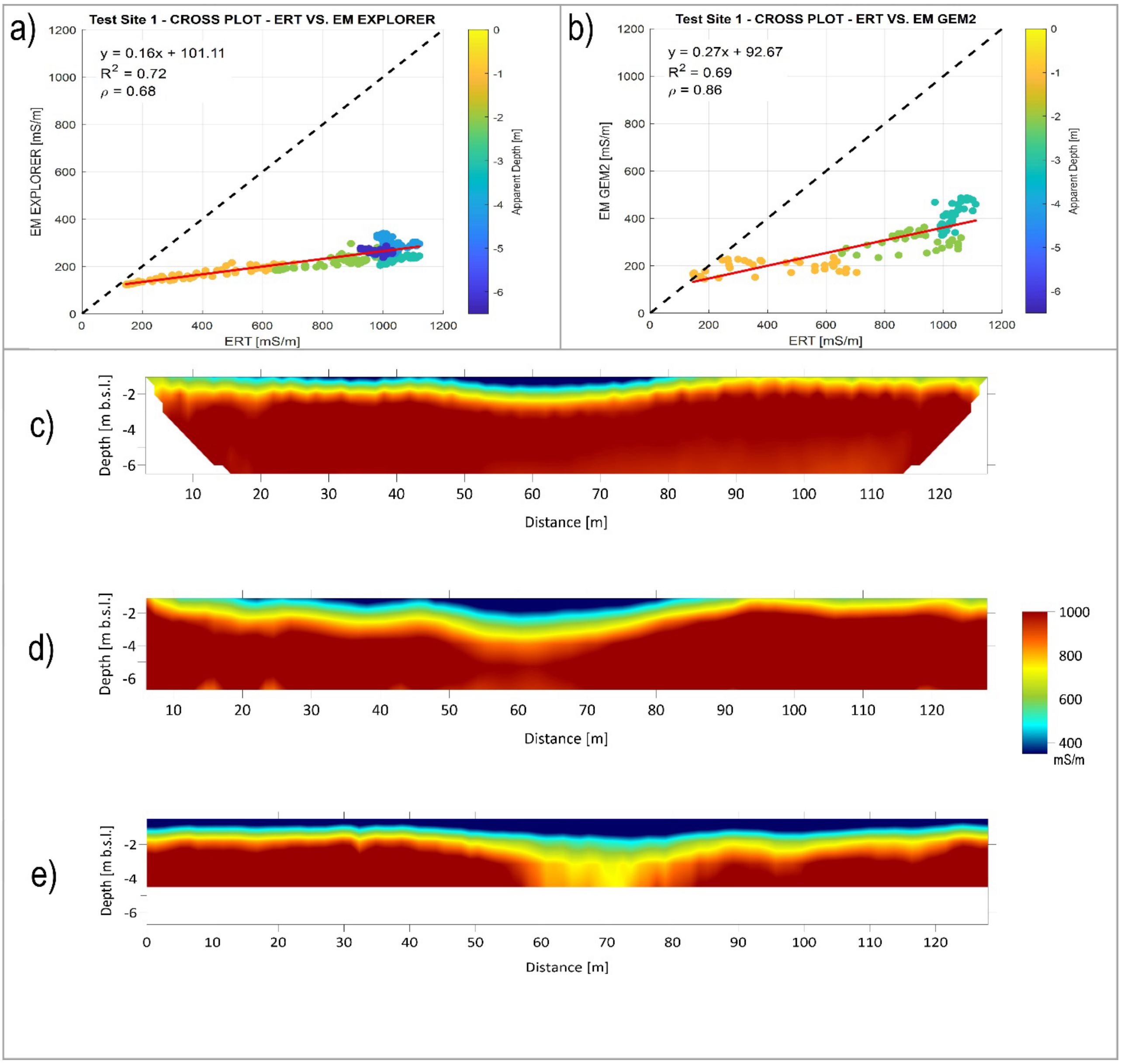

Fig. 2 - Representative results for Test Site 1. Crossplots of ERT vs Explorer and ERT vs GEM-2 (2a and 2b). 2c, 2d, 2e show the pseudo-depth ECa sections obtained with SyscalPro, Explorer and GEM-2, respectively after the FDEM data calibration. The scale ratio and the conductivity colour bar are the same for panels 2c, 2d and 2e.

4.3 Behaviour across contrasting hydrogeological settings

At TS2, high rainfall preceding acquisition led to decreased ECa values and increased spatial variability. Correlations remain moderate, confirming the need for site-specific calibration under seasonal recharge conditions.

At TS3, a palaeochannel characterised by lower salinity and coarser sediments was identified as a consistent low-conductivity zone in all data sets. FDEM areal mapping further clarified the geometry of this feature, while borehole water EC measurements confirmed reduced salinity within the channel.

At TS4, strong topographic gradients resulted in distortions within the ERT inversion, while the calibrated FDEM datasets better captured the shallow freshwater lens and the low-conductivity dune sand. GEM-2 proved particularly sensitive to the thin unsaturated layer, despite a higher noise level.

Across all sites, both FDEM instruments reproduced the conductivity distribution observed in ERT profiles. However, absolute values differed significantly without calibration, often by factors of 2-5 depending on soil salinity, frequency bandwidth, and depth sensitivity. Simple linear corrections derived from cross-plot regressions of galvanic (ERT) and inductive (EMI) measurements substantially reduced these discrepancies.

The study confirms that local calibration of FDEM data using ERT measurements is essential, particularly in shallow coastal environments where conductivity ranges are large and subsurface conditions can rapidly vary both in depth and in space. Once calibrated, FDEM surveys have demonstrated their strong potential for mapping salinity patterns quickly and reliably, even over large areas. This enables both 2-D extended transects and 3-D volumetric reconstructions (Fig. 3). In the example of Fig. 3, after applying the above-described calibration equations, the values obtained by the two FDEM devices are very similar. They highlight vertical variations mainly related to a shallow brackish aquifer, as well as spatial changes related to the man-made surface drainage network.

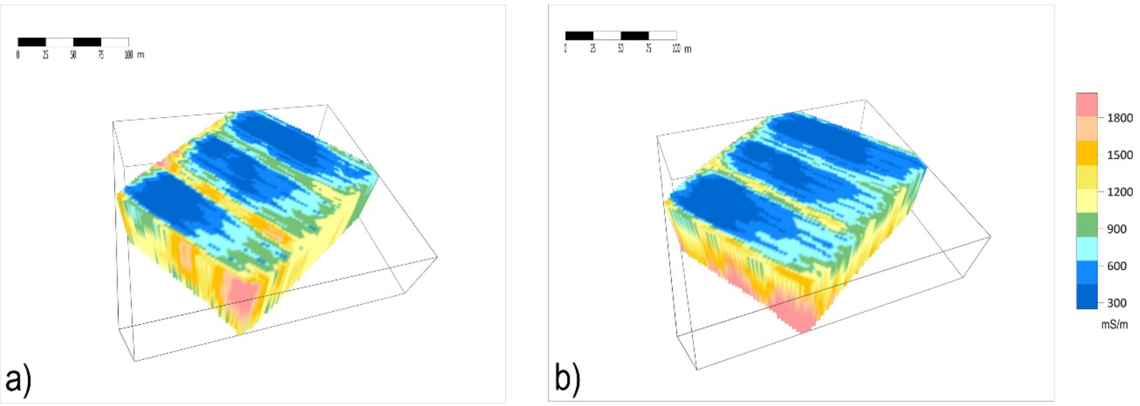

Fig. 3: Representative volume mapping of ECa at TS1. (a) CMD Explorer, (b) GEM-2. Data is normalised using the previously derived calibration equations.

Notably, extended FDEM surveys at TS1 and TS3 revealed regional-scale salinity gradients and channel-related heterogeneities consistent with the 2-D ERT profiles and the hydrogeological expectations. These results illustrate the scalability of FDEM, which offers rapid, contactless, and cost-efficient coverage compared to ERT surveys.

5. Conclusions

This study evaluates the performance of two FDEM instruments against ERT for mapping shallow salinity and lithological variations in shallow coastal aquifer systems. The main findings are:

- FDEM reliably detects the spatial patterns of salinity and lithology, but absolute ECa values differ and require calibration.
- CMD Explorer exhibits the most consistent correlation with ERT, while GEM-2 is more sensitive to shallow features but more prone to scatter.
- Cross-plot regression provides a simple, effective calibration approach, though it remains site- and season-dependent.
- Calibrated FDEM is suitable for large-scale 2-D and 3-D conductivity mapping, extending the interpretative value of limited ERT profiles.
- The combined use of ERT, FDEM and in situ measurements provides a robust framework for characterising seawater intrusion in shallow coastal aquifers.

Acknowledgements

This study was carried out within the PNRR research activities of the consortium iNEST (Interconnected North-Est Innovation Ecosystem) funded by the European Union Next-Generation EU (Piano Nazionale di Ripresa e Resilienza (PNRR) – Missione 4 Componente 2, Investimento 1.5 – D.D. 1058 23/06/2022, ECS_00000043).

The authors would like to thank the European Commission and the Water 4 All Partnership for funding in the frame of the collaborative international consortium RESCUE financed under the 2022 Joint call of the European Partnership 101060874 — Water4All

References

Archie GE (1942) The electrical resistivity log as an aid in determining some reservoir characteristics. Transactions of the AIME 146:54–62. https://doi.org/10.2118/942054-G.

Blanchy G, McLachlan P, Mary B, Censini M, Boaga J, Cassiani G (2024) Comparison of multi-coil and multi-frequency frequency domain electromagnetic induction instruments. Frontiers in Soil Science 4:1239497. https://doi.org/10.3389/fsoil.2024.1239497.

Everett ME (2012) Theoretical developments in electromagnetic induction geophysics with selected applications in the near surface. Surveys in Geophysics 33:29–63. https://doi.org/10.1007/s10712-011-9138-y.

Marocco R (1995) Sediment distribution and dispersal in northern Adriatic lagoons (Marano and Grado paralic system). Giornale di Geologia 57:77–89

Mastrocicco M, Colombani N (2021) The issue of groundwater salinization in coastal areas of the Mediterranean region: A review. Water 13:90. https://doi.org/10.3390/w13010090.

Paz MC, Castanheira NL, Paz AM, Gonçalves MC, Monteiro Santos F, Farzamian M (2024) Comparison of electromagnetic induction and electrical resistivity tomography in assessing soil salinity: Insights from four plots with distinct soil salinity levels. Land 13:295. https://doi.org/10.3390/land13030295.

Corresponding author: benedetta.surian@phd.units.it

Temporal Changes in Soil Elastic Parameters $\left(\frac{\Delta V}{V}, \Delta f_0\right)$ and their Interdependence

B. Tiboni [1], **S. Castellaro** [1]

[1] *Dipartimento di Fisica e Astronomia, Alma Mater Studiorum Università di Bologna, v.le C. B. Pichat 8, 40127 Bologna (Italy)*

Over the past few years, geodetic techniques such as GPS and InSAR have revealed vertical ground motions on daily and seasonal timescales. Similar variations are also observed in seismic data, which reflect changes in the elastic properties of the ground, including the resonance frequency. Seismic observations provide a valuable complement to geodetic measurements: they are passive, offer three-component recordings, are less sensitive to atmospheric errors, and potentially allow the analysis of much longer time series.

In this context, over the past two decades single-station ambient-noise measurements have become a widely used and effective tool for investigating the dynamic behavior of the ground, particularly for identifying the resonance frequency, a key parameter linked to the elastic properties of the subsurface. Recent studies have shown that this frequency is not constant over time, but can vary on a seasonal scale, as observed by Lattanzi et al. (2023) for the resonance frequency (f_0) and by Vassallo et al. (2022) for the H/V spectral ratio. Other authors (e.g., Mao et al., 2022) have investigated the same phenomenon from the perspective of relative changes in seismic wave propagation velocity (ΔV/V), using cross-correlation of seismic signals recorded by a dense network of stations. Since seismic velocity is directly related to the elastic moduli and therefore to ground stiffness, a direct relationship is expected between ΔV/V and variations in the resonance frequency f_0. However, this relationship has not yet been analyzed in detail. It is also important to note that temporal variations in f_0 may reflect not only changes in stiffness, but also variations in material mass or in the system's boundary conditions.

The original goal of this study was therefore to analyze the relationship between temporal variations in ΔV/V and f_0, and to assess whether the former alone can account for the amplitude of the latter. To this end, we first examined the same dataset used by Mao et al. (2022), focusing on seismic stations in the Los Angeles Basin. At five representative broadband stations, we analyzed both the frequency variations of the H/V peaks and the frequency shifts of individual spectral features. The dataset also includes a broadband station in Switzerland, previously analyzed by Lattanzi et al. (2023), which represents a well-documented 2D case study and provides a useful term of comparison with the sites in the Los Angeles Basin.

As is well known, under 1D conditions the H/V peak typically corresponds to a minimum in the vertical spectral component, while the horizontal spectral components may or may not display peaks at the same frequency (Castellaro, 2016; Castellaro and Musinu, 2022). The minimum in the vertical spectrum is related to Rayleigh-wave behavior (Bard and Bouchon, 1985; Tuan et al., 2011), whereas maxima in the horizontal components are generally associated with S-wave resonances or contributions from Love waves. In 2D settings, however, the H/V peak is usually linked to S-wave resonances that appear as clear peaks in the horizontal spectral components (Castellaro and Musinu, 2022).

Our results confirmed that both the resonance frequencies f_0 and the H/V peaks exhibit seasonal and even diurnal variations. Particularly noteworthy is the relationship between the resonance frequencies and the peaks of the H/V spectral ratio.

In the Los Angeles Basin, all observed H/V peaks were consistent with the 1D case: the H/V peak was fully correlated with the minimum in the vertical spectral component and fully anticorrelated with the peaks in the horizontal spectral components within the same frequency range. When a vertical P-wave resonance was observable (typically at about twice the horizontal resonance frequency), it was found to be strongly correlated with the horizontal spectral peaks. These observations confirm that, under 1D conditions, H/V peaks reflect minima in the vertical spectral components and are therefore related to surface-wave behavior. Interestingly, their frequency variation is anticorrelated with that of body-wave resonances.

In the 2D cases, represented by the Swiss station analyzed by Lattanzi et al. (2023), the spectral peaks are instead clearly associated with S-wave resonances. In this context, the H/V peaks and the S-wave resonances were found to be positively correlated, confirming that under 2D conditions the H/V ratio is indeed associated with body-wave resonances, as expected.

No uniform trend emerged regarding the seasonal behavior of the resonance frequencies. In the 2D Alpine basins, frequencies tend to increase in summer (Northern Hemisphere), whereas in the 1D cases of the Los Angeles Basin the trend is different. This suggests that the physical mechanisms underlying the two phenomena are unlikely to be the same.

Another unresolved issue concerns the behavior of the vertical component of Rayleigh waves, which appears to be systematically anticorrelated with the resonance frequencies of body waves. Ultimately, the observed frequency variations are significantly larger than what would be expected based solely on $\Delta V/V$ changes. Without addressing the additional complexity introduced by diurnal variations, the results indicate that several contributing factors, often simplistically attributed to variations in subsurface fluid content, play a role in the observed resonance-frequency variations, suggesting that the responsible mechanisms extend beyond a simple hydrological control.

References

Bard, P.-Y., & Bouchon, M. (1985). The two-dimensional resonance of sediment-filled valleys. *Bulletin of the Seismological Society of America*, *75*(2), 519–541. https://doi.org/10.1785/BSSA0750020519.

Castellaro, S. (2016). The complementarity of H/V and dispersion curves. *Geophysics*, *81*(6), T323–T338. https://doi.org/10.1190/geo2015-0399.1

Castellaro, S., & Musinu, G. (2022). Resonance versus Shape of Sedimentary Basins. *Bulletin of the Seismological Society of America*, *113*(2), 745–761. https://doi.org/10.1785/0120210277

Lattanzi, G., Castellaro, S., & Di Donato, M. (2023). On the time-stability of resonance frequencies in deep basins. Geophysical Journal International, 234(3), 1870–1884. https://doi.org/10.1093/gji/ggad172.

Mao, S., Lecointre, A., Van Der Hilst, R. D., & Campillo, M. (2022). Space-time monitoring of groundwater fluctuations with passive seismic interferometry. *Nature Communications*, *13*(1), 4643. https://doi.org/10.1038/s41467-022-32194-3.

Tuan, T. T., Scherbaum, F., & Malischewsky, P. G. (2011). On the relationship of peaks and troughs of the ellipticity (H/V) of Rayleigh waves and the transmission response of single layer over half-space models: Relationship of peaks and troughs of H/V-ratio. *Geophysical Journal International*, *184*(2), 793–800. https://doi.org/10.1111/j.1365-246X.2010.04863.

Vassallo, M., Cultrera, G., Di Giulio, G., Cara, F., & Milana, G. (2022). Peak Frequency Changes From HV Spectral Ratios in Central Italy: Effects of Strong Motions and Seasonality Over 12 Years of Observations. *Journal of Geophysical Research: Solid Earth*, *127*(5), e2021JB023848. https://doi.org/10.1029/2021JB023848.

Corresponding author: Beatrice.tiboni2@unibo.it

Acceptability Criteria for Microtremor H/V Curves: Traditional and AI-Based Approaches.

B. Tiboni [1], **S. Castellaro** [1]

[1] *Dipartimento di Fisica e Astronomia, Alma Mater Studiorum Università di Bologna, v.le C. B. Pichat 8, 40127 Bologna (Italy)*

The SESAME criteria (2004), established 22 years ago, consist of nine threshold-based rules aimed at evaluating: (i) the reliability of a microtremor H/V curve (three criteria) and (ii) the clarity of its peaks (six criteria). However, advances in the understanding of seismic wavefields and the phenomenology of H/V curves have rendered these criteria partially outdated (Molnar et al., 2022), highlighting the need for a revision. In particular, it remains an open question whether maintaining a threshold-based strategy is optimal, or if more flexible classification systems could better account for the wide variety of curve shapes and the underlying physical phenomena.

Artificial neural networks have proven particularly effective in classification problems that are straightforward for the human brain but challenging to formalize mathematically, such as pattern or image recognition. Recently, Castellaro and Dal Compare (2025) trained an artificial neural networks on thousands of H/V curve examples to classify different frequency intervals into categories such as “normal curve,” “1D characteristics,” “2D/3D characteristics,” “artifact,” “velocity inversion,” “curve requiring cleaning,” and “malfunctioning instrument.” The network assigns each interval to a category with a confidence interval, effectively substituting the six SESAME criteria related to peak clarity. However, an equivalent of the first three SESAME criteria, which define overall curve reliability, is still missing. This is particularly important because a single H/V curve may contain dozens of intervals classified into multiple categories, making a synthetic evaluation of curve quality necessary.

In this work, we focus on defining such reliability criteria. We employed an independent dataset comprising microtremor measurements from three geological and geographic contexts: the Boston metropolitan area (219 measurements; Yilar, 2017), the New England area (354 measurements; Pontrelli, 2023a), and California (489 measurements; Yong, 2013) (Fig. 1).

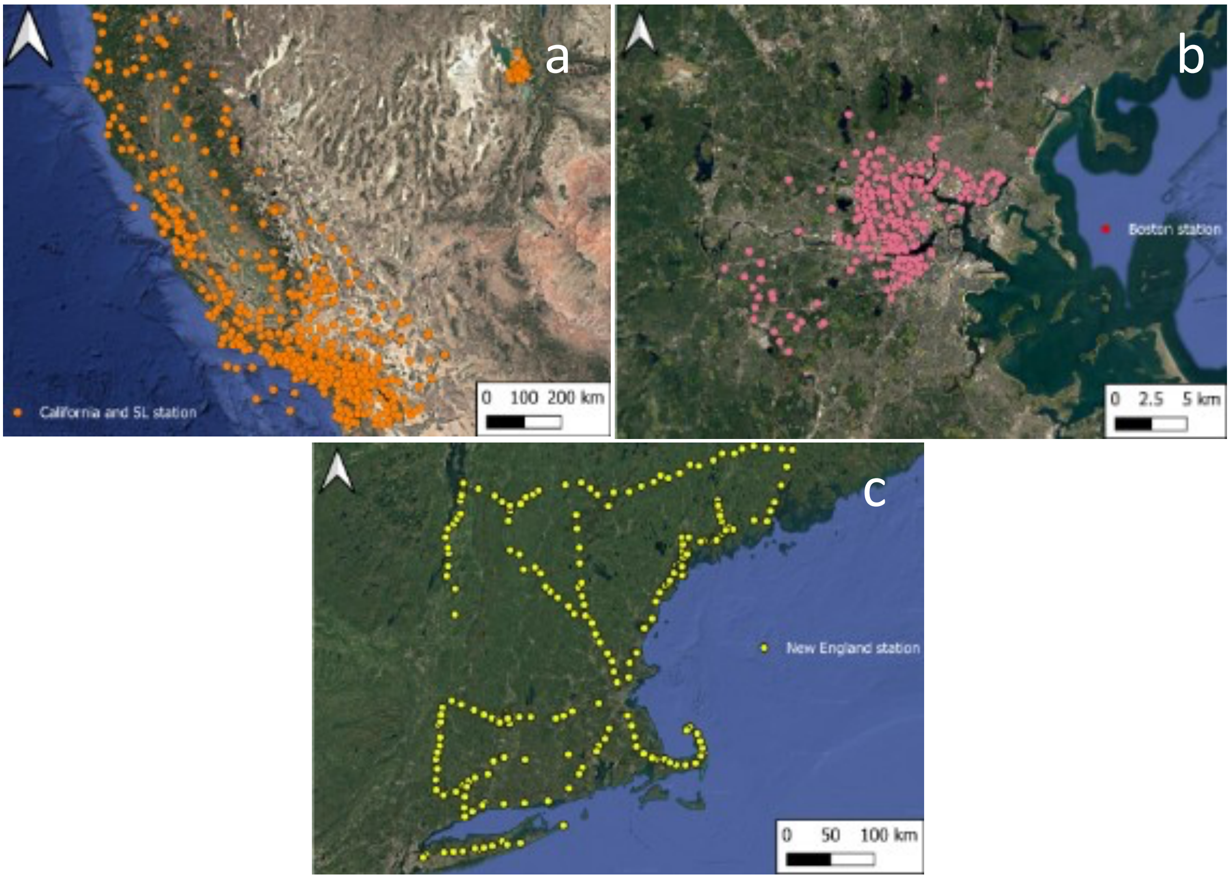

Fig. 1 – Distribution of microtremor measurements in the three datasets used: (a) California (489 measurements, Yong 2013); (b) Boston (219 measurements, Yilar 2017); (c) New England (354 measurements, Pontrelli 2023a). Points indicate the locations of the measurement stations.

The choice of this dataset is motivated by the fact that it is completely unknown to the network, as it was not used in any way during the training phase; moreover, it was acquired with different types of seismometers than those used for training and covers a wide range of geological settings, from exposed or shallow bedrock to deep sedimentary basins (bedrock at 100–200 m, covered by Quaternary deposits).

We first created and cleaned the H/V curves, then analyzed them according to the SESAME criteria and subsequently with the neural network. We compared expert assessments with SESAME and neural network classifications, analyzing divergences and convergences. From these results, we propose a set of operational rules, implementable in cascade with the neural network, to define the overall reliability of H/V curves, analogous to the first three SESAME criteria while leveraging the flexibility of neural networks.

References

Castellaro, S., and L. Dal Compare. "AI-Based Quality Check and Interpretation of H/V Curves." NSG 2025: 31st Meeting of Environmental and Engineering Geophysics. Vol. 2025. No. 1. European Association of Geoscientists & Engineers, 2025.

Molnar, S., A. Shirohey, J. Assaf, P.-Y. Bard, S. Castellaro, C. Cornou, B. Cox, B. Guiller, B. Hassani, H. Kawase, S. Matsushima, and F.J. Sánchez-Sesma, 2022, A review of the microtremor horizontal-to-vertical spectral ratio (MHVSR) method: Journal of Seismology, **26**, 653-685.

Pontrelli, M.A., Baise, L.G., Ebel, J.E. (2023a) Regional-Scale Site Characterization Mapping in High Impedance Environments Using Soil Fundamental Resonance (f0): New England, USA. Engineering Geology Volume 315. doi: https://doi.org/10.1016/j.enggeo.2023.107043

Yilar, E., Baise, L.G., Ebel, J.E. (2017) Using H/V measurements to determine depth to bedrock and Vs30 in Boston, Massachusetts. Engineering Geology 217, 12-22

Yong, A., Martin, A., Stokoe, K., and Diehl, J., 2013, ARRA-funded V_{S30} measurements using multi-technique approach at strong-motion stations in California and central-eastern United States: U.S. Geological Survey Open-File Report 2013–1102, 60 p. and data files, http://pubs.usgs.gov/of/2013/1102/.

Corresponding author: Beatrice.tiboni2@unibo.it

Towards the development and optimization of a geophysical sensors suite for the planetary exploration: the PRORIS and MARS-LAVA projects

Pietro Tizzani[1,2], Andrea Barone[1,2], Andrea Vitale[2], Filippo Accomando[2], Francesco Mercogliano[1,2,3], Raffaele Castaldo[1,2], Giuseppe Solaro[1,2], Susi Pepe[1,2], Ilaria Catapano[1], Ugo Cortesi[4], Roberto Orosei[5], Francesco Soldovieri[1]

[1] Istituto per il Rilevamento Elettromagnetico dell'Ambiente (IREA), Consiglio Nazionale delle Ricerche (CNR), Naples, Italy
[2] GAIA iLAB, Portici, Italy
[3] Università degli Studi di Napoli Parthenope, Naples, Italy
[4] Istituto di Fisica Applicata "Nello Carrara" (IFAC), Consiglio Nazionale delle Ricerche (CNR), Florence, Italy
[5] Istituto di Radioastronomia (IRA), Istituto Nazionale di Astrofisica (INAF), Bologna, Italy

The last decades have been characterized by a growing worldwide interest in space exploration for extending the human presence in the Solar System. In particular, the human exploration of the Martian surface is becoming a priority. The pathway to Mars is rooted in the experience gained with the International Space Station and is continuing through the development of various space missions of increasing complexity, which will lead to a long-term and sustainable human presence on the Moon as a prelude to human missions to Mars and beyond. The Moon is in fact considered an intermediate and fundamental step for testing most of the new technologies required for sustainable human exploration of deep space. Among these technologies, geophysical methodologies are becoming increasingly important as they allow us to investigate a whole range of elements that are fundamental to human space exploration, including the presence of water and resources (rare earth elements, metals, etc.), and places of protection such as lava tubes.

We here present an overview of two Italian National projects dedicated to the development of geophysical technologies for planetary exploration, including the "PROgramma di RIcerca Spaziale di base (PRORIS)" project, funded by the Italian Ministry of University and Research (MUR) and whose management has been assigned to the National Research Council of Italy (CNR) and the National Institute for Astrophysics (INAF), and the "Martian Analysis of Resources and Structures: Lava tubes, neAr-surface ice and aquifers Visibility and Assessment (MARS-LAVA)" project, led by CNR and INAF.

The PRORIS project is mainly related to the Moon exploration with the proposal of different activities for the development of methodologies and research prototypes for in situ characterization of the surface and subsurface and the validation of the developed technologies in terrestrial analog environments. The MARS-LAVA project instead aims at developing, optimizing and testing a suite of geophysical sensors with high potential for Mars exploration, and to develop analysis techniques based on data fusion/integration and modeling, by designing an optimized payload for the characterization of the site of a landed mission using a mobile platform. Both the projects involve the use of magnetometric and electromagnetic geophysical methods.

This contribution therefore aims to present the activities of these two projects in the context of current needs in planetary exploration. A particular focus is dedicated to the use of the magnetometric method to study lava tubes. More specifically, we present the preliminary results of two magnetometric surveys using Unmanned Aerial System (UAS) platform carried out at the test sites of the lava tubes of Vesuvius (Campania region, Italy) and Etna (Sicily region, Italy) volcanoes. The surveys have been conducted using the MagArrow magnetometer, equipped with Micro Fabricated Atomic Magnetometer (MFAM) sensors, the MagNimbus magnetometer in vertical gradiometer configuration, equipped with two QuSpin-Gen2 sensors, and the DJI Matrice 300 RTK drones.

The presented results highlight the potential of the magnetometric method in mapping lava tubes and the challenges that need to be overcome for an increasingly reliable future planetary exploration.

Acknowledgments

Some surveys have been conducted using geophysical equipment acquired under the ITINERIS project "EU–Next Generation EU Mission 4, Component 2–CUP B53C22002150006–Project IR0000032 ITINERIS–Italian Integrated Environmental Research Infrastructures" with the support of the "Geo Agro Interdisciplinary Analysis interdepartmental LABoratory (GAIA iLAB)".

Corresponding author: barone.a@irea.cnr.it

Integrated Geophysical Study of the Vipava River near Miren (Slovenia): River–Aquifer Interactions in the Transboundary Soča/Isonzo Basin

Gaia Travan[1], Flavio Accaino[1], Alessandro Affatato[1], Oziel Souza de Araujo[1], Ilaria Dreossi[1], Michela Giustiniani[1], Veronika Ivan[1], Goran Vižintin[2], Luigi Sante Zampa[1]

[1] *Istituto Nazionale di Oceanografia e di Geofisica Sperimentale –OGS, Trieste, Italy*
[2] *University of Ljubljana - Slovenia*

Understanding the connection between surface and groundwater systems is essential for the sustainable management of transboundary water resources. The Vipava River, a tributary of the Soča/Isonzo, flows from western Slovenia into northeastern Italy, crossing a transition zone between karst and alluvial domains. In this complex geological setting, river–aquifer interactions remain poorly constrained, with implications for both water quality and cross-border resource management.

This study uses an integrated near-surface geophysical approach to characterize the subsurface architecture and assess the hydraulic connectivity between the Vipava River and adjacent aquifers near Miren (Slovenia), shortly before its confluence with the Soča/Isonzo River. Two field campaigns, conducted in February and August 2025, combined high-resolution P- and S-wave seismic reflection and tomography, Electrical Resistivity Tomography (ERT), Self-Potential (SP) measurements, and gravimetry, all integrated within a GIS framework. The geodatabase serves a threefold purpose: (1) it consolidates the available geological, hydrogeological, hydrological, and environmental information for the area, enabling their integrated analysis; (2) it supports the identification of key areas where the geophysical investigations are required; and (3) it facilitates the interpretation of new results in the context of existing data.

Seismic profiles, tomographic velocity models, and gravimetric contrasts reveal a gently northward-dipping carbonate bedrock, probably overlain by stratified alluvial sediments.

ERT sections, together with time-lapse resistivity maps and electric field vectors, delineate bodies with contrasting permeability and degrees of saturation, allowing the identification of preferential flow pathways and zones of local hydraulic disturbance.

These findings refine previous hydrogeological models of the Soča/Isonzo basin and demonstrate the effectiveness of combining multiple geophysical methods to delineate hydrogeological boundaries and evaluate surface–groundwater interactions in complex transboundary environments.

Acknowledgments

This research was supported by the WABIN project (Transboundary river basin water balance with integrated methodologies and adaptation to climate change), co-financed by the European Union under the Interreg VI-A Italy-Slovenia Programme 2021–2027.

Corresponding author: gtravan@ogs.it

Full-3D Electrical Resistivity Tomography (ERT) for sinkhole assessment and gypsum mining planning

A. Vergnano[1], C. Caselle[1], C. Comina[1], D. Franco[2], S. Bonetto[1]

[1] *Università degli studi di Torino, Dipartimento di Scienza della Terra, Torino, Italy*
[2] *Politecnico di Torino, Dipartimento di Ingegneria per l'Ambiente, il Territorio e le Infrastrutture, Torino, Italy.*

Introduction

The prevention of risks related to surface subsidence and sinkholes during underground mining requires extensive assessments before and during the excavations, specifically dedicated to the investigation of the physico-mechanical features of the underground rock mass and of the groundwater circulation. Among other potentially applicable geophysical methods, past research with Electrical Resistivity Tomography (ERT) surveys reported a clear identification of sinkhole-affected volumes (Giampaolo et al., 2016; Khalil et al., 2022; Bonetto et al., 2023). Focusing on gypsum, ERT demonstrated also its effectiveness in the quantification of the exploitable resource both in terms of volumes and of quality of the material (e.g. Martínez-Moreno et al., 2015; Caselle et al., 2019 and 2024).

The top of gypsum geological units often has complex geometries due to several causes (e.g., relict karst morphologies, erosional surfaces, irregular surfaces due to the internal chaotic organization). Similarly, sinkholes have strongly three-dimensional geometries. All these elements are better investigated with full-3D ERT surveys than with conventional 2D surveys. Past 3D ERT surveys often employed the quasi-3D approach, consisting in acquiring many parallel ERT lines and inverting them in 3D. The full-3D approach has the advantage of minimizing the directional bias of the quasi-3D approach, which is useful in complex 3D geometries (Chambers et al., 2007).

We aim to investigate an underground gypsum quarry sited in Piedmont (NW Italy), in which an 80-m-diameter sinkhole has formed in April 2025, and past sinkhole events (2019) already affected the area (Bonetto et al., 2023). The quarry consists of 6 underground levels and is exploited following a room-and-pillars configuration. The exploited gypsum orebody lays in the Monferrato domain of the Tertiary Piedmont Basin, being part of the Valle Versa Chaotic Complex. From a geomechanical point of view, the orebody can be classified as a bimunit (i.e., unit with block-in-matrix fabric), with the additional possibility of labelling the matrix-supported and clast-supported portions, in accordance with the classification by Napoli et al., 2022, as "softBIMrocks I5H" and "broken formation", respectively having worse and better mechanical properties.

Methods

We designed a full-3D ERT survey to achieve a good compromise between data coverage, accessibility obstacles, and time constraints. We surveyed the entire quarry area prioritizing the sinkhole area. We employed a 3D ERT setup involving 8 lines each made by 48 electrodes spaced 10 m. We acquired 2D ERT data for each of the lines, and 3D data with cross-cable measurements between lines 1-2-3, 3.4.5 and 6-7-8. We employed a 72-channel Syscal Pro georesistimeter, manufactured by IRIS Instruments, connected to two "switches" to increase the total number of channels to 144. This instrument can acquire up to 10 potential difference measurements at the same time, provided that the electrode numbering is correctly concatenated in the sequence file.

The quadrupole sequence was created in a custom way, to include both same-cable and cross-cable measurement, and to be optimized to use all the available 10 simultaneous measurements allowed by the instrument. Since the distances involved are great, the logic to generate the sequence had to avoid generating quadrupoles with a too high geometric factor (k), while ensuring good penetration depth at the same time. In total, with 8 same-cable and 3 cross-cable sequences, we acquired about 60000 data points over the entire investigated volume. The whole survey lasted 2 days with a survey crew composed of 6 operators.

Results

We performed the 3D inversion with Resipy (Blanchy et al., 2020). Horizontal slices were cut from the 3D resistivity volume, to visualize the subsurface electrical resistivity at several depths. Figure 1 shows depth slices (from 220 m to 154 m a.s.l.), at the same altitudes as the quarry floor levels.

The electrical resistivity was quite variable across the investigated domain. In general, lower resistivity values are depicted in the upper layers (down to less than 10 Ωm) related to the presence of the cover materials. The resistivity is higher at greater depths (up to values higher than 100 Ωm), due to the presence of the gypsum formation. At depth (Figure 1 c to f) the higher resistivity values well correspond to the location of the excavation voids, which are mainly developed in the “broken formation” gypsum sub-facies. With this respect, it must be underlined that the imaged resistivity values could be partially influenced towards higher values by the presence of the highly resistive voids. Conversely at shallower depths, even in correspondence of excavation voids (Figure 1 a and b in the north part) resistivity values remain lower, probably due to the presence of the “softBIMrocks I5H” formation or higher water content areas.

Discussion

For gypsum rock masses organized as bimunits and with a sufficient resistivity contrast between rock blocks and matrix, the bulk electrical resistivity can be used to estimate the block-to-matrix ratio (Caselle et al., 2024). The block-to-matrix ratio of the two main sub-facies in the investigated gypsum rock mass were quantified of respectively around 55-60% (softBIMrocks I5H) and higher than 75% (broken formation subfacies). Hence, using the calibration curve proposed by Caselle et al., 2024, two resistivity thresholds as representative of the limits between the gypsum rock mass and the soil cover were assumed.

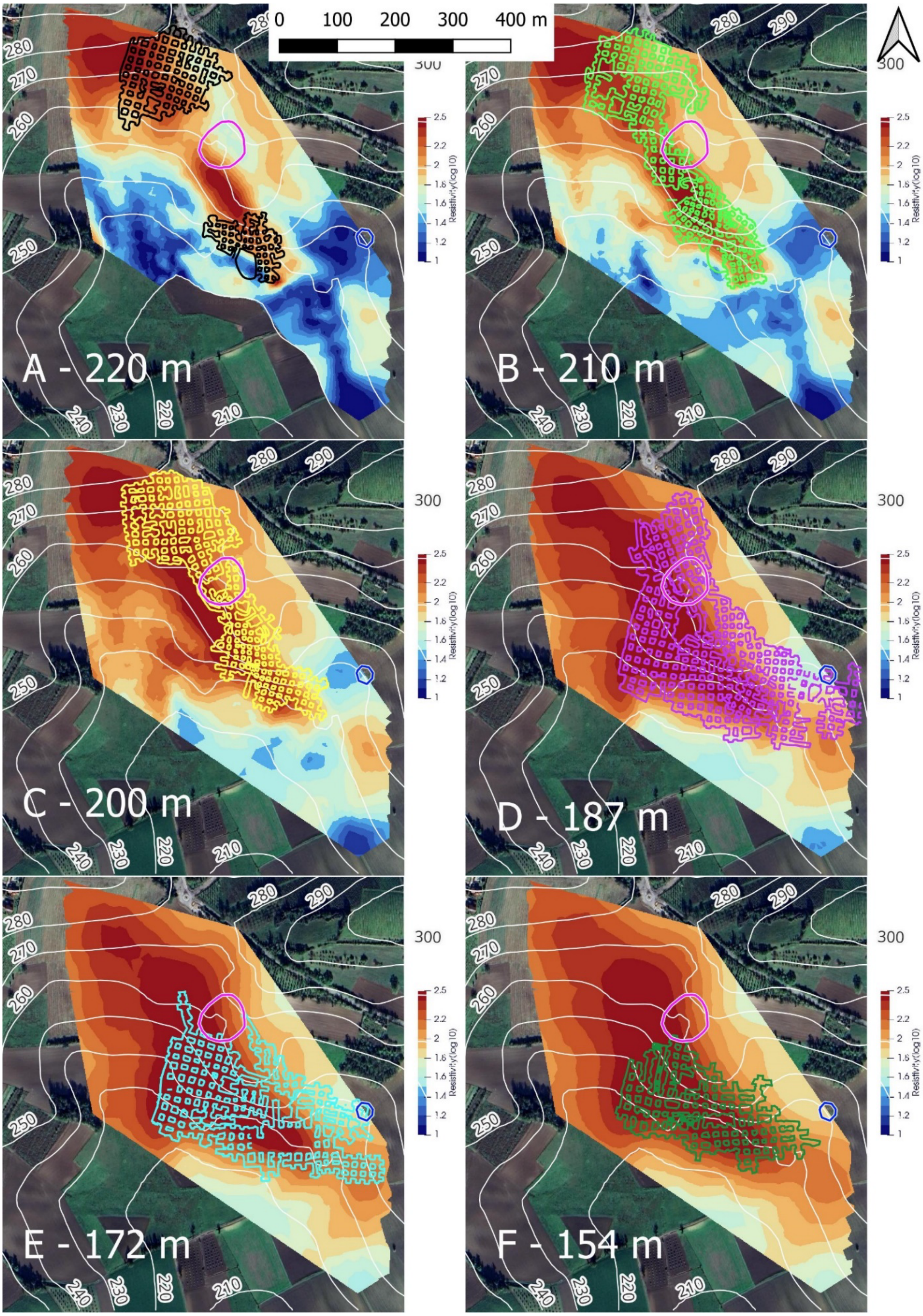

Fig. 1 – Electrical resistivity maps at the quarry floor levels (A – F). The 2025 sinkhole is pictured in purple, the 2019 sinkhole in blue.

Based on these thresholds (logarithm of the resistivity = 1.8, approximatively corresponding to 55% of blocks and logarithm of the resistivity = 2.5, approximatively corresponding to 73% of blocks), the color scale used for data visualization correspond to:

- Colors from blue to pale green/yellow correspond to the soil cover, with the possibility to distinguish between areas with higher (dark blue) and lower (light blue to pale green/yellow) water content;
- Orange-like colors correspond to the matrix-supported sub-facies of the gypsum orebody ("softBIMrocks I5H");
- Red color corresponds to the "broken formation" sub-facies.

As shown in Figure 2, the reliability of this interpretation founds a confirmation in the comparison between ERT output and the geological map of level A of the quarry. "Red" resistivities correspond to areas mapped as "broken formation", while "orange-like" resistivities correspond to areas mapped as "softBIMrock I5H".

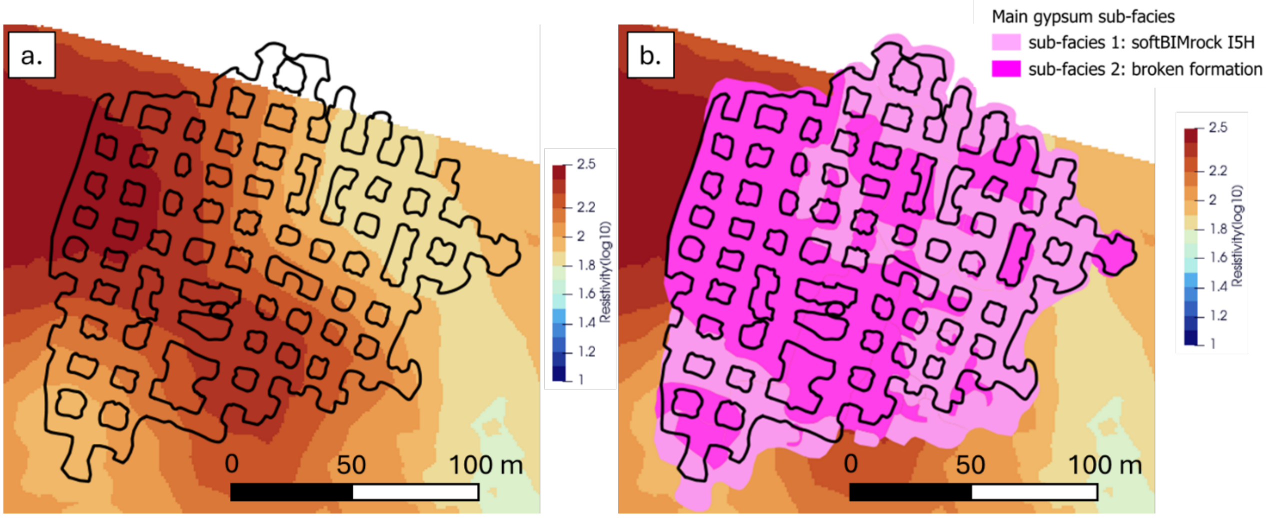

Fig. 2 – a. Electrical resistivity map (Ωm, in logarithmic scale) at z = 220 m a.s.l.. The black drawing depicts quarry level A; b. Comparison of resistivity map in panel a with geological map.

Figure 3 reports a vertical slice extracted from the 3D ERT volume. Based on the previous considerations, we drew the limit between gypsum body and soil covers (black continuous line). As can be seen, the data suggests that this surface is irregular, with local depressions. In particular, A-A slice highlights the presence of a main depression in correspondence of the sinkhole.

The portions classified as "broken-formation" (i.e., portions with better mechanical features) usually correspond to morphological "highs" in the interface between gypsum and soil covers. In addition, the position of the sinkhole corresponds with portions of the rock mass with worse mechanical properties (softBIMrock I5H sub-facies). In the soil covers, we further set a limit between portions with higher and lower resistivity (red dashed line). Portions with lower resistivity may be considered as saturated in water. They can be part of the sinkhole deposits, or they can signal potentially future locations of new sinkholes.

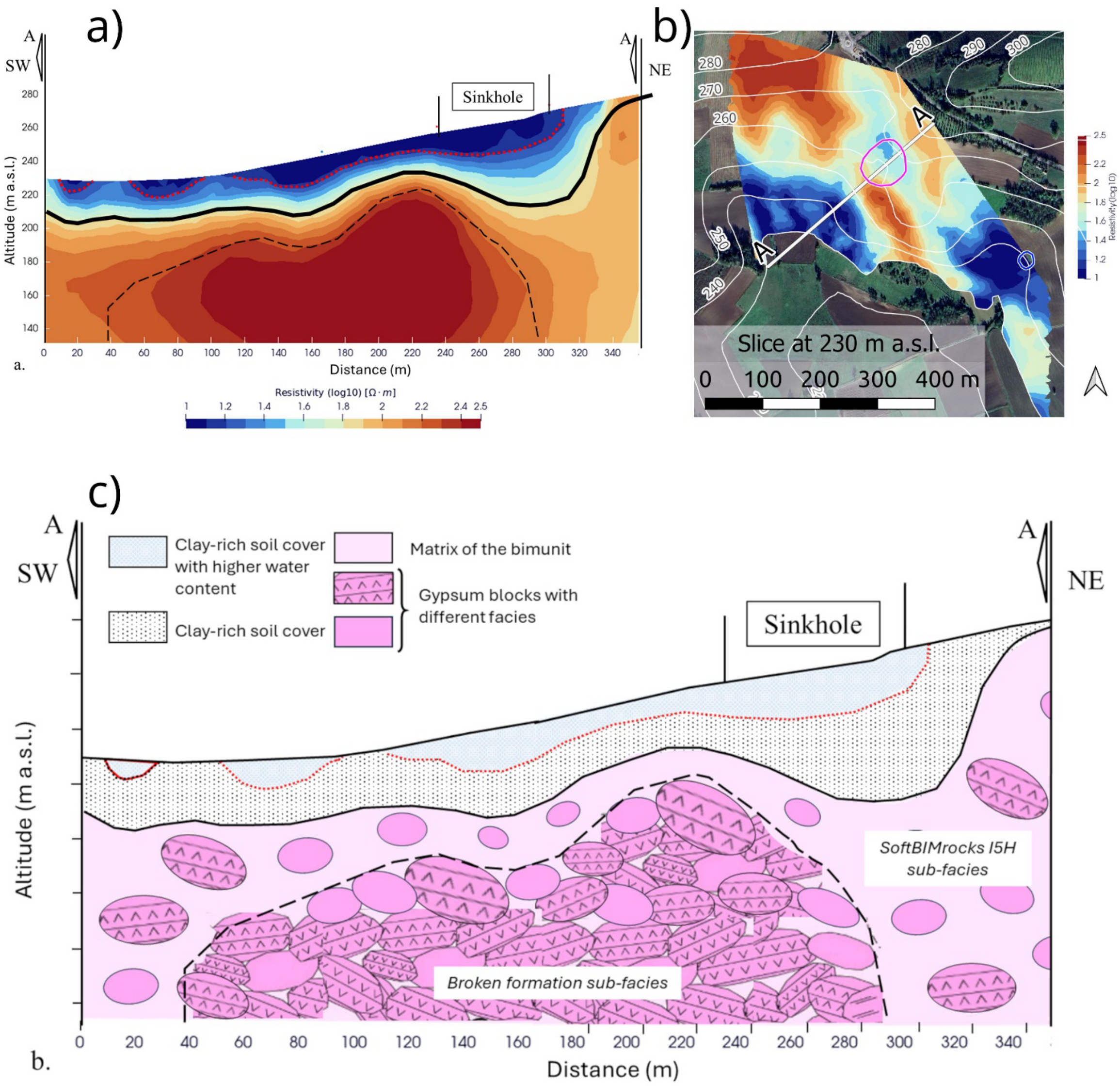

Fig. 3 – Resistivity profile A-A (a), its location on the map (b), and its geological interpretation (c)

Conclusions

We presented a fast, full-3D ERT survey setup for investigating a 20-hectares area containing an 80-m-diameter sinkhole. This approach obtained a coarse, but reliable resistivity model of the gypsum orebody in the quarry area. The model defined the complex geometry of the top surface of the orebody and classified the portions of the orebody with different compositional (and, in turn, mechanical) properties. The survey highlighted conductive areas at the surface as potential regions of water accumulation and infiltration.

The proposed approach can be employed as a preliminary investigation tool for mining purposes. Being able to distinguish the different sub-facies of gypsum rock, the method allows detecting favorable directions of quarry development, in order to find compact, higher quality rock and reduce collapse risks.

A limitation of the performed inversion process is that we did not consider the quarry voids in the inversion mesh, possibly causing an overestimation of the rock resistivity at depth. However, the resistivity distribution seems quite independent on the quarry voids. In fact, low-resistivity areas are clearly detected even in correspondence with quarry voids and seems directly related to geological properties (e.g., properties of the gypsum rock mass or water infiltration).

Future research could focus on comparing this approach to another approach often used for deep basin-scale investigations (the "FullWaver" approach, as in Sapia et al., 2021), which consists in sparse dipole arrangements with very large distances between electrodes. Moreover, other geophysical techniques, such as refraction seismic and surface wave analysis, could be integrated to add information more closely related to rock mechanical strength.

Acknowledgments

We are indebted with Arianna Paschetto, Antonio Merico, Yan Han for their generous help during fieldwork. We thank Francesco Tozzato for his help with the quadrupole sequences. We thank Estrazione Gesso s.r.l. (gypsum mining company) for their permission to publish this work conducted in their property, and Sergio for his help during fieldwork.

References

Bonetto, S., Caselle, C., Comina, C., Vagnon, F., 2023. Geophysical surveys for noninvasive characterization of sinkhole phenomena: a case study of Murisengo. Earth Surf. Process. Landf. 48 (9), 1895–1905. https://doi.org/10.1002/esp.5584.

Blanchy, G., Saneiyan, S., Boyd, J., McLachlan, P., Binley, A., 2020. ResIPy, an intuitive open source software for complex geoelectrical inversion/modeling. Computers & Geosciences 137, 104423. https://doi.org/10.1016/j.cageo.2020.104423

Caselle, C., Bonetto, S., Comina, C., 2019. Comparison of laboratory and field electrical resistivity measurements of a gypsum rock for mining prospection applications. Int. J. Min. Sci. Technol. 29 (6), 841–849. https://doi.org/10.1016/j.ijmst.2019.09.002.

Caselle, C., Comina, C., Festa, A., Bonetto, S., 2024. Electrical resistivity tomography for the evaluation of Areal Block Proportion (ABP) in bimunits: Modelling and preliminary field validation. Engineering Geology 333, 107488. https://doi.org/10.1016/j.enggeo.2024.107488

Chambers, J.E., Wilkinson, P.B., Weller, A.L., Meldrum, P.I., Ogilvy, R.D., Caunt, S., 2007. Mineshaft imaging using surface and crosshole 3D electrical resistivity tomography: A case history from the East Pennine Coalfield, UK. Journal of Applied Geophysics 62, 324–337. https://doi.org/10.1016/j.jappgeo.2007.03.004

Giampaolo, V., Capozzoli, L., Grimaldi, S., Rizzo, E., 2016. Sinkhole risk assessment by ERT: The case study of Sirino Lake (Basilicata, Italy). Geomorphology 253, 1–9. https://doi.org/10.1016/j.geomorph.2015.09.028

Gómez-Ortiz, D., Martín-Crespo, T., 2012. Assessing the risk of subsidence of a sinkhole collapse using ground penetrating radar and electrical resistivity tomography. Engineering Geology 149–150, 1–12. https://doi.org/10.1016/j.enggeo.2012.07.022

Khalil, M.A., Sadeghiamirshahidi, M., Joeckel, R.M., Santos, F.M., Riahi, A., 2022. Mapping a hazardous abandoned gypsum mine using self-potential, electrical resistivity tomography, and Frequency Domain Electromagnetic methods. Journal of Applied Geophysics 205, 104771. https://doi.org/10.1016/j.jappgeo.2022.104771

Martínez-Moreno, F.J., Galindo-Zaldívar, J., Pedrera, A., González-Castillo, L., Ruano, P., Calaforra, J.M., Guirado, E., 2015. Detecting gypsum caves with microgravity and ERT under soil water content variations (Sorbas, SE Spain). Engineering Geology 193, 38–48. https://doi.org/10.1016/j.enggeo.2015.04.011

Napoli, M.L., Festa, A., Barbero, M., 2022. Practical classification of geotechnically complex formations with block-in-matrix fabrics. Engineering Geology 301, 106595. https://doi.org/10.1016/j.enggeo.2022.106595

Corresponding author: andrea.vergnano@unito.it